The STAR Beam Use Request for Run-20 and Run-21

The STAR Collaboration

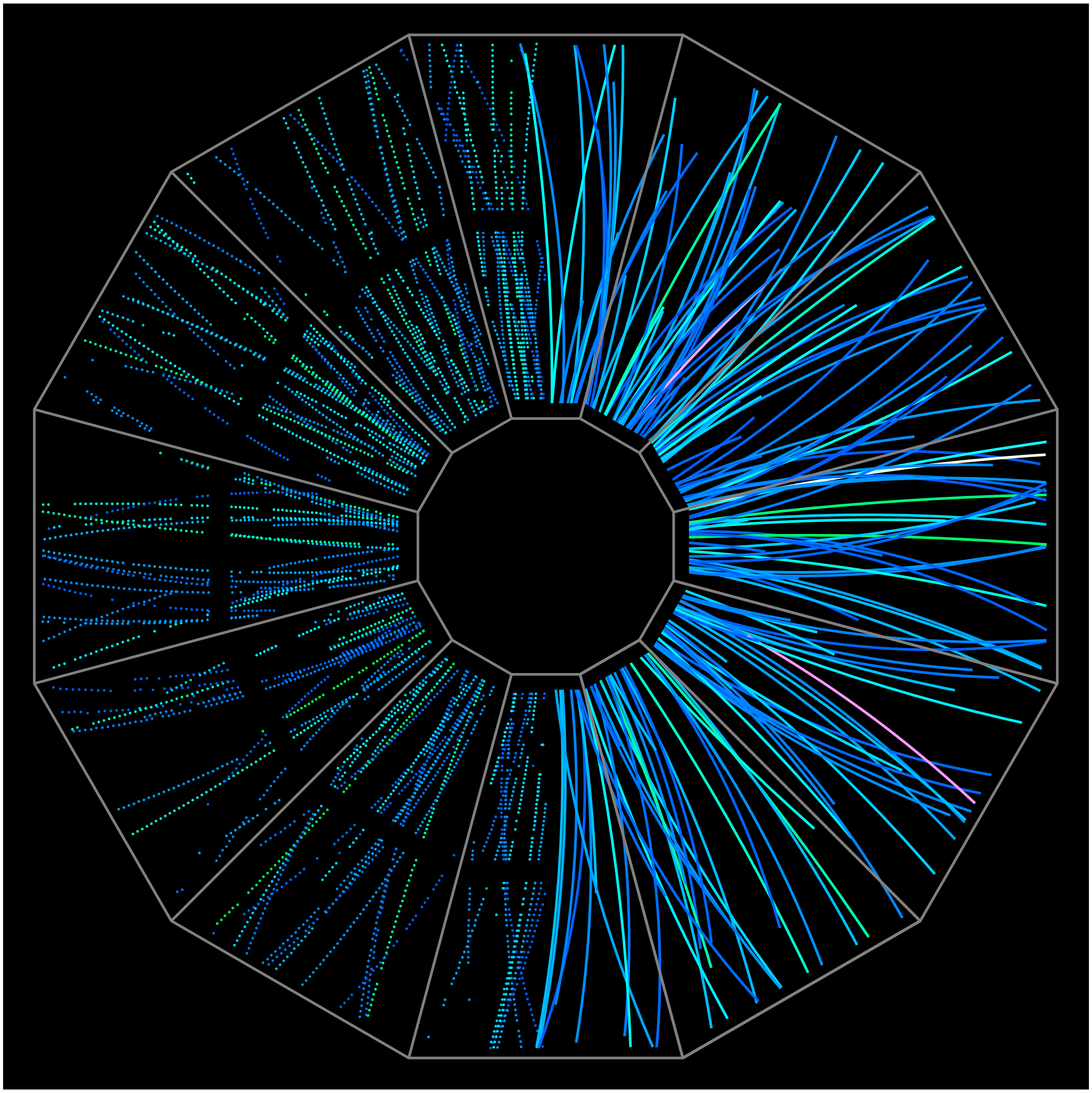

May 15, 2019

Executive Summary

This Beam Use Request from the STAR collaboration for RHIC Run-20 and Run-21 is focused on the completion of the NSAC-endorsed second phase of the Beam Energy Scan (BES-II) program. This program started with Run-19 in which the collaboration aims to collect data from the two top collider energies of $\sqrt{s_{\rm NN}}$=19.6 and 14.6 GeV as well as data from a subset of the fixed target (FXT) program. Collection of all the data outlined in Table 1 is STAR's **highest scientific priority**. Additionally, the STAR collaboration proposes a small system run to study the emergence of collectivity and the mechanism for early-time *hydrodynamization* in large collisions systems.

BES-II will dramatically enhance our understanding of the QCD phase diagram. The proposed program involves dedicated low beam energy running and high precision measurements of the observables which have been proposed as sensitive to the phase structure of QCD matter. In addition to the five lower collider energies that have been put forward in past BURs, STAR proposes a sixth collider beam energy at $\sqrt{s_{\rm NN}}$ = 16.7 GeV. These data will provide for a finer scan in a range where the energy dependence of the net-proton kurtosis and neutron density fluctuations appears to undergo a sudden change.

Table 1: Summary of all BES-II and FXT Au+Au beam energies, equivalent chemical potential, requested event statistics, and run times.

Beam Energy (GeV/nucleon)	$\sqrt{s_{NN}}$ (GeV)	$\mu_{\rm B}$ (MeV)	Run Time	Number Events	Status
9.8	19.6	205	4.5 weeks	400M	Run-19 (finished)
7.3	14.6	260	5.5 weeks	300M	Run-19 (in progress)
8.35	16.7	235	5 weeks	250M	
5.75	11.5	315	9.5 weeks	230M	LEReC availability?[1]
4.55	9.1	370	9.5 weeks	160M	
3.85	7.7	420	12 weeks	100M	
31.2	7.7 (FXT)	420	2 days	100M	Run-19 (scheduled)
9.8	4.5 (FXT)	589	2 days	100M	Run-19 (scheduled)
7.3	3.9 (FXT)	633	2 days	100M	Run-19 (scheduled)
19.5	6.2 (FXT)	487	2 days	100M	
13.5	5.2 (FXT)	541	2 days	100M	
5.75	3.5 (FXT)	666	2 days	100M	
4.55	3.2 (FXT)	699	2 days	100M	
3.85	3.0 (FXT)	721	2 days	100M	

[1] At the time of this writing, the availability of LEReC for the 11.5 GeV energy is not clear. Consequently, the run time for this energy is changed from last year's BUR. The new estimate is based on the 14.6 GeV performance in Run-19. A more optimistic estimate, based on the 19.6 GeV performance, would be 7.5 weeks.

With Run-19, the collaboration will start its fixed-target (FXT) program which extends the reach of its BES-II program energy range down to lower center-of-mass energies. The proposed energies for both collider and fixed-target mode are summarized in Table 1.

Three detector upgrades have been proposed for BES-II and have been successfully installed for Run-19. The upgrades increase STAR's acceptance both in rapidity and low transverse momentum, and extend its particle identification capabilities. The Event Plane Detector (EPD) was installed prior to Run-18. The inner Time Projection Chamber (iTPC) and the end-cap Time-of Flight (eTOF) commissioning have benefited from an extensive cosmic ray data taking campaign prior to Run-19. Following recommendations from the 2018 PAC and a very positive report from a BNL-convened *cost and schedule* review, the STAR collaboration has commenced preparations to significantly improve its forward detection capabilities. A Forward Calorimeter System (FCS) and Forward Tracking System (FTS) will provide superior detection capabilities in the forward region between $2.5 < \eta < 4$.

Table 2: Proposed Run-20 assuming 28 cryo-weeks, including five weeks of LEReC commissioning, an initial one week of cool-down and a one week set-up time for each collider energy.

Single-Beam Energy (GeV/n)	$\sqrt{s_{NN}}$ (GeV)	Run Time	Species	Events (MinBias)	Priority	Sequence
5.75	11.5	9.5 weeks	Au+Au	230M	1	1
4.55	9.1	9.5 weeks	Au+Au	160M	1	3
19.5	6.2 (FXT)	2 days	Au+Au	100M	2	5
13.5	5.2 (FXT)	2 days	Au+Au	100M	2	6
5.75	3.5 (FXT)	2 days	Au+Au	100M	2	2
4.55	3.2 (FXT)	2 days	Au+Au	100M	2	4
3.85	3.0 (FXT)	2 days	Au+Au	100M	2	7
100	200	1 week[2]	O+O	400M 200M (central)	3	8

[2] Available run time for the proposed small system run using O+O will directly depend on the the run time for the 11.5 GeV system. In the case the combined performance of C-AD and STAR resembles that of last year's 19.6 GeV data set, then approximately 2 cryo-weeks would be available to complete the small system program.

STAR's **highest scientific priority for Run-20** is the continuation of the RHIC Beam Energy Scan II. The collaboration proposes to continue with the next two highest beam energies in collider mode (11.5 and 9.1 GeV), as well as the associated FXT energies (4.55 and 5.75 GeV) followed by the remaining FXT single-beam energies of 19.5, 13.5, and 3.85 GeV. We list the Run-20 priorities and proposed sequence in Table 2. Based on guidance from the Collider-Accelerator Department (C-AD), we allocate five cryo-weeks in Run-20 to the commissioning of Low-Energy RHIC electron Cooling (LEReC). As the commissioning efforts are still ongoing, the status of LEReC for the Run-20 11.5 GeV is not yet clear. Consequently, the proposed schedule will be somewhat fluid within the total budget of 28 cryo-weeks.

Table 3: Proposed Run-20 assuming 24 cryo-weeks, including three to four weeks of LEReC commissioning, an initial one week of cool-down and less than one week set-up time for each collider energy.

Single-Beam Energy (GeV/n)	$\sqrt{s_{NN}}$ (GeV)	Run Time	Species	Events (MinBias)	Priority	Sequence
5.75	11.5	7.5 weeks[3]	Au+Au	230M	1	1
4.55	9.1	9.5 weeks	Au+Au	160M	1	3
19.5	6.2 (FXT)	2 days	Au+Au	100M	3	5
13.5	5.2 (FXT)	2 days	Au+Au	100M	3	6
5.75	3.5 (FXT)	2 days	Au+Au	100M	2	2
4.55	3.2 (FXT)	2 days	Au+Au	100M	2	4
3.85	3.0 (FXT)	2 days	Au+Au	100M	3	7

[3] In this 24 cryo-week scenario an optimistic view on the performance of the 11.5 GeV run is presumed, based on combined performance of C-AD and STAR resembling that of last year's 19.6 GeV run.

In Table 3, we list our priorities and proposed sequence in the case the total budget for Run-20 is limited to 24 cryo-weeks. Top priority remains with the collider program of the Beam Energy Scan and the commissioning efforts of LEReC, bearing in mind its impact on the long 7.7 GeV run in the following year. With a combined cool-down and total set-up time for the various energies between two and three weeks, an optimistic projection for the non-cooled 11.5 GeV run, and an e-cooled 9.1 GeV run, we estimate that between three and four weeks of dedicated LEReC commissioning time can be set aside and at least 60% of the originally scheduled FXT program completed. The remaining two FXT runs could move to Run-21, as will the small system run.

STAR's **highest scientific priority for Run-21** is the completion of the RHIC Beam Energy Scan II. The bulk of the 20-cryoweeks budget will be devoted to Au+Au collisions at the lowest collider energy of the program, at $\sqrt{s_{NN}}$ =7.7 GeV. We expect to refine our estimates of the projected run time for 7.7 GeV, currently 12 weeks, following some tests with C-AD towards the end of Run-19. The collaboration proposes to run the collider at $\sqrt{s_{\rm NN}} = 16.7$ GeV to allow collection of an important data point between 14.6 and 19.6 GeV as is pointed out earlier in this summary. We list the Run-21 proposed priorities and sequence in Table 4.

Depending on the availability of cryo-weeks in Run-20 and/or Run-21 the collaboration proposes to collect data set(s) in the context of a small system run using O+O collisions. These data would allow for a direct comparison with a similarly proposed higher-energy O+O run at the LHC around 2021-2022, and further motivate the case for a small system scan complementary to ongoing efforts by the NA61/SHINE collaboration at SPS energies, and other proposed light-ion species at the LHC.

For FY22, we include a request for a dedicated 16-week *pp* run at $\sqrt{s} = 500$ GeV. This run will take full advantage of STAR's new forward detection capabilities and further capitalize

Table 4: Proposed Run-21 assuming 20 cryo-weeks, including an initial one week of cool-down and a one week set-up time for each collider energy.

Single-Beam Energy (GeV/n)	$\sqrt{s_{NN}}$ (GeV)	Run Time	Species	Events (MinBias)	Priority	Sequence
3.85	7.7	12 weeks	Au+Au	100M	1	1
8.35	16.7	5 weeks	Au+Au	250M	2	2
100	200	1 week[4]	O+O	400M 200M (central)	2	3

[4] In the case the proposed small system run can not take place in Run-20, the cryo-week budget for Run-21 could potentially permit this run to take place depending on the Run-20 LEReC performance.

on the recent BES-II detector upgrades. We motivate a program that will use RHIC's unique ability to provide transverse and longitudinally polarized proton beams to exploit both an increased statistical power and kinematic reach from recent and planned detector upgrades as proposed in [1, 2].

Contents

1 Highlights from the STAR Program

1.1 Heavy Ion Highlights

Heavy Flavor Physics

Quarkonium Suppression in Au+Au Collisions
With high statistics pp and A+A datasets collected in recent years by both the Muon Telescope Detector (MTD) and the Barrel EMC (BEMC) detectors, STAR has conducted extensive measurements of quarkonium production to study both cold and hot QCD dynamics. STAR recently submitted two quarkonium measurement papers utilizing the data collected by the MTD in Au+Au and pp collisions, respectively. The MTD is designed to measure J/ψ and the 1S and (2S+3S) Υ states to investigate the proposed sequential melting picture due to color screening in the QGP medium. Figure 1 shows the MTD's comprehensive measurement of J/ψ R_{AA} as a function of p_{T} from $\sim$0 up to $\sim$12 GeV/c in various centrality bins at $\sqrt{s_{\mathrm{NN}}} = 200$ GeV, little dependence on p_{T} is observed for all centrality bins. In the 0-10% most central collisions, the J/ψ yield is suppressed by a factor of approximately 3 for $p_{\mathrm{T}} > 5$ GeV/c relative to that in binary collision scaled pp collisions. Model calculations can qualitatively describe the data, providing further evidence for the color-screening effect experienced by J/ψ mesons in the QGP.

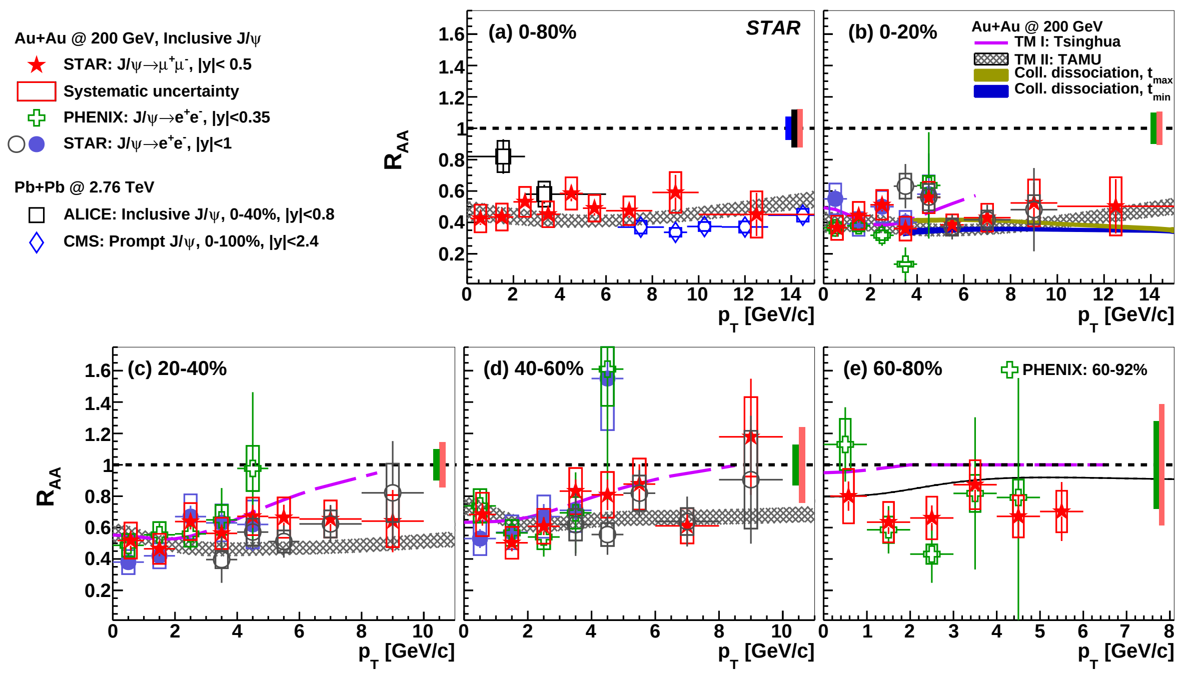

Figure 1: R_{AA} of J/ψ as a function of p_{T} in different centrality intervals of 200 GeV Au+Au collisions compared to other measurements and model calculations.

With the 2014+2016 combined data sets from the MTD, STAR was able to identify the different Υ states [3], shown in Fig. 2 left panel. Combined with the measurement of

e^+e^- channel, $\Upsilon(1S)$ and $\Upsilon(2S+3S)$ $R_{\rm AA}$ were calculated respectively and their centrality dependence is shown in the right panel of Fig. 2. The $R_{\rm AA}$ of $\Upsilon(2S+3S)$ is smaller than that of $\Upsilon(1S)$ in central Au+Au collisions, consistent with the sequential melting picture as calculated in a transport model indicated by the blue bands in the figure.

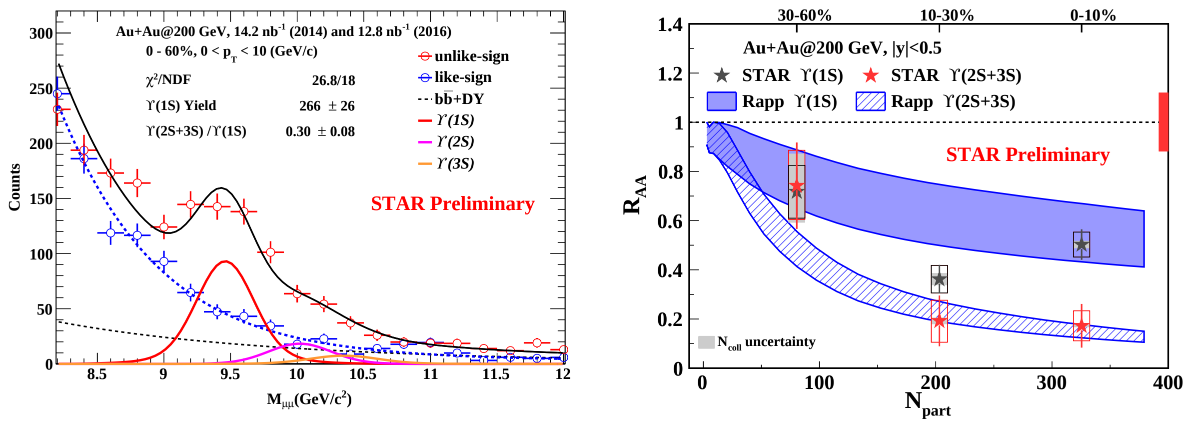

Figure 2: (Left) $\mu^+\mu^-$ invariant mass spectra measured by MTD combining 2014+2016 data sets in Au+Au collisions at 200 GeV. (Right) $R_{\rm AA}$ of $\Upsilon(1S)$ and $\Upsilon(2S+3S)$ from combined measurements of $\mu^+\mu^-$ and e^+e^- channels in Au+Au collisions as a function of centrality.

J/ψ Production in pp Collisions

STAR recently submitted a paper on the J/ψ production cross section measurement over a broad $p_{\rm T}$ coverage in *pp* collisions at top RHIC energy. Figure 3 (a) shows the J/ψ production cross section measured at mid-rapidity in *pp* collisions via $\mu^+\mu^-$ and e^+e^- channels at 510 and 500 GeV, respectively. The combined measurements cover a $p_{\rm T}$ region of 0–20 GeV/c. Panel (b) shows the ratio of the measured data to a Levy function fit. Panel (c) and (d) show comparisons to several model calculations. Those from CGC+NRQCD [4], NLO NRQCD [5] and ICEM [6], which cover low, high and both $p_{\rm T}$ regions respectively, give a reasonable description for the data within the polarization envelope.

D^0 Meson Directed Flow

STAR recently submitted a paper reporting the first measurement of rapidity-odd directed flow, v_1, of D^0 mesons [7]. The heavy flavor v_1 is predicted to be sensitive to the initial geometric tilt angle of the QGP source and the charm-medium interaction strength [8]. The difference between charm and anti-charm quark v_1 is proposed to have a unique sensitivity to the initial strong magnetic field created in heavy-ion collisions [9]. Figure 4 top panel shows the averaged D^0 and $\overline{D}^0$ meson v_1 as a function of rapidity compared to charged kaons and theory model calculations. The measured v_1 of D^0 mesons shows a significant negative slope around $y = 0$ and the absolute value of the slope parameter is nearly a factor of 25 times than that of charged kaons. The hydrodynamic model with an initially tilted QGP source can qualitatively describe the large negative v_1 slope. These data are expected to offer

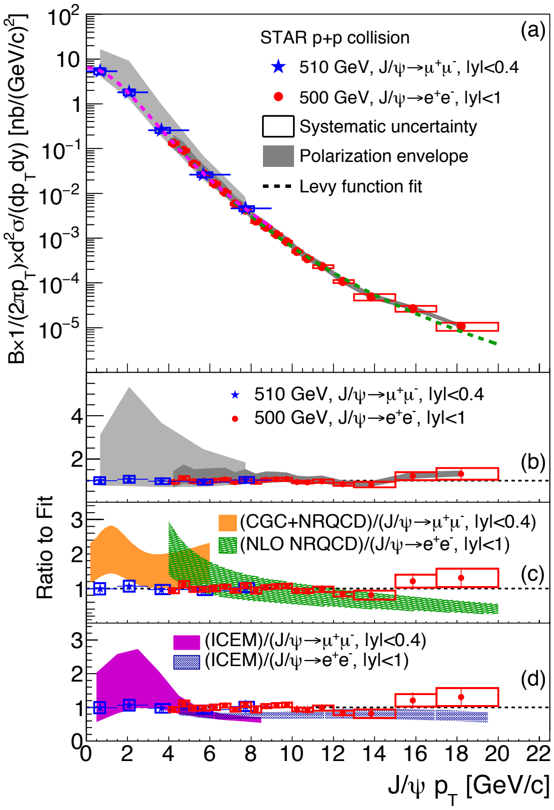

Figure 3: (a) Inclusive J/ψ production cross section as a function of p_{T} in pp collisions $\sqrt{s_{\mathrm{NN}}}$ = 510 and 500 GeV measured through $\mu^+\mu^-$ (blue stars) and e^+e^- decay channels (red circles). (b, c, d) Ratios of data and different model calculations to the Levy function fit to the measured data.

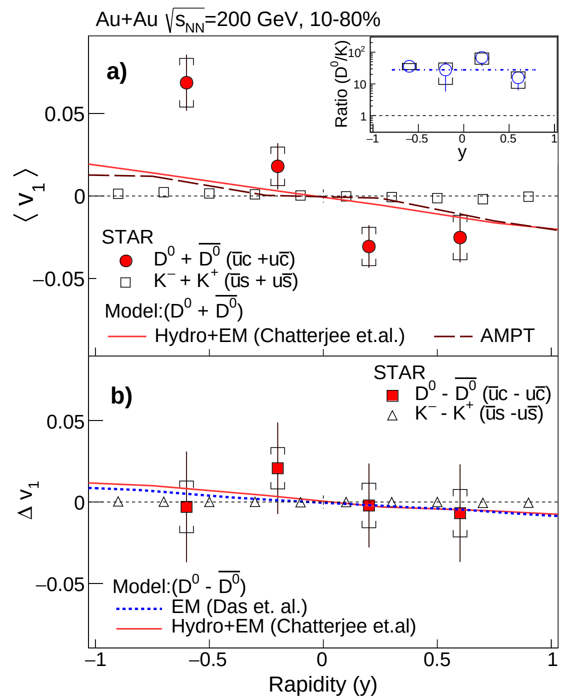

Figure 4: The average v_1 of D^0 and $\overline{D}^0$ (top) and v_1 difference between D^0 and $\overline{D}^0$ (bottom) as a function of rapidity in Au+Au collisions at $\sqrt{s_{NN}} = 200\,\mathrm{GeV}$ compared to light hadron measurement as well as model predictions.

unique constraints for the geometric and transport parameters of the hot QGP medium. The bottom panel of Fig. 4 shows the difference in v_1 between D^0 and $\overline{D}^0$ mesons. Our experimental uncertainty is not sufficient enough to reveal the predicted signal induced by the initial magnetic field.

D^0 Meson Spectra and Radial Flow

STAR recently published the high precision measurement of D^0 meson spectra in various centrality bins in Au+Au collisions at $\sqrt{s_{\mathrm{NN}}} = 200\,\mathrm{GeV}$ with the HFT detector [10, 11]. The broad transverse momentum coverage (from zero to $\sim 8\,\mathrm{GeV}/c$) allows detail investigation of D^0 freeze-out properties and collectivity through the fireball evolution. The kinetic freeze-out temperature T_{kin} and average transverse velocity extracted from a Blast-Wave (BW) thermal model fit to the D^0 spectra are shown in the left panel of Fig. 5. The BW fit result suggests

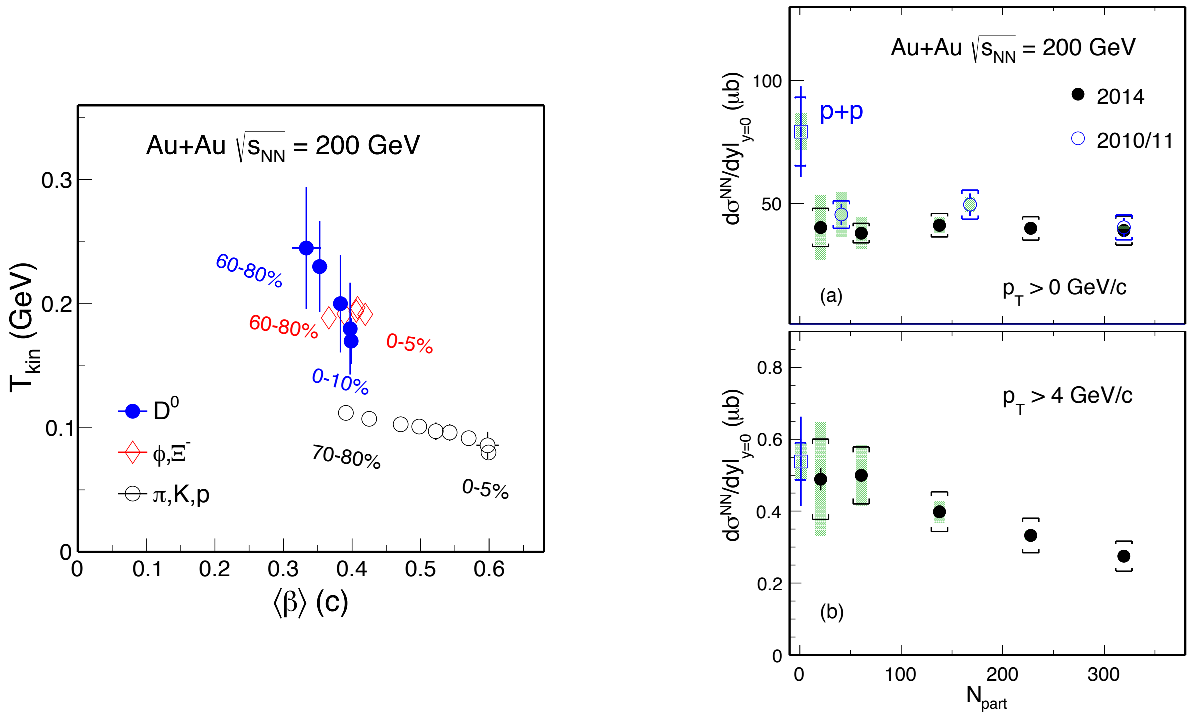

Figure 5: (Left) Kinetic freeze-out parameters obtained through Blast-Wave model fits to D^0 mesons compared to light and multi-strange hadrons in Au+Au collisions at $\sqrt{s_{\mathrm{NN}}} = 200\,\mathrm{GeV}$. (Right) p_{T}-integrated D^0 cross sections in pp and Au+Au collisions in different centrality bins for $p_{\mathrm{T}} > 0\,\mathrm{GeV}/c$ and $p_{\mathrm{T}} > 4\,\mathrm{GeV}/c$, respectively.

that D^0 mesons kinematically freeze out from the system at a higher temperature and with a smaller radial collectivity, that are comparable to those obtained from multi-strange hadrons, than those of the light flavor hadrons.

This broad momentum coverage also allows the extraction of the p_{T} integrated D^0 total cross section, shown in the upper right panel of Fig. 5. The results in Au+Au collisions from this measurement show no significant centrality dependence, and the total D^0 cross section in central Au+Au collisions is smaller than that obtained in pp collisions ($\sim 1.5\sigma$). The bottom right panel in Fig. 5 shows the integrated cross section at $p_{\mathrm{T}} > 4\,\mathrm{GeV}/c$ gradually decreases from pp to central Au+Au collisions, consistent with the expectation of the increased energy loss in the QGP medium in more central heavy-ion collisions.

Λ_c Baryon Production

The reduction in the total D^0 cross section in central Au+Au collisions indicates there are finite cold nuclear matter shadowing effects and/or a change in the abundances of the different charm hadrons in heavy-ion collisions. STAR has previously reported the observation of enhancements in the D_s^+/D^0 and Λ_c/D^0 ratios in Au+Au collisions compared to the fragmentation baseline constrained from other ee/ep collisions [12]. STAR has now extended the Λ_c baryon measurements by applying a supervised machine learning technique as well as including the new 2016 dataset [13]. This improved reconstruction allows us to study its

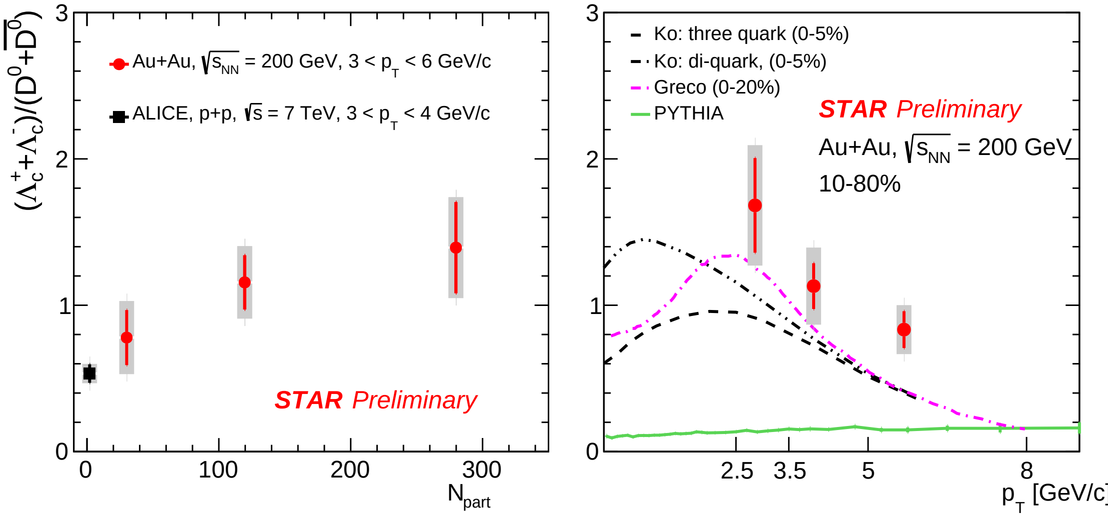

Figure 6: (Left)Λ_c/D^0 ratio in Au+Au collisions at $\sqrt{s_{\rm NN}} = 200\,$GeV as a function of $N_{\rm part}$ and (Right) $p_{\rm T}$.

centrality and $p_{\rm T}$ dependence, shown in Fig. 6 left and right panels, respectively. The Λ_c/D^0 ratio shows a large enhancement around $3\,$GeV$/c$ compared to PYTHIA calculations and gradually decreases with the increasing $p_{\rm T}$ from 2.5 to $8\,$GeV$/c$. The centrality dependence of this ratio shows a gradual increase from peripheral to central Au+Au collisions. These features are qualitatively consistent with several coalescence model calculations as shown; the difference between models is sizable depending on their choices of the coalescence parameters etc. The Λ_c/D^0 ratio in the measured $p_{\rm T}$ region is also larger than the expectation from statistical hadronization model.

The large Λ_c/D^0 ratio indicates that the Λ_c baryon makes a sizable contribution to the total charm cross section. STAR has the capability to measure all major ground state charm hadrons (D^0, D^+, D_s^+, and Λ_c). An analysis that combines their measured cross sections results in a $p_{\rm T}$ integrated $c\bar{c}$ total cross section per nucleon-nucleon collision at mid-rapidity $d\sigma^{c\bar{c}}_{\rm NN}$=152$\pm$13(stat.)$\pm$29(sys.)$\mu$b. The total cross section measured in Au+Au collisions is compatible with that extracted from pp within the experimental uncertainties. This indicates that although the produced charm quarks approximately follow the number-of-binary-collision scaling, the relative abundances between different charm hadrons change considerably from pp to central Au+Au collisions.

Light Flavor & Ultra-Peripheral Physics

HyperNuclei and Light Nuclei

We recently submitted for publication measurements of the Λ hyperon binding energy, B_Λ, for the hypertriton, which is the lightest hypernucleus yet discovered and consists of a proton, a neutron, and a Λ hyperon [14]. This new study places stringent constraints on the hyperon-

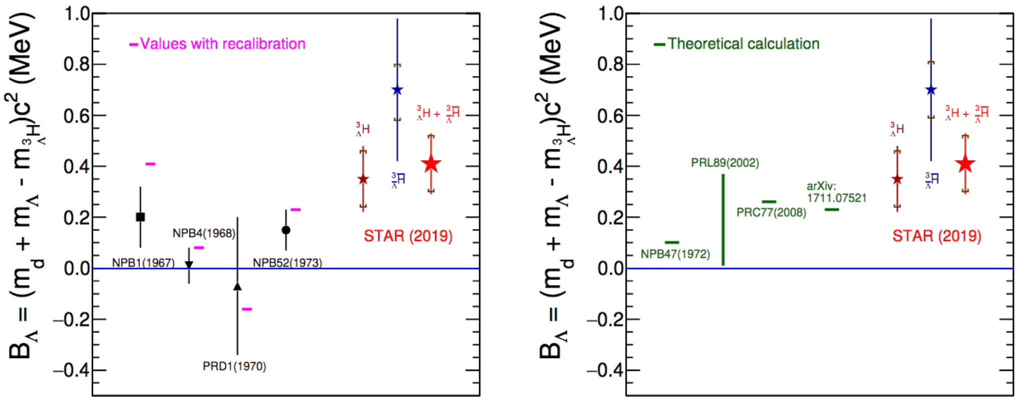

Figure 7: (Left) Comparison of the STAR results on Λ binding energy (B_Λ) for hypertriton and antihypertriton with earlier measurements and (Right) theoretical calculations [15, 16, 17]. The black points and the statistical uncertainties as shown as bars represent earlier results. The short horizontal magenta lines represent the best estimates of B_Λ based on the same early data but using modern hadron and nucleus masses.

nucleon interaction, and provides critical inputs for studying neutron star interiors, where strange matter may be present. It also provides a quantitative test for the first time of the matter-antimatter symmetry pertaining to the binding of strange and anti-strange quarks (s and $\bar{s}$) in a nucleus.

STAR's measurement of Λ binding energy for hypertriton and antihypertriton ($B_\Lambda \equiv m_d + m_\Lambda - m_{{}^3_\Lambda H}$ is presented in Fig. 7 (left panel) along with earlier measurements from nuclear emulsion and helium bubble chamber experiments [15, 16, 17]. The current STAR result differs from zero with a significance of 2.6σ. The daughter particle masses used in the early measurements of were different from contemporary standard CODATA and PDG values [18]. Thus the early B_Λ values have been recalculated using the most precise mass values known today, and the recalibrated results are shown by short horizontal magenta lines in Fig. 7. Our result is larger than the widely accepted prior measurement from 1973. In addition, theoretical calculations are also available as presented in right panel of Fig. 7.

Since the binding energies of (anti)deuterons is small ($\sim$2.2 MeV) they cannot survive when the temperature is much higher than the binding energy. Their production can therefore be used to extract important information on the distribution of nucleons at freeze-out. An article on the beam energy dependence of (anti-)deuteron production in Au+Au collisions has just been accepted for publication [19]. While the yields are shown to be well described by thermal model predictions, the extracted values of the coalescence parameter, B_2, for anti-deuterons are systematically lower than those for deuterons, indicating that the correlation volume of anti-baryons is larger than that of baryons for $\sqrt{s_{NN}}$ = 19.6 -39 GeV. In addition, as shown in Fig. 8, a broad minimum in B_2 is observed around $\sqrt{s_{NN}}$ = 20-40

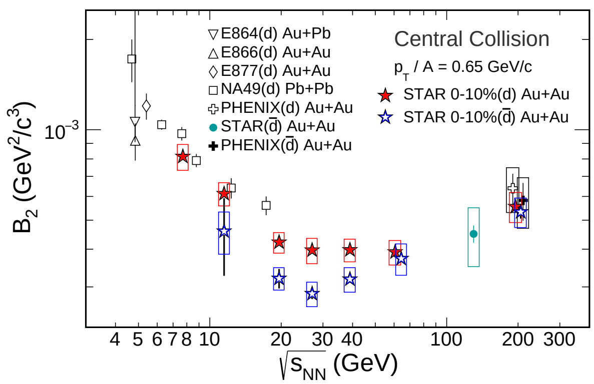

Figure 8: Collision energy dependence of the deuteron B_2 for central Au+Au collisions.

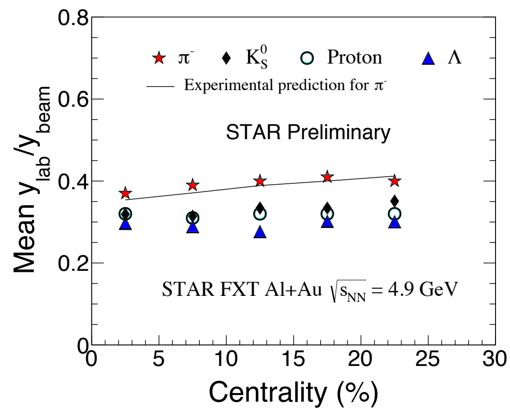

Figure 9: Peak position of rapidity density distribution dN/dy of various particles as a function of centrality in Al+Au collisions.

GeV, which might imply a change of the equation of state of the medium in these collisions.

Baryon Stopping

Understanding baryon stopping is key to understanding the baryon chemical potential of the dense medium produced in heavy-ion collisions, and asymmetric systems provide valuable insights into the stopping mechanisms which are often characterized as either the rapidity loss of projectile baryons or rapidity gain of target baryons [20]. In 2015, as part of STAR's fixed-target tests, Al(beam)+Au(target) collisions at $\sqrt{s_{\mathrm{NN}}} = 4.9$ GeV were collected. The transverse mass spectra and rapidity density distributions (dN/dy) for the strange ($K0_S$ and Λ) and charged hadrons (protons and pions) over a rapidity interval of $0.2<|y_{\mathrm{lab}}|<1.8$ have been measured and are consistent with those from Si+Au and Si+Pb collisions from the E802, E810 and E814 experiments at the AGS [21, 22, 23, 24, 25, 26, 27].

The peak position of the rapidity density distribution, dN/dy, of various particles as a function of centrality is shown in Fig. 9. In this asymmetric Al+Au system, the dN/dy peak position of π^- appears to be consistent with the interaction zone rapidity, which varies with centrality. For K^0_S, the peak is consistently 0.089 ± 0.026 units of rapidity less than that of the pions. The measured baryons, protons and Λ, whose dN/dy peak positions are used to measure the baryon stopping, have an average rapidity gain ($\delta y = y_{\mathrm{peak}} - y_{\mathrm{target}}$) of ~ 1 unit of rapidity.

Dileptons

Dileptons are good probes of the hot QCD medium created in heavy-ion collisions since they are not affected by the strong interaction. As a result, leptons can traverse the hot medium with minimal final-state effects, providing means to experimentally test models that predict chiral symmetry restoration, and enabling a better understanding of the microscopic properties of QCD matter. The RHIC BES-I program provided a unique opportunity to systematically test calculations as a function of the initial collision energy. The p_{T} integrated

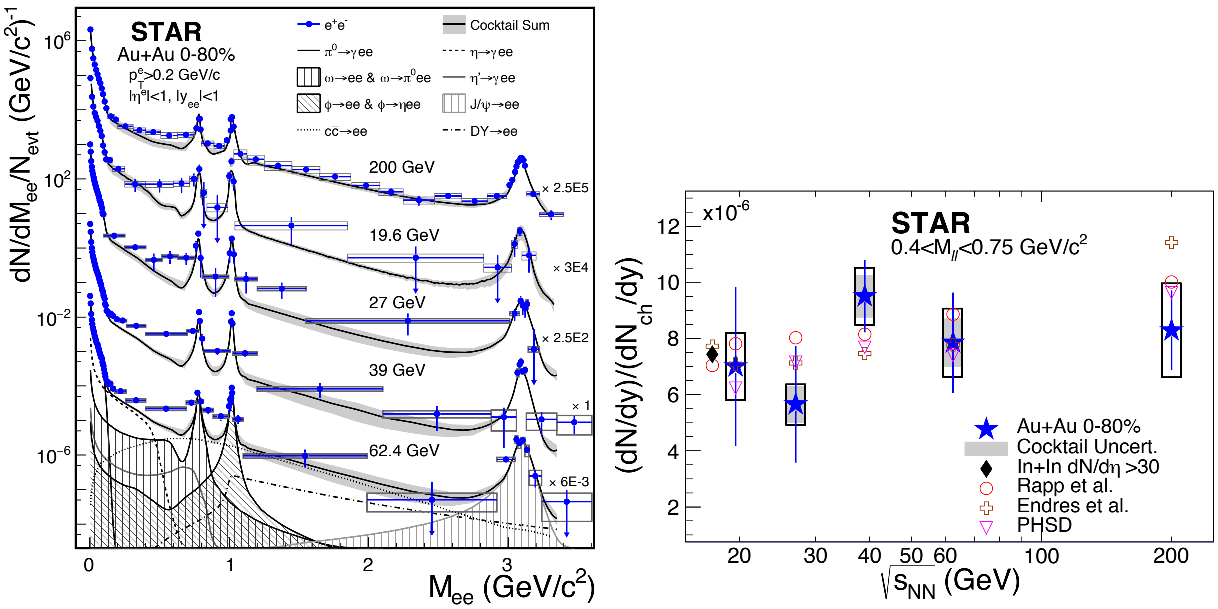

Figure 10: (Left) Background subtracted dielectron invariant mass spectra from $\sqrt{s_{\rm NN}}$ = 19.6, 27, 39, 62.4, and 200 GeV 0−80% most-central Au+Au collisions . compared to the hadronic cocktails (gray bands). The cocktail components for $\sqrt{s_{\rm NN}}$ = 62.4 GeV are also shown. (Right) Collision energy dependence of the integrated dilepton excess yields in $0.4 < M_{ll} < 0.75$ GeV/c^2, normalized by dN_{ch}/dy. The closed markers represent the experimental measurements while the open markers represent the model calculations.

dilepton spectra are shown in the left panel of Fig. 10 for 0−80% Au+Au collisions in various collision energies; these data have been submitted for publication [28].

To allow for a direct comparison of our measurements with previously published results and model calculations, we integrated the acceptance-corrected dielectron excess spectra. The right panel of Fig. 10 shows the integrated excess yields in the low mass region (0.4< M_{ll} <0.76 GeV/c^2) normalized by dN_{ch}/dy as a function of collision energy. Our data show no significant collision-energy dependence for the 0-80% Au+Au collisions, consistent with models that include ρ meson broadening in the approach to chiral symmetry restoration.

Strong electromagnetic fields arising from the relativistic contraction and large amount of charges in the nuclei generate a large flux of high-energy quasi-real photons. Dileptons therefore can also be produced in these type photon-photon and photonuclear interactions. Dilepton production from either photon-photon or coherent photonuclear processes are known to be distinctly peaked at very low transverse momenta. Recently, STAR published a paper on the measurement of inclusive e^+e^- pair production at low $p_{\rm T} < 0.15$ GeV/c in Au+Au collisions at $\sqrt{s_{\rm NN}}$ =200 GeV and U+U collisions at $\sqrt{s_{\rm NN}}$ =193 GeV [29]. The left plot of Fig. 11, panel (a) presents the efficiency-corrected e^+e^- invariant mass spectra in Au+Au and U+U collisions for pair $p_{\rm T} < 0.15$ GeV/c for different centrality bins. The ratios of data over cocktail that describes the enhancement factors are shown in panel (b). The enhancement factor is found to be significant in the most peripheral (60-80%) collisions, and

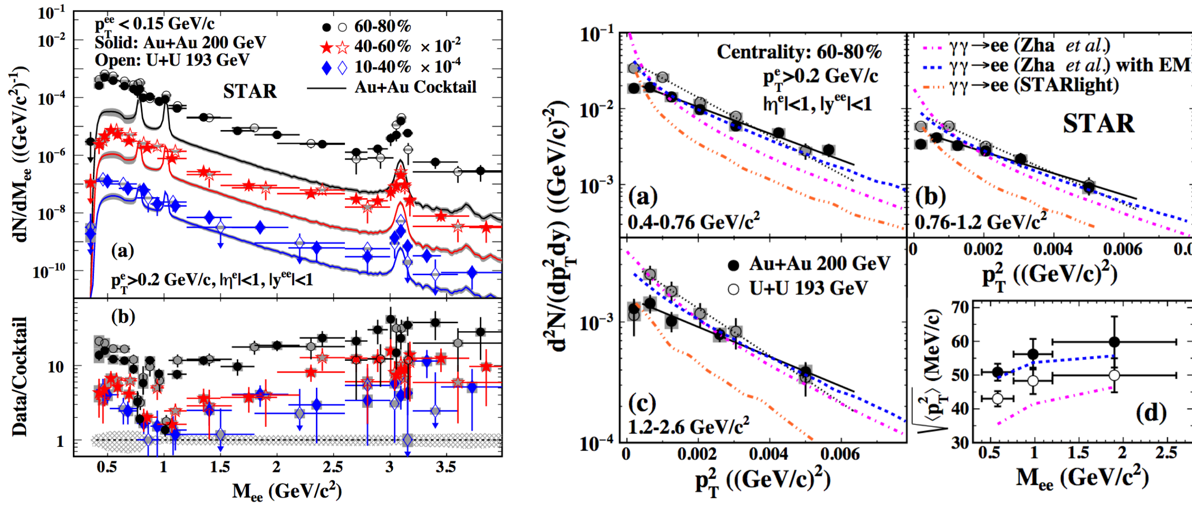

Figure 11: (Left) (a) The centrality dependence of e^+e^- invariant mass spectra from Au+Au collisions and U+U collisions for pair $p_{\rm T} < 0.15$ GeV/c. (b) The corresponding ratios of data over cocktail. (Right) The p_T^2 distributions of excess yields within the STAR acceptance in the mass regions of (a) 0.4-0.76, (b) 0.76-1.2, and (c) 1.2-2.6 GeV/c^2 in 60-80% Au+Au and U+U collisions, (d) $\sqrt{\langle p_T^2 \rangle}$ of excess yields as a function of M_{ee}.

gradually decreases in semi-peripheral (40-60%) and semi-central (10-40%) collisions.

To further explore the observed excess, $p_T^2(\sim -t)$, the squared four-momentum transfer distributions of the excess yields are shown in the right plot of Fig. 11 (a)-(c) for three different mass regions. The invariant mass dependence of the extracted $\sqrt{\langle p_T^2 \rangle}$ is plotted in Fig. 11 (d). These distributions show weak invariant mass and collision species dependencies. Based on comparisons with model calculations, the observed excess for $p_{\rm T} < 0.15$ GeV/c is likely linked to photon-photon production and represents the first observation showing the magnitude of two-photon interactions in heavy-ion collisions with hadronic overlap. In addition, model calculations of photon-photon interactions describe the observed excess yields but fail to reproduce the p_T^2 distributions.

pp Cross Sections

Elastic scattering plays an important role in *pp* scattering at high energies, which is evident by the fact that it contributes about 30% of the total cross section at the highest measured energies. With STAR we were able to study the total and elastic cross sections of *pp* collisions at $\sqrt{s} = 200$ GeV with the Roman Pot system originally constructed for the pp2pp experiment which are used to detect scattered forward protons. New differential elastic cross section results are presented in the left panel of Fig. 12 which are well described by the functional form Ae^{-Bt} with the slope parameter $B = 14.32 \pm 0.09^{+0.20}_{-0.33}\,\mathrm{GeV}^{-2}$. This study does not reveal evidence of a non-linear term in the exponent of σ_{el}, which has been reported

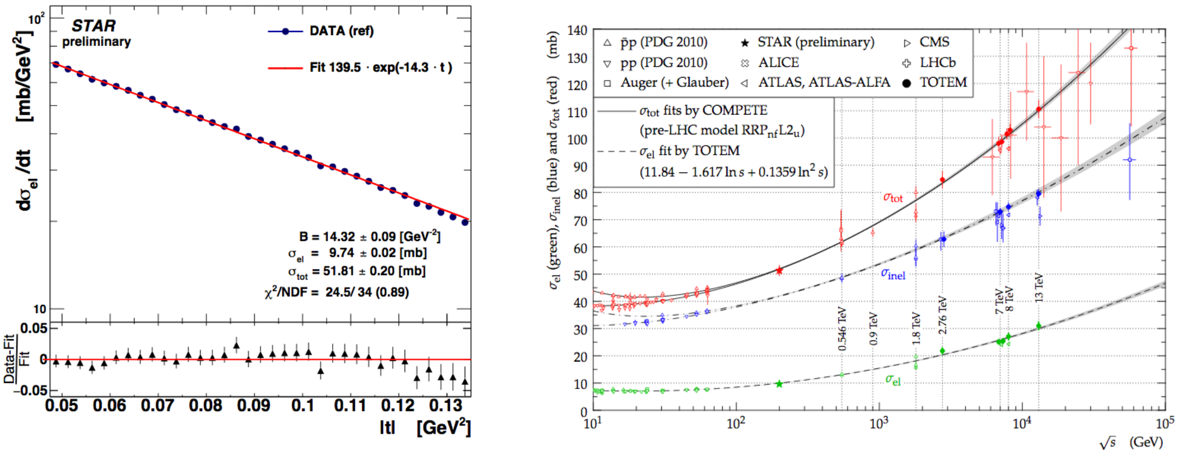

Figure 12: (Left) Corrected pp elastic differential cross-section $d\sigma/dt$ fitted with a exponential function $A\exp^{-Bt}$. (Right) Comparison of STAR result on σ_{el} and σ_{tot} with the world data.

by the TOTEM collaboration at center of mass energy of 8 TeV collisions at the LHC [30]. The total pp cross section is obtained by extrapolating the measurement to the non-detected t–region using the optical theorem. This result is compared with the world data for other energies shown in the right panel of Fig. 12 [31].

Bulk Correlations & Fluctuations

Long-Range Collectivity in Small Collision System
Recent measurements at both the LHC [32, 33] and RHIC [34, 35] have discovered and confirmed the presence of long-range two-particle angular correlations, called the "ridge", in high-multiplicity pp and p/d/^{3}He+A collisions. STAR has studied the beam energy dependence of p+Au and d+Au collisions to gain further insights on the ridge physics. The observed anisotropy in these systems provides new information to address the physics origin of ridge, as well as to expose possible limitations to the fluid dynamical description of the matter created in these collisions.

The magnitude of the associated azimuthal anisotropy can be obtained from a Fourier decomposition of the azimuthal angle distribution of the emitted hadrons. A template fitting method [36] employed to subtract non-flow contributions to the two-particle correlations, allows the extraction of the anisotropy coefficients (v_n) for these systems at their respective energies. Figure 13 shows the integral v_2 results as a function of $\langle dN_{\mathrm{ch}}/d\eta\rangle$ without (left) and with (right) subtracting non-flow contributions in d+Au collisions from 19.6 to 200 GeV and p+Au at 200 GeV. The values of both v_2 and $\langle dN_{\mathrm{ch}}/d\eta\rangle$ were evaluated for charged hadrons with $0.2 < p_{\mathrm{T}} < 3.0$ GeV/c and $|\eta|$ <0.9 in each data set. The results after non-flow subtraction show similar magnitudes and trends for v_2 values extracted at similar $\langle dN_{\mathrm{ch}}/d\eta\rangle$

regardless of beam energy and collision system. This observation is consistent with the expected trend for the dominance of final-state viscous attenuation at low $\langle dN_{\rm ch}/d\eta \rangle$ [37].

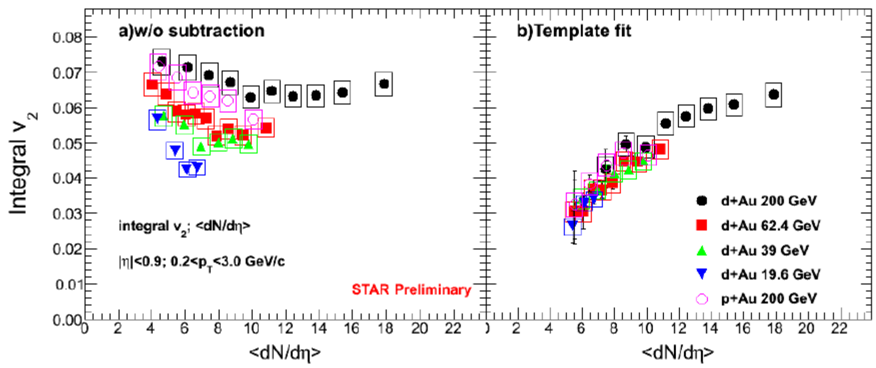

Figure 13: (Left) The integral v_2 without and (Right) with template fitting non-flow subtraction as a function of $\langle dN_{\rm ch}/d\eta \rangle$ in p+Au and d+Au collisions. Results are shown for several beam energies as indicated.

Polarization Along the Beam Direction

The matter created in non-central heavy-ion collisions should exhibit rotational motion in order to conserve the initial angular momentum carried by the two colliding nuclei. The direction of the angular momentum is perpendicular to the reaction plane, as defined by incoming beam and the impact parameter vector. It was predicted [38, 39] that such a spinning motion of the matter would lead to a net spin polarization of particles produced in the collisions due to spin-orbit coupling. STAR observed positive polarizations of Λ hyperons [40, 41], where the signal increases with decreasing energies from 200 down to 7.7 GeV. Anisotropic flow, characterized by the Fourier coefficients of the particle azimuthal distribution in the transverse plane, has been extensively studied in heavy-ion collisions and was found to be well described by hydrodynamic calculations [42, 43]. The observation of the large second-order coefficients of elliptic flow in mid-central collisions indicates significantly stronger expansion in the reaction plane direction compared to that out-of-plane. Such nontrivial velocity fields may lead to a quadrupole structure in the z-component of vorticity depending on the azimuthal angle relative to the reaction plane [44, 45].

STAR has measured the Λ hyperon polarization along the beam direction, P_z, for the first time in Au+Au collisions at $\sqrt{s_{\rm NN}} = 200$ GeV. Figure 14 (left) shows the finite signals of a quadrupole modulation of both Λ and $\bar{\Lambda}$ polarization along the beam direction which are qualitatively consistent with the expectation from the vorticity component along the beam direction due to the elliptic flow. Figure 14 (right) shows a strong centrality dependence of the longitudinal polarization results. The increase of the signal with centrality is likely due to increasing elliptic flow contributions in peripheral collisions. The experimental results are also compared to calculations from AMPT model [46], which show the opposite phase of the modulation and overpredict the magnitude of the polarization (opposite phase also predicted by hydrodynamic model [47]). On the other hand, the blast-wave model predicts the correct phase of P_z modulation and the version with HBT radii included in the fit also reasonably describe the centrality dependence.

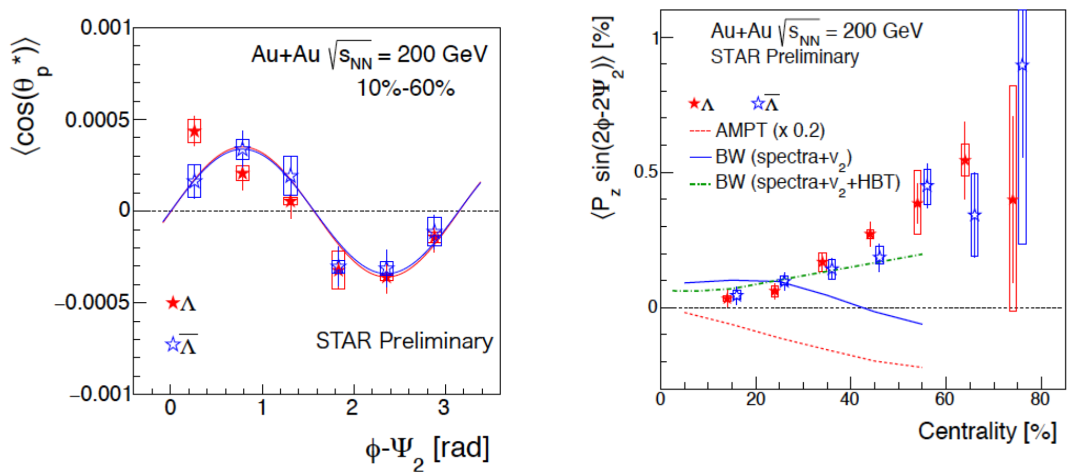

Figure 14: (Left) $\langle \cos\theta_p^* \rangle$ proportional to the longitudinal component of the polarization ($P_z =< cos\theta^* > /(3\alpha)$) is shown for Λ and $\bar{\Lambda}$ as a function of azimuthal angle ϕ relative to the second-order event plane Ψ_2 for 20%-60% centrality bin in Au+Au collisions at 200 GeV. (Right) The second Fourier sine coefficient of the polarization of Λ and $\bar{\Lambda}$ along the beam direction as a function of the collision centrality in Au+Au collisions at 200 GeV.

Sixth-Order Cumulant of Net-Particle Multiplicity Distributions

The ratios of the cumulants of identified net-particle multiplicity distributions have been predicted to be sensitive to the onset of Quantum Chromodynamics (QCD) phase transition and to the additional fluctuations expected from the close proximity to the critical point [48, 49]. Generally, high-order cumulants are more sensitive to the chemical freeze-out conditions than particle yields. The 6^{th}-order fluctuations, C_6/C_2, are predicted to be sensitive to the crossover as well as the critical point [50]. The lattice QCD calculation and $O(4)$ scaling function [51] predict a negative value of C_6/C_2 for net-charge and net-baryon distributions if the chemical freeze-out is close enough to the chiral phase transition at the beam energy of $\sqrt{s_{NN}} \leq 60$ GeV [52, 50].

STAR has now measured the sixth-order cumulant of net-charge and net-proton distributions at 200 GeV and 54.4 GeV, $0.4 < p_T < 2.0$ GeV/c with corrections for detector inefficiency effects under the assumption that efficiencies follow a binomial distribution [53]. Figure 15 shows C_6/C_2 as a function of centrality at $\sqrt{s_{NN}} = 54.4$ and 200 GeV. It is found that the $C_6/C_2 > 0$ at $\sqrt{s_{NN}} = 54.4$ GeV, while $C_6/C_2 < 0$ at $\sqrt{s_{NN}} = 200$ GeV in central collisions. This result is qualitatively consistent with the theoretical prediction [54], which could indicate the experimental evidence of the crossover at $\sqrt{s_{NN}} = 200$ GeV. The experimental results are also compared with lattice QCD calculations, as a proxy for $\mu_B \sim 0$ MeV, which show that both calculations are negative in central collisions. In addition, UrQMD results at $\sqrt{s_{NN}} = 200$ GeV show $C_6/C_2 > 0$ for all centralities, indicating that $C_6/C_2 < 0$

cannot be realized by the hadron transport model.

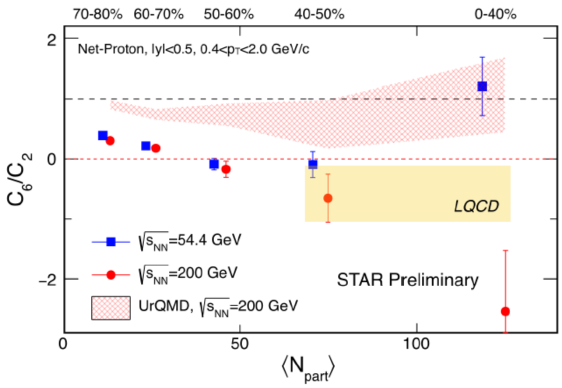

Figure 15: The 6^{th}-order fluctuations, C_6/C_2, of the net-proton multiplicity distributions at $\sqrt{s_{\rm NN}} = 54.4$ and 200 GeV as a function of centrality. The red band represents UrQMD results at $\sqrt{s_{\rm NN}} = 200$ GeV.

STAR has also done the first measurement [55] of the off-diagonal cumulants up to the 2^{nd}-order between net-p, net-K and net-Q, which provide additional constraints on the chemical freeze-out conditions [56]. Figure 16 (left) shows the normalized off-diagonal cumulants which probe the correlations between net-proton and net-kaon ($C_{p,k}$), net-charge and net-kaon ($C_{Q,k}$), net-charge and net-proton ($C_{Q,p}$), as a function of beam energy for $0.4 < p_{\rm T} < 1.6$ GeV/c in 0-5% and 70-80% centralities. The Poisson baseline and UrQMD results are shown as dotted lines and shaded bands, respectively. $C_{p,k}$ is found to be described well by UrQMD, while significant excess of $C_{Q,k}$ and $C_{Q,p}$ is observed with respect to the Poisson baseline and UrQMD expectations.

Two-Particle Angular Correlations

The two-particle angular correlation function, R_2, is defined by the two particle multiplicity density in the relative (pseudo)rapidity and azimuthal angle, $(\Delta y, \Delta\varphi)$, normalized by the single particle multiplicity densities. R_2 reflects the dynamics of heavy-ion collisions in both the longitudinal and azimuthal directions [57]. The study of different particle species pairs allows us to compare the meson and baryon correlations, while a beam energy dependence study may indicate non-monotonic behavior possibly related to a critical point.

STAR has measured two-particle correlations for like-sign and unlike-sign identified pions, kaons and protons in Au+Au collisions in the BES-I program, and in different centralities from the most central 0-5% to the most peripheral 70-80%, and two ranges of low and high transverse momentum. Figure 16 (right) shows the projections of the angular correlation functions onto the relative rapidity axis (integrated over all azimuthal angles) for like-sign and unlike-sign proton pairs in 30-40% central collisions. The proton pair correlations are found to differ significantly from those of the pion and kaon pair correlations at all eight energies and for both like-sign and unlike-sign charge combinations [58]. The pion and kaon correlations show an enhancement around $\Delta y \sim 0$ resulting from short-range mechanisms, and decrease as the collisions become more central. In contrast, both the like-sign and unlike-sign proton correlation functions show a $p_{\rm T}$-independent anticorrelation near $\Delta y \sim 0$ at all eight energies, weakly decreasing with increasing beam energy and decreasing as the collisions become more central. This behavior is observed for the first time in an A+A colli-

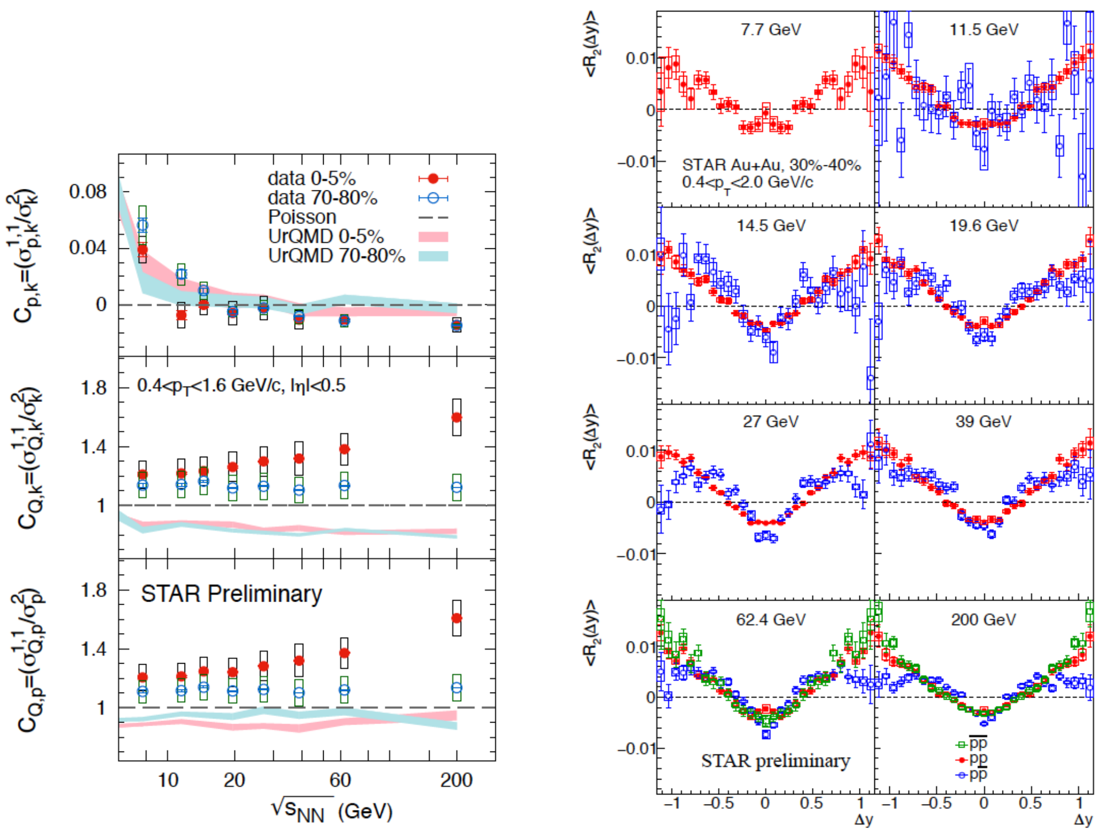

Figure 16: (Left) Beam energy dependence of $C_{p,k}$, $C_{Q,k}$ and $C_{Q,p}$ in 0-5% and 70-80% centralities and $|\eta| < 0.5$. The dotted lines represent the Poisson baseline, while the shaded bands represent the UrQMD expectations. (Right) Projection of correlation function $\langle R_2(\Delta y)\rangle$ of like-sign (red) and unlike-sign (blue) proton pairs in Au+Au collisions at 30-40% centrality and eight different energies from 7.7 GeV (top left) to 200 GeV (bottom right). Also shown at the highest beam energies in the right frames are the $\overline{p}\overline{p}$ correlations.

sion system. Non-monotonic behavior is not observed in the two-particle angular correlation functions of any particle specious as a function of the beam energy from $\sqrt{s_{\mathrm{NN}}} = 7.7$ to 200 GeV. The experimental results are also compared to those obtained from the models, such as UrQMD, Hijing, and AMPT. The model comparisons imply that the anticorrelations in the unlike-sign proton pairs result from baryon-antibaryon annihilation, but the cause of such a strong and longe-range anticorrelation in like-sign proton pairs is still unknown.

Chiral Magnetic Effect

Quark interactions with fluctuating topological gluon field can induce chirality imbalance and local parity violation in quantum chromodynamics (QCD) [59]. In relativistic heavy-ion collisions, this can lead to electric charge separation in the presence of a strong magnetic field ($\vec{B}$), a phenomenon known as the chiral magnetic effect (CME) [60]. Extensive theoretical and experimental efforts have been devoted to the search for the CME-induced charge separation along $\vec{B}$ in heavy-ion collisions [61, 62]. The commonly used observable to search for the CME-induced charge separation is the three-point azimuthal correlator difference, $\Delta\gamma = \gamma_{OS} - \gamma_{ss}$; $\gamma = \langle cos(\phi_\alpha + \phi_\beta - 2\Psi_{RP})\rangle \approx \langle cos(\phi_\alpha + \phi_\beta - 2\phi_c)\rangle / v_2$, where ϕ_α and ϕ_β are the azimuthal angles of two charged particles, of opposite electric charge sign (OS) or same sign (SS), and Ψ_{RP} is that of the reaction plane to which $\vec{B}$ is perpendicular on average. The latter is often surrogated by the azimuthal angle of a third particle, Φ_c, with a resolution correction factor given by the particle's elliptical anisotropy (v_2) [60].

Charge separation measurements by the three-point azimuthal correlator ($\Delta\gamma$) are contaminated by major backgrounds arising from resonance decay correlations coupled with the elliptical anisotropy (v_2). To reduce background contaminations, STAR has employed several methods [63, 64, 65, 66] such as the $\Delta\gamma$ correlator as a function of the particle pair invariant mass (m_{inv}), and the comparative $\Delta\gamma$ measurements with respect to Ψ_{RP} (estimated

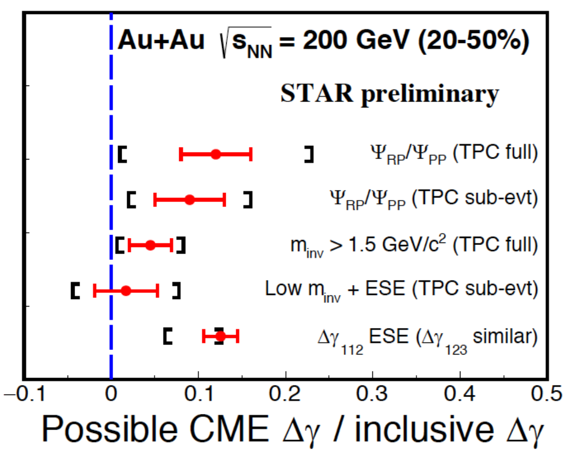

Figure 17: The possible CME $\Delta\gamma$ over the inclusive $\Delta\gamma$ fraction from different analysis methods in middle central (20-50%) Au+Au collisions at $\sqrt{s_{\rm NN}} = 200$ GeV. Horizontal bars are statistical errors and caps are systematic uncertainties.

by ZDC) and Ψ_{PP}(estimated by TPC). Figure 17 summarizes the extracted potential CME signal fractions (CME $\Delta\gamma$ over the inclusive $\Delta\gamma$) in mid-central (20-50%) Au+Au collisions at $\sqrt{s_{\rm NN}} = 200$ GeV. These data-driven estimates indicate that the possible CME signal is small.It is expected that the precision can be improved in the future with more Au+Au data and the new isobar run.

Other Publications Since 2018 PAC

STAR has also published the collision energy dependence of $p_{\rm T}$ correlations in Au+Au collisions at RHIC and showed that the relative dynamical correlations for Au+Au collisions at $\sqrt{s_{\rm NN}} = 200$ GeV has a power law dependence on the number of participant nucleons and agree with the results for Pb+Pb collisions at $\sqrt{s_{\rm NN}} = 2.76$ TeV from ALICE. As the collision energy is lowered from $\sqrt{s_{\rm NN}} = 200$ GeV to 7.7 GeV, the centrality dependence of the relative dynamical correlations departs from the power law behavior observed at the higher collision energies [67]. Proton-Omega correlation function in Au+Au collisions at $\sqrt{s_{\rm NN}} = 200$ GeV has been studied by STAR and showed that the measured ratio of proton-Ω correlation function from peripheral (small system) to central (large system) collisions is less than unity for relative momentum smaller than 40 MeV/c. Comparison of measured correlation ratio with the theoretical calculation slightly favors a proton-Ω bound system with a binding energy of $\sim$ 27 MeV [68]. Moreover, STAR has studied constraining the initial conditions and temperature dependent transport with three-particle correlations in Au+Au collisions which provides additional information about the initial geometry, the nonlinear hydrodynamic response of the medium and constrain temperature dependence of η/s. The centrality dependence of $C_{1,2,3}$ for the first time reveals a possible coupling between directed, elliptic, and triangular harmonic flow, which arises from fluctuations in the initial geometry [69].

Jet Measurements

Jets have been a useful tool to study the properties of QGP. With the help of newly developed techniques and significantly increased statistics in recent RHIC runs, STAR has explored various aspects of jets in heavy ion and *pp* collisions.

Tagged Semi-inclusive Jets

The semi-inclusive distributions of charged-particle jets recoiling from high transverse momentum hadron triggers have been studied with STAR previously [70]. The results showed a significant suppression in the recoil jet yield in central collisions relative to peripheral collisions. Based on the techniques developed for the semi-inclusive jet analysis, STAR has recently measured semi-inclusive charged-particle jets recoiling from direct photon ($\gamma_{\rm dir}$) and π^0 meson triggers. The direct photons that are produced in coincidence with recoil jets ($\gamma_{\rm dir}$+jet) are considered to be an ideal probe of the parton energy loss in the medium produced in heavy ion collisions, as $\gamma_{\rm dir}$ do not interact with the medium via strong interactions and the initial energy of the parton is expected to be preserved in the energy of the $\gamma_{\rm dir}$. Figure 18 shows the ratio of recoiled jet yields (Y) in central Au+Au collisions and PYTHIA

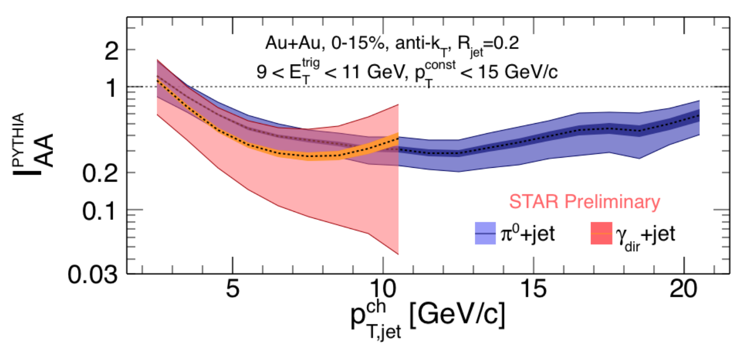

Figure 18: $I_{\rm AA}^{\rm PYTHIA}$ for $\gamma_{\rm dir}$- (red band) and π^0-trigger (blue band) recoiling charged-particle jets with $9 < E_{\rm T}^{\rm trig} < 11$ GeV in Au+Au collisions at $\sqrt{s_{\rm NN}} = 200$ GeV. Lighter and darker bands correspond to systematic and statistical uncertainties, respectively.

simulations as a proxy for *pp* collisions for $\gamma_{\rm dir}$ and π^0 triggers as a function of recoiling jet's transverse momentum, i.e. $I_{\rm AA}^{\rm PYTHIA}(p_{\rm T,jet}^{\rm ch}) = Y^{\rm Au+Au}(p_{\rm T,jet}^{\rm ch})/Y^{\rm PYTHIA}(p_{\rm T,jet}^{\rm ch})$. A strong suppression is observed in similar magnitudes for both $\gamma_{\rm dir}$+jet and π^0+jets for the kinematic range studied for $R = 0.2$ anti-$k_{\rm T}$ jets.

Differential Dijet Imbalance

The dijet imbalance measured by $|A_J| = |p_{\mathrm{T}}^{\mathrm{lead}} - p_{\mathrm{T}}^{\mathrm{sublead}}|/(p_{\mathrm{T}}^{\mathrm{lead}} + p_{\mathrm{T}}^{\mathrm{sublead}})$ can quantify the transverse momentum imbalance between back-to-back leading and subleading jet pairs. The jet pairs reconstructed with high transverse momentum (> 2 GeV/c) constituents (hard-core jets) were observed to have a strong imbalance in Au+Au collisions [71]. However, the momentum balance is restored when such jets are reconstructed again with their softer constituents (matched jets) [71]. STAR has recently extended the $|A_J|$ measurement in Au+Au

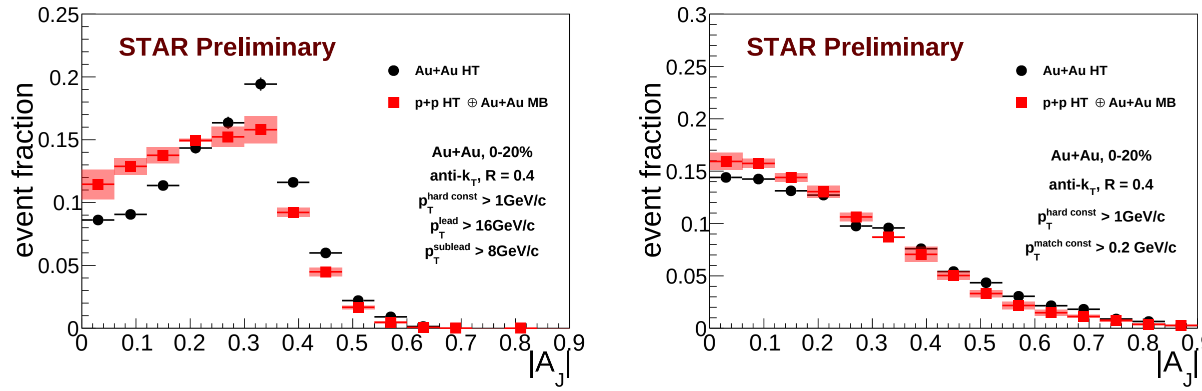

Figure 19: (Left) $|A_{\mathrm{J}}|$ distributions for Au+Au and *pp* embedded in Au+Au, with $p_{\mathrm{T}}^{\mathrm{const}} > 1.0$ GeV/c for hard-core dijets and (Right) matched dijets.

collisions for various parameters and compared them with those in *pp* that are embedded in the corresponding Au+Au events. Figure 19 shows the preliminary $|A_J|$ distributions with $p_{\mathrm{T}}^{\mathrm{const}} > 1.0$ GeV/c for hard-core jets and $R_{\mathrm{jet}} = 0.4$. While hard-core jets are observed to be modified in Au+Au collisions in all R_{jet} with respect to *pp*, matched jets show a smooth transition from statistically different distributions of $|A_J|$ at low R_{jet} (from 0.2) and low $p_{\mathrm{T}}^{\mathrm{const}}$ (from 1.0 GeV/c) to statistically similar distributions at larger R_{jet} (up to 0.4) and higher $p_{\mathrm{T}}^{\mathrm{const}}$ (up to 3.0 GeV/c). These results demonstrate that we can select the level of jet modification in heavy ion collisions relative to a *pp* reference by modifying the dijet definition with a connection to the in-medium path-length dependence of partonic energy loss.

Two Particle Correlations

Two-particle angular correlations have been widely used in the field of heavy ion physics, particularly for characterization of jet quenching in heavy ion collisions. Depending on the trigger and associated particle selections, they may explore different aspects of jet properties.

Recently STAR has utilized D^0-mesons and unidentified charged particles as trigger and associated particles, respectively, for an analysis of two-particle angular correlations in $\sqrt{s_{\mathrm{NN}}} = 200$ GeV Au+Au collisions. Open heavy-flavor hadrons are a unique probe of the QGP due to their large mass and early production. The Heavy Flavor Tracker (HFT) provides an excellent identification of $D^0(\bar{D}^0)$ via the weak decay channels, $D^0 \to K^-\pi^+$ ($\bar{D}^0 \to K^+\pi^-$) [72]. The correlation structures on relative pseudorapidity and azimuth

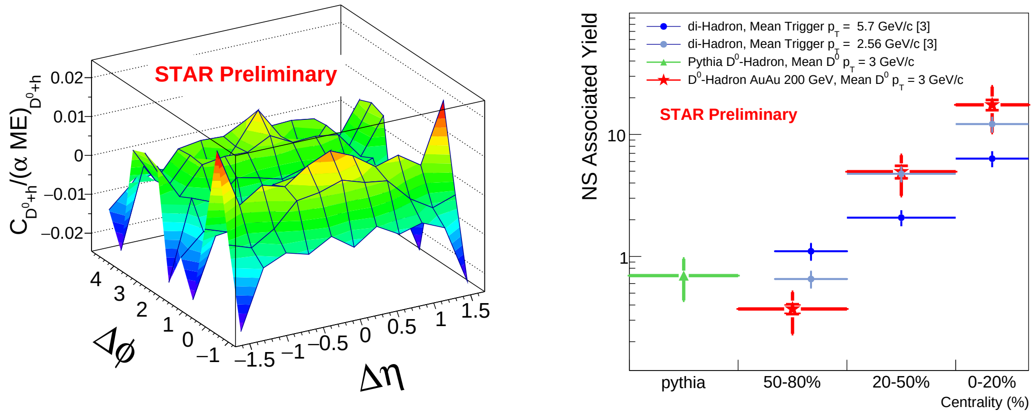

Figure 20: (Left) D^0-hadron correlation function for 50-80% centrality class and (Right) correlated hadron yield per D^0 trigger in the near-side peak in Au+Au collisions at $\sqrt{s_{\mathrm{NN}}} = 200$ GeV. PYTHIA [73] and di-hadron [74] results are compared in the yield plot.

$(\Delta\eta, \Delta\phi)$ have been investigated for various centrality classes (e.g., Fig. 20 left for 20-50% centrality class). In such two-particle correlations, the near-side ($\Delta\phi = \phi_{\mathrm{trig}} - \phi_{\mathrm{asso.}} \sim 0$) structure serves as a proxy for a jet containing a charm quark. In order to isolate the correlation structure originating from jets from other physics mechanisms, a 2-dimensional fitting model [75] is applied. The resultant near-side (NS) associated yields for different centrality classes are plotted on the right panel of Fig. 20. These results are compared with similar measurements using unidentified hadrons, primarily light-flavor hadrons, with similar trigger particle p_{T} [74], and no significant difference in the NS yields and widths are observed. These results complement STAR's previous studies on D^0 mesons and provide an additional hint of the interaction of D^0-mesons with the medium created in heavy ion collisions.

Another two-particle correlation analysis has investigated the jet interactions relative to the second-order event plane (Ψ_2). Compared to the hadron-hadron correlations, jet-hadron correlations generally contain less surface bias and the trigger particles constrain the initial parton energy better. Event-plane dependent measurements also enable us to explore the path length dependence of jet modification in the QGP. Figure 21 shows the near-($\Delta\phi \sim 0$) and away-side ($\Delta\phi \sim \pi$) yields for three different azimuthal ranges of jets relative to the event plane, $0 < |\psi_{\mathrm{jet}} - \Psi_2| < \pi/6$ for in-plane, $\pi/6 < |\psi_{\mathrm{jet}} - \Psi_2| < \pi/3$ for mid-plane, and $\pi/3 < |\psi_{\mathrm{jet}} - \Psi_2| < \pi/2$ for out-of-plane, as a function of associated particle p_{T}. The results indicate no significant event-plane dependence within the current uncertainties. This may be due to larger contributions of fluctuations to jet energy loss which smear the expected effects of path-length dependence. The di-hadron correlation relative to the event plane in heavy ion collisions [76] has been extended by applying the event-shape engineering techniques. In [76], the away-side correlation structure was observed to have strong modification in heavy ion collisions. This showed a significant dependence on the trigger hadron azimuthal angle relative to the event plane providing hints of path length dependence of jet quenching. Event-shape engineering, which further classifies events in the

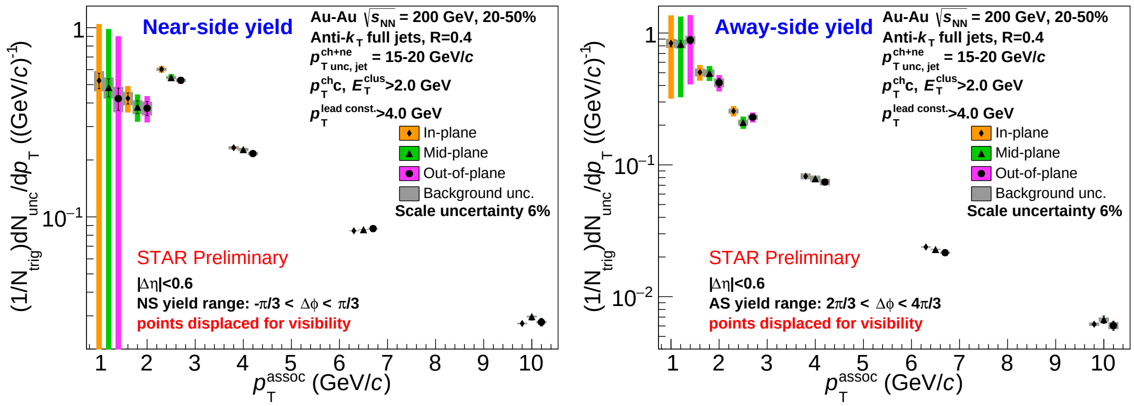

Figure 21: (Left) The near-side and (Right) away-side yields for $R = 0.4$ full jets in Au+Au collisions at $\sqrt{s_{\rm NN}} = 200$ GeV for 20-50% centrality class.

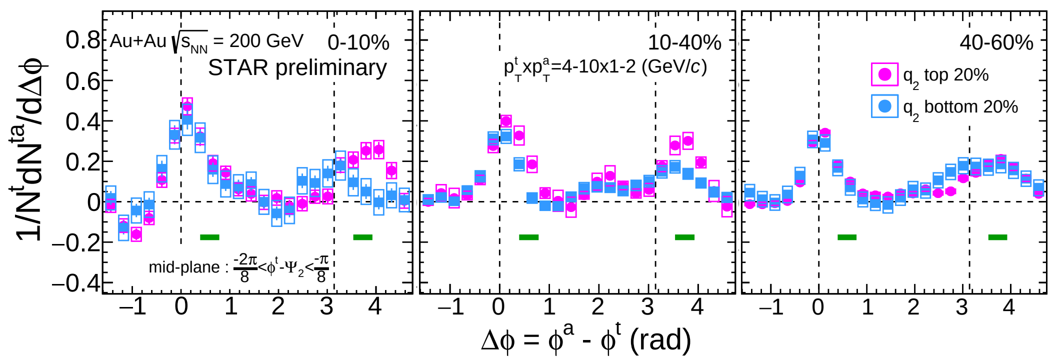

Figure 22: (Left) Di-hadron correlation functions from top 20% q_2 (magenta) and bottom 20% q_2 (azure) events for 0-10%, (Mid) 10-40%, and (Right) 40-60% centrality classes in Au+Au collisions at $\sqrt{s_{\rm NN}} = 200$ GeV. Trigger hadrons and associated hadrons are selected with $4 < p_{\rm T} < 10$ GeV$/c$ and $2 < p_{\rm T} < 4$ GeV$/c$, respectively, and the green line at $\pi/8 < \Delta\phi < 2\pi/8$ indicates the event plane direction. Statistical and systematic uncertainties are indicated with lines and boxes, respectively. The green bars at y $\sim$ 0.2 indicate the event-plane directions.

same centrality class based on the magnitude of the flow vector (q_2) [77], allows additional control on the initial collision geometry. STAR has performed extensive measurements of di-hadron correlations in $\sqrt{s_{\rm NN}} = 200$ GeV Au+Au collisions, varying centrality, q_2 of events, azimuthal angle of the trigger hadron relative to the event plane ($\phi^{\rm t} - \Psi_2$), and $p_{\rm T}$ of trigger and associated hadrons.

Figure 22 shows an example of the results, where correlation functions from top 20% q_2 and bottom 20% q_2 events are compared in three centrality classes with the same trigger and associated hadron $p_{\rm T}$ and $\phi^{\rm t} - \Psi_2$. Background flow contributions up to the forth order harmonic flow are subtracted following the procedure described in [76]. Larger shift of the away side peak position is observed in larger q_2 events, and such shift is more evident in more central events. This may suggest jet-medium coupling, and the overall results will provide a new insight on jet-medium interaction in the expanding system.

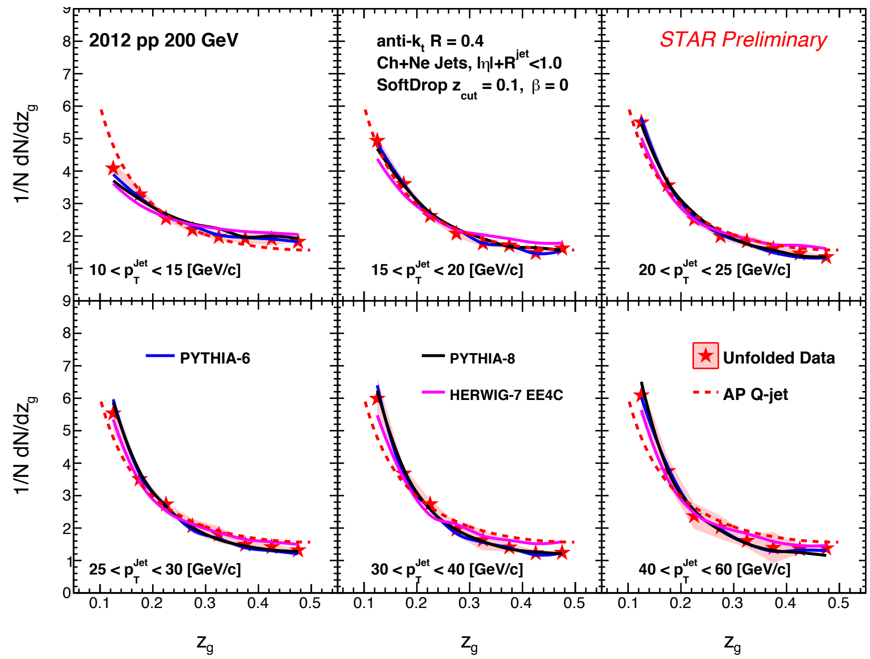

Figure 23: SoftDrop z_g distributions in pp collisions at $\sqrt{s} = 200$ GeV$/c$ for varying jet p_{T}.

Jet Sub-structure

Jets have two intrinsic scales in their evolution, the angular and momentum scales. In order to further understand jet properties depending on such scales, STAR has measured jet sub-structure observables, the SoftDrop shared momentum fraction (z_g) and the groomed jet radius (R_g) [78], in pp collisions at $\sqrt{s} = 200$ GeV. The results are corrected for detector effects via 2-dimensional Bayesian unfolding [79], and compared with leading order Monte Carlo generators, including PYTHIA-6 Perugia tune [80], PYTHIA-8 Monash [81], and Herwig-7 EE4C UE tune [82].

The z_g results are shown in Fig. 23 as an example. All models can reproduce the general trends of measured z_g, e.g., steeper z_g distributions in higher jet p_{T}.

The invariant jet mass, M, which provides access to the virtuality evolution of the hard scattered parton is also investigated in pp collisions. The corrected jet mass results are shown in Fig. 24. PYTHIA-8 and HERWIG calculations are observed to over- and under-predict jet mass, respectively.

Having established the jet sub-structure measurement baseline in pp collisions, STAR has measured the opening angle between two leading sub-jets (θ_{SJ}) [83] in Au+Au collisions at $\sqrt{s_{\mathrm{NN}}} = 200$ GeV. θ_{SJ} is essentially related to R_g, but less sensitive to the fluctuating underlying event in heavy ion collisions. Sub-jets are reconstructed with a smaller jet resolution parameter within a jet, and the two leading sub-jets correspond to the two highest p_{T} sub-jets. Larger (smaller) θ_{SJ} represents jets with wide (narrow) angular splitting. Then jets are classified based on their θ_{SJ}, and several jet observables are measured for different

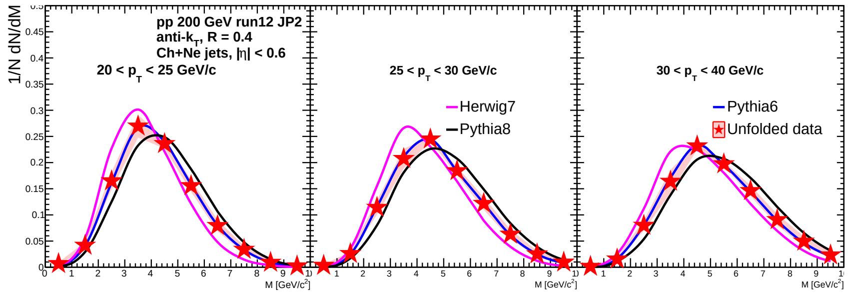

Figure 24: Invariant jet mass distributions in pp collisions at $\sqrt{s} = 200$ GeV$/c$ for varying jet p_{T}.

θ_{SJ} classes. Figure 25 shows an example, matched jet A_J for three different θ_{SJ} selections,

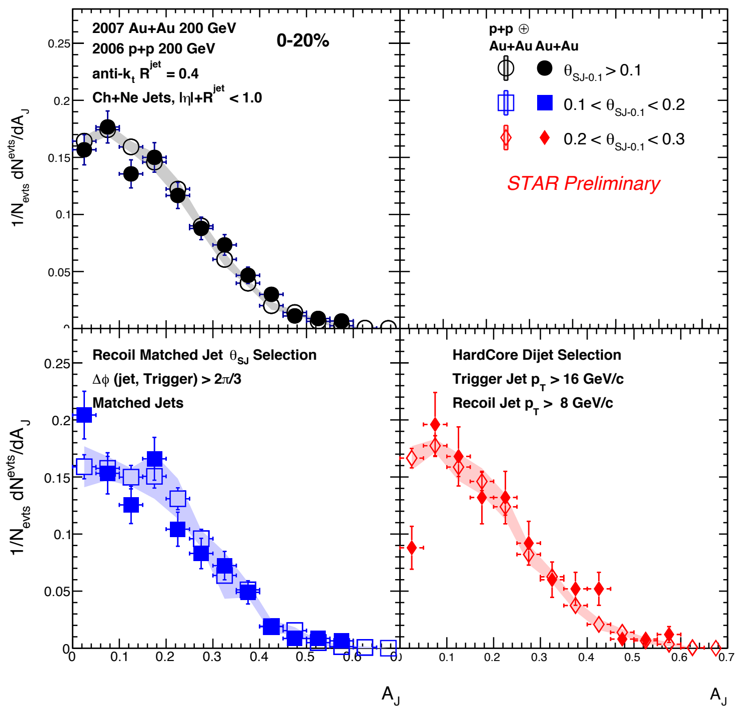

Figure 25: Matched jet dijet asymmetry (A_J) for three θ_{SJ} selections in 200 GeV Au+Au (closed markers) and pp events embedded in heavy ion collision environment (open markers).

where no significance differences are observed.

Jet shapes, the fractional transverse momentum radial distribution, have been previously measured at the LHC, and revealed a centrality-dependent modification of the jet shapes in heavy ion collisions. [84] STAR has recently measured the jet shapes in Au+Au collisions at $\sqrt{s_{\mathrm{NN}}} = 200$ GeV (see Fig. 26 for $p_{\mathrm{T}} = 20 - 40$ GeV$/c$ and in 20-50% centrality range.) For this analysis, the background contributions are estimated via an event-mixing technique and removed accordingly. The result shows clearly different radial distributions depending on

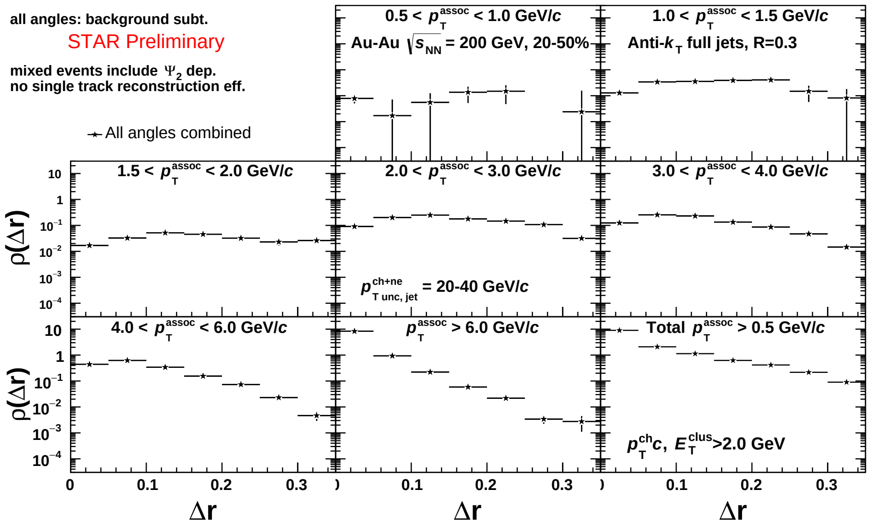

Figure 26: Jet shape distribution for anti-k_T jets with $R_{\text{jet}} = 0.3$ in 20-50% Au+Au collisions at $\sqrt{s_{\text{NN}}} = 200$ GeV. Each panel represents different p_{T} ranges of associated charged hadrons, and the bottom right plot is generated with combining all p_{T} ranges.

p_{T} of associated tracks. In order to investigate the path length dependence of modification of jets' radial energy profile, the jet shape observables are currently being investigated as a function of the azimuthal angle of jets with respect to the event plane.

1.2 Cold QCD and Spin Physics Highlights

The STAR Cold QCD program seeks to advance our understanding of the spin and flavor structure of the proton in terms of its constituent quarks and gluons, exploiting the unique capability of RHIC to provide longitudinally and transversely polarized *pp* collisions at multiple collision energies. Using longitudinally polarized beams, STAR probes the helicity preferences of gluons and up and down (anti-)quarks, to determine the individual contributions to the total spin of the proton. With beam polarization aligned transverse to the momentum direction, the *pp* collisions exhibit kinematic and dynamical effects that are directly sensitive to quark transversity, which can be interpreted as the net transverse polarization of quarks within a transversely polarized proton, and partonic motion within the proton. This program is complemented by studies of polarized *pp* elastic scattering and central exclusive production, in which a far-forward proton is detected intact.

Since 2009 STAR has completed several highly successful polarized *pp* runs both at $\sqrt{s} = 200$ GeV and $\sqrt{s} = 510$ GeV. The STAR sampled luminosity and the luminosity averaged beam polarization as measured by the hydrogen jet (H-jet) polarimeter are summarized in Table 5. These data sets formed the basis for several papers and new preliminary results, Table 6 summarizes the publications and preliminary results since the last year's PAC report, which are highlighted in the following sections. The results from the first two papers were discussed in the previous PAC report but have since been published in journals.

Table 5: Summary of *pp* running periods at RHIC since 2009, including center-of-mass energy, STAR's integrated luminosity and the average beam polarization for blue (B) and yellow (Y) beams from the H-jet polarimeter. Years with a single polarization value indicate both beams had the same average value.

Year	$\sqrt{s}$ (GeV)	Recorded Luminosity (pb^{-1})	Polarization Orientation	B/Y $\langle P \rangle$
2009	200	25	Longitudinal	55
2009	500	10	Longitudinal	39
2011	500	12	Longitudinal	48
2011	500	25	Transverse	48
2012	200	22	Transverse	61/56
2012	510	82	Longitudinal	50/53
2013	510	300	Longitudinal	51/52
2015	200	52	Transverse	53/57
2015	200	52	Longitudinal	53/57
2017	510	320	Transverse	55

Longitudinal Spin Program

Measurement of the longitudinal single spin asymmetry, A_L, in $W^\pm$ production was one of the initial motivations for the spin-physics program at RHIC, exploring the longitudinally polarized sea quark distributions. The final $W^\pm$ A_L results from the 2013 $\sqrt{s}$ =510 GeV data [87] are shown in Fig. 27 combined with previously published data collected by STAR in 2011 and 2012. The data have now reached a level of precision that for the first time it is possible to evaluate the individual sea quark polarizations, revealing that the polarization of $\bar{u}$ is larger than that of $\bar{d}$.

With its ability to identify $W^\pm$, STAR has released the preliminary results on the unpolarized cross-section ratio of the W^+ and W^- bosons from the STAR 2011 to 2013 data at $\sqrt{s} = 510$ GeV [91]. This unique measurement is sensitive to the un-polarized light sea quark distributions in the region of $x > 0.05$. A significant advantage of these data is that they are free of any correction and systematic uncertainties associated with the nuclear targets typically used in experiments that probe these distributions.

A combined paper from the inclusive jet and dijet A_{LL} using the 2012 510 GeV longitudinally polarized *pp* data [92, 93] is soon to be submitted to Physical Review D. The paper introduces the so-called off-axis cone method to correct for the underlying event (UE) contribution to the jet transverse energy on a jet-by-jet basis This method has been expanded to an UE corrections on dijet invariant mass, M_{inv}. The measured A_{LL} enables exploration of $\Delta g(x, Q^2)$ at $x \sim 0.015$. The inclusive jet A_{LL} (left-hand of Fig. 28) constrains the magnitude of $\Delta g(x, Q^2)$, while the four topology binned dijet A_{LL} (right-hand of Fig. 28) give information on the shape of $\Delta g(x, Q^2)$. The dijet A_{LL} is presented in four topology bins based on the pseudorapidities of the two jets.

Table 6: Summary of published papers and preliminary results since the last PAC.

Title	Journal/Conference	Dataset
Published Papers		
Longitudinal double-spin asymmetries for dijet production at intermediate pseudorapidity in polarized pp collisions at $\sqrt{s} = 200\text{GeV}$	Phys. Rev. D [85]	2009
Longitudinal double-spin asymmetries for π^0s in the forward direction for 510 GeV polarized pp collisions	Phys. Rev. D [86]	2012-13
Measurement of the longitudinal spin asymmetries for weak boson production in proton-proton collisions at $\sqrt{s}$ =510 GeV	Phys. Rev. D (R)[87]	2011-13
Transverse spin transfer to Λ and $\overline{\Lambda}$ hyperons in polarized proton-proton collisions at $\sqrt{s} = 200\text{GeV}$	Phys. Rev. D (R) [88]	2012
Improved measurement of the longitudinal spin transfer to Λ and $\overline{\Lambda}$ hyperons in polarized proton-proton collisions at $\sqrt{s} = 200\text{GeV}$	Phys. Rev. D [89]	2009
Preliminary Results		
Transverse Spin Asymmetries in the $p^{\uparrow}p \longrightarrow p\pi^0 X$ Process at STAR	DIS 2019 [90]	2015
Constraining the Sea Quark Distributions Through $W^{\pm}$ Cross Section Ratio Measurements at STAR	DIS 2019 [91]	2011-13

A recent study from the DSSV group [94] taking into account our previously published dijet A_{LL}, one with both jets within $0 < |\eta| < 0.8$ [95] and the other with at least one jet within $0.8 < |\eta| < 1.8$ [85], shows a sizable reduction on the uncertainty of $\Delta g(x, Q^2)$ and a moderate increase in $\Delta g(x)$ at $0.05 \leq x \leq 0.2$.

The longitudinal spin transfer, D_{LL}, to Λ and $\overline{\Lambda}$ hyperons is one tool to access the strange quark helicity distribution functions and the respective longitudinally polarized fragmentation function. The improved measurements of Λ and $\overline{\Lambda}$ D_{LL} from the STAR 2012 200 GeV pp data [89] are shown in Fig. 29 as a function of p_{T}. While the data do not provide conclusive evidence for a spin transfer signal, the data tend to lie below the expectation from DSV "scenario 3" [96], which is based on the extreme assumption that the quark polarized fragmentation functions are flavor-independent.

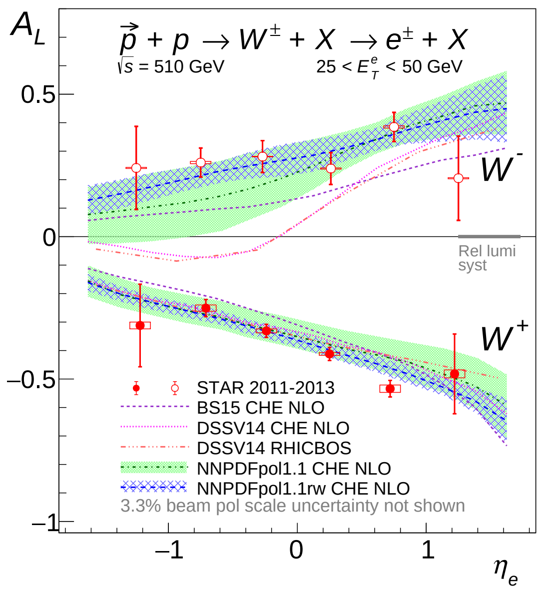

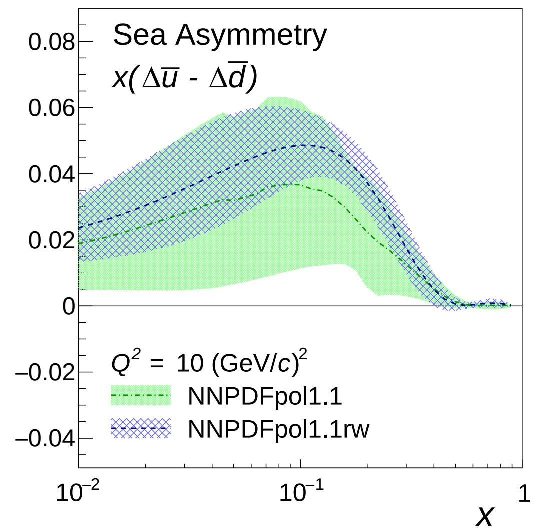

Figure 27: (Left) Longitudinal single-spin asymmetries, A_L, for $W^{\pm}$ production vs. the positron or electron pseudorapidity, η_e, for the combined STAR 2011, 2012 and 2013 data samples for 25 $< E_T <$ 50 GeV [87]. (Right) The difference of the light sea-quark polarizations vs. x at $Q^2 = 10$ $(\mathrm{GeV}/c)^2$.

Transverse Spin Program

The transverse spin transfer, D_{TT}, from polarized protons to Λ and $\overline{\Lambda}$ hyperons is sensitive to the transversity distribution of the nucleon, in particular strange quark transversity, and the Λ transversely polarized fragmentation functions. The results of the D_{TT} to Λ and $\overline{\Lambda}$ from the 2012 $\sqrt{s} = 200$ GeV [88] are consistent with zero and also with model predictions for both Λ and $\overline{\Lambda}$ (Fig. 30).

The preliminary results for the transverse spin asymmetry, A_N, from isolated pion production, $p^{\uparrow}p \rightarrow p\pi^0 X$, [90] were obtained by reconstructing π^0's from the Forward Meson Spectrometer (FMS) at $2.65 < \eta < 3.9$ and detecting the proton scattered with very small scattering angles in the STAR Roman Pots (RP). A large asymmetry is seen for pions near the proton scattering plane. In contrast, asymmetries for pions scattered away from the proton scattering plane are consistent with zero. Theory calculations are now needed to get a detailed understanding of the mechanism of isolated pion production and its asymmetry A_N.

The first extraction of transversity, $h_1(x, Q^2)$, from a global analysis of *ep* and *pp* data [97] demonstrated the uncertainty on $h_1(x, Q^2)$ is significantly reduced by including the STAR measurements of transverse spin-dependent azimuthal correlation of charged pion pairs at 200 GeV [98]. The same results at 500 GeV [99] will enable extractions of $h_1(x, Q^2)$ with comparable precision, but at much higher momentum transfer Q^2 than current semi-inclusive deep inelastic scattering (SIDIS) data. STAR has also presented the first observations of

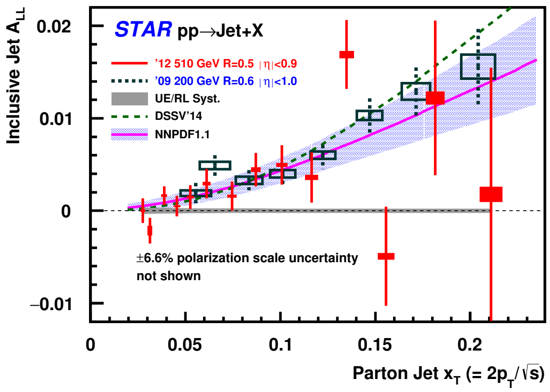

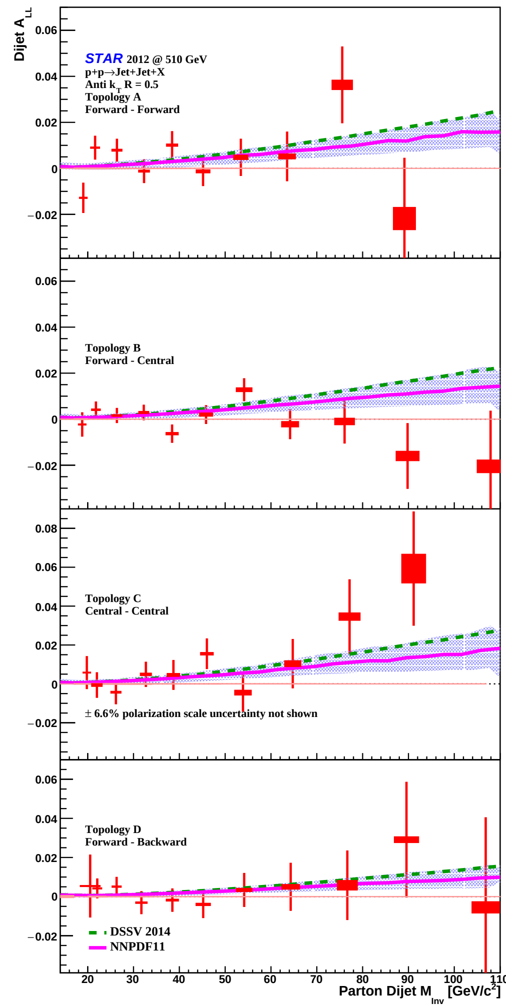

Figure 28: (Above) STAR inclusive jet A_{LL} vs. parton jet x_T compared with the STAR 2009 200 GeV data [92] and (Right) dijet A_{LL} vs. parton dijet M_{inv} for the four η topologies, forward-forward, forward-central, central-central, and forward-backward from the 2012 pp 510 GeV data [93]

transverse spin-dependent azimuthal asymmetries in the distribution of hadrons within jets, the so-called "Collins" asymmetries [100, 101]. Recent phenomenological studies suggest these results are consistent with those observed in SIDIS [102, 103]. If confirmed, this would indicate the Collins effect is universal and that transverse-momentum-dependent factorization in pp is robust for observables such as hadrons-within-jets.

Update on 2017 Data Analysis

One of the highlighted analyses from the STAR 2017 pp 510 GeV run is a measurement of the Z boson differential cross-section and its transverse single spin asymmetry A_N. The Z boson differential cross-section can be included in an global analysis to constrain the quark transverse momentum distribution (TMD) in the proton, the STAR data will especially constrain the TMDs at high x. The Z boson A_N is the cleanest observable to test the

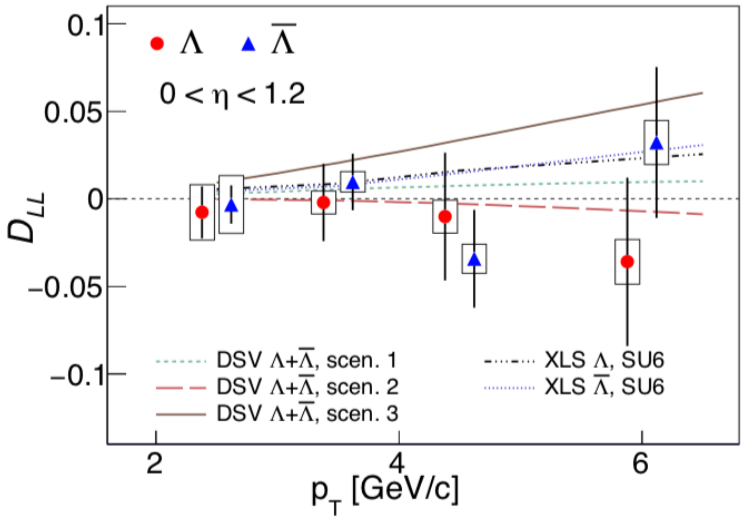

Figure 29: Comparison of the measured spin transfer D_{LL} with theory predictions [96] for positive η versus p_{T} [89]. The vertical bars and boxes indicate the sizes of the statistical and systematic uncertainties, respectively. The $\overline{\Lambda}$ results have been offset to slightly larger p_{T} values for clarity.

predicted non-universality of the Sivers function measures in deep inelastic scattering (DIS) and pp and TMD evolution effects, which are predicted to be large.

With the sample size comparable to the previous 2011, 2012 and 2013 data combined, the 2017 Z boson differential cross-section $d\sigma/dp_{\mathrm{T}}$ as a function of p_{T} has been extracted, and full acceptance and efficiency corrections applied. The full systematic uncertainties for the 2017 results have been finished except for that due to the ongoing determination of the STAR 2017 barrel electro-magnetic calorimeter (BEMC) gain calibration. The currently measured Z boson A_N shows a hint of being away from zero in the positive direction, which favors the sign-change in the Sivers functions and small evolution effects. However this analysis also requires the same BEMC gain calibration and its uncertainty mentioned in the above differential cross-section measurements.

1.3 Run 18 Analysis Update

In this section, we briefly summarize the status of the production and analysis of the Isobar (^{96}Ru + ^{96}Ru and ^{96}Zr + ^{96}Zr) data collected in Run-18. The scientific goal that drove collection of this data was to clarify the interpretation of measurements related to the chiral magnetic effect. Comparison of charge separation results will aid in determining the fraction of those measurements which are related to the chiral magnetic effect by isolating the magnetic field dependence.

Upon the PAC recommendation STAR elected to perform blinded analyses on this dataset. This is the first known attempt of analysis blinding in the Heavy-Ion experimental community. We have implemented a detailed plan for how to ensure that we have successfully blinded all information that might reveal which isobar collision each event is the result of. Several changes to the original blinding procedure have ensued during this validation process, highlighting the appropriateness of the plan. All the identified key analyzers have been engaged in providing rapid feedback during this unique yet critical phase of the production process. To ensure transparency STAR plans to submit for publication a detailed

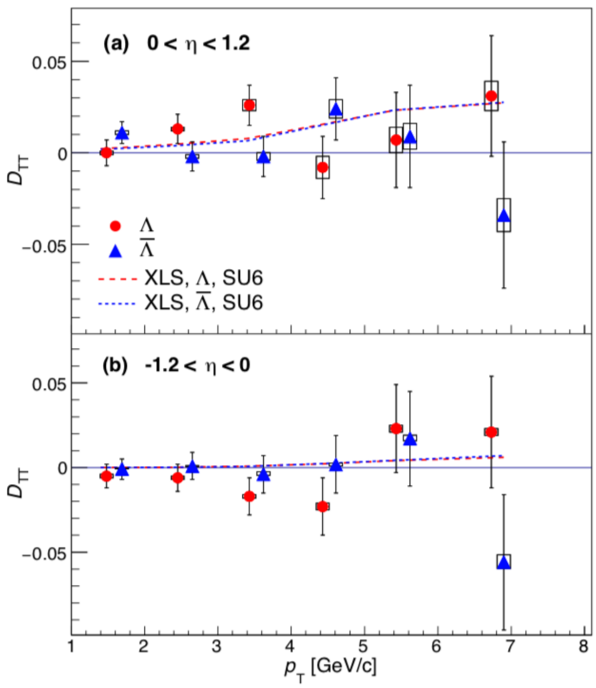

Figure 30: The spin transfer D_{TT} for Λ and $\overline{\Lambda}$ versus p_{T} in comparison with model predictions for (a) positive η and (b) negative η [88]. The vertical bars and hollow rectangles indicate the sizes of the statistical and systematic uncertainties, respectively. The $\overline{\Lambda}$ results have been offset to slightly larger p_{T} values for clarity.

description of the final blinding process prior to publication of the results.

2 Proposed Program

2.1 Continuation of Beam Energy Scan Phase 2

RHIC has already begun the BES-II physics program. Specific details of the physics goals and required statistics for each goal at each collider energy are given below in Table 7. Because in the RHIC collider mode, the lowest collision energy available is $\sqrt{s_{NN}} = 7.7$ GeV, the BES-II collider program has been expanded to include a fixed target program. The beam energies used in the fixed-target part of the program have already been developed for BES-I or will be used in the BES-II collider program. Details of the fixed-target physics statistics requirements for each physics goal at each energy are shown in Table 8, which also includes the single-beam total energy, the center-of-mass rapidity, as this gives insight into the acceptance of STAR for a given energy, and the expected chemical potential, which indicates the region of the QCD phase diagram to be studied.

Table 7: Event statistics (in millions) needed in the collider part of the BES-II program for various observables. This table updates estimates originally documented in STAR Note 598.

Collision Energy (GeV)	7.7	9.1	11.5	14.5	19.6
μ_{B} (MeV) in 0-5% central collisions	420	370	315	260	205
Observables					
R_{CP} up to $p_{\mathrm{T}} = 5$ GeV/c	-	-	160	125	92
Elliptic Flow (ϕ mesons)	80	120	160	160	320
Chiral Magnetic Effect	50	50	50	50	50
Directed Flow (protons)	20	30	35	45	50
Azimuthal Femtoscopy (protons)	35	40	50	65	80
Net-Proton Kurtosis	70	85	100	170	340
Dileptons	100	160	230	300	400
$>5\sigma$ Magnetic Field Significance	50	80	110	150	200
Required Number of Events	100	160	230	300	400

As noted, the BES-II program has already started and the achieved performance in the energies completed or in progress can be used to refine the estimates of performance in the upcoming two years. For the collider program, we review the performance for the 27 GeV run from 2018, the 19.6 GeV run completed in 2019, and the data currently being taken at 14.6 GeV[1]. For the fixed-target part of the program we will review the performance for the 3.0 GeV run and the 7.2 GeV test run, both of which occurred in 2018, and a brief test at 3.9 GeV which took place this year.

For the collider system at 27 GeV, we expected a luminosity increase of a factor of 3.3. Based on the good event rate of 190 Hz achieved in the 2014 run we hence inferred a data

[1] In 2014, collisions were run at a collider energy of 14.546 GeV, which was rounded to 14.5 GeV. This year, we are running at a slightly different energy, 14.618 GeV, which is rounded to 14.6 GeV.

Table 8: Event statistics (in millions) needed in the fixed-target part of the BES-II program for various observables.

$\sqrt{s_{NN}}$ (GeV)	3.0	3.2	3.5	3.9	4.5	5.2	6.2	7.7
Single Beam Energy (GeV)	3.85	4.55	5.75	7.3	9.8	13.5	19.5	31.2
$\mu_{\rm B}$ (MeV)	721	699	666	633	589	541	487	420
Rapidity y_{CM}	1.06	1.13	1.25	1.37	1.52	1.68	1.87	2.10
Observables								
Elliptic Flow (kaons)	300	150	80	40	20	40	60	80
Chiral Magnetic Effect	70	60	50	50	50	70	80	100
Directed Flow (protons)	20	30	35	45	50	60	70	90
Femtoscopy (tilt angle)	60	50	40	50	65	70	80	100
Net-Proton Kurtosis	36	50	75	125	200	400	950	NA
Multi-strange baryons	300	100	60	40	25	30	50	100
Hypertritons	200	100	80	50	50	60	70	100
Requested Number of Events	300	100	100	100	100	100	100	100

taking rate of 627 Hz. The rate of good events achieved for the 2018 run was 620 Hz, consistent with these expectations. Although in the 2018 isobars run STAR achieved an average of 15 hours per day of data taking, the average for the 27 GeV run was only 9 hours because beam time was shared with Coherent electron Cooling (CeC) development.

For the 19.6 GeV collider system, we had two ways to project the expected performance. First, we could extrapolate the performance from the 19.6 GeV run in 2011. In that run, STAR achieved a good event rate of 100 Hz; the expected increase in luminosity was a factor of 3.3, which suggested we should expect a good event rate of 330 Hz. Second, we could scale the performance of the 27 GeV run from 2018; the performance of RHIC typically scales as γ^2 for accelerated beams; scaling the 620 Hz achieved for 27 GeV by $(9.8/13.5)^2$ predicted a good event rate of 335. The actual achieved rate in 2019 was 400 Hz as seen in Fig. 31a, which exceeded expectations. The average data taking time per day for the 19.6 GeV run was 11 hours; this time this was below 15 hours per day due to time share with the development of Low Energy RHIC electron Cooling (LEReC).

For the 14.6 GeV collider run, we could not really scale from the 2014 performance because the achieved event rate of 17 Hz had been unusually low due to the challenge of separating the good events from the background off of the small beam used while the Heavy Flavor Tracker was installed in STAR. RHIC performance typically scales as γ^3 for beams below the nominal injection energy. Scaling the expected performance at 19.6 GeV of 335 Hz by $(7.3/9.8)^3$, we expected a good event rate of 138 HZ. Scaling the achieved performance at 19.6 GeV of 400 Hz, we expected a rate of 160 Hz. The achieved rate has now approached 160 Hz as seen in Fig. 31b. Thus the performance for 14.6 GeV is as expected.

For the projections for the newly proposed 16.7 GeV run, we have scaled the achieved 19.6 GeV performance of 400 Hz by $(8.35/9.8)^3$ to project a good event rate of 245 Hz.

For the 11.5 GeV run, scaling the 19.6 and 14.6 GeV performance would project 80 Hz. C-AD predicts a factor of 2.0 increase over the 2010 performance, which would project a good event rate of 60 Hz. We have included a range of projections for this system in Table 9.

For 7.7 GeV we have again included a range of projections. The pessimistic projection comes from either using a factor of 3.0 improvement over 2010 or scaling from the pessimistic 11.5 GeV projection. The optimistic projection comes from either using a luminosity increase of 4.0 over 2010 or scaling the optimistic projection for 11.5 GeV. Note that the improved luminosity increase of a factor of 4.0 is the assumed performance of the LEReC. Note also that we are only projecting 12 hours per day of data taking due the short fill length.

The 9.1 GeV projections are scaled from the 7.7 GeV projections.

Table 9 shows lines for the optimal fill length, which is determined by the expected lifetimes of the beam, and the expected turn around time between beam dump and injection of a new store. The fill length and turn around time help determine the expected hours per day of data taking. The table also shows the maximum DAQ rates expected. The rates are determined from the expected longitudinal spread of the collision vertex distribution and the expected background rate at each energy. At no collider energies with the trigger rate exceed the DAQ bandwidth of STAR.

Table 9: Achieved and projected experiment performance criteria for the BES-II collider program.

Collision Energy (GeV)	7.7	9.1	11.5	14.5	16.7	19.6	27
Performance in BES-I							
Good Events (M)	4.3	NA	11.7	12.6	NA	36	70
Days running	19	NA	10	21	NA	9	8
Data Hours per day	11	NA	12	10	NA	9	10
Fill Length (min)	10	NA	20	60	NA	30	60
Good Event Rate (Hz)	7	NA	30	17	NA	100	190
Max DAQ Rate (Hz)	80	NA	140	1000	NA	500	1200
Performance in BES-II (**achieved** or projected)							
Required Number of Events	100	160	230	300	250	400	NA
Achieved Number of Events	TBD	TBD	TBD	TBD	TBD	**580**	**560**
fill length (min)	20	30	40	**45**	50	**60**	**120**
Good Event Rate (Hz)	20-33	33-53	60-80	**160**	245	**400**	**620**
Max DAQ rate (Hz)	125	160	250	**800**	1300	**1800**	**2200**
Data Hours per day	12	14	15	**10**	15	**11**	**9**
weeks to reach goals	16-10	14-8.5	10.2-7.6	9.5	2.7	**5.3**	**4.0**

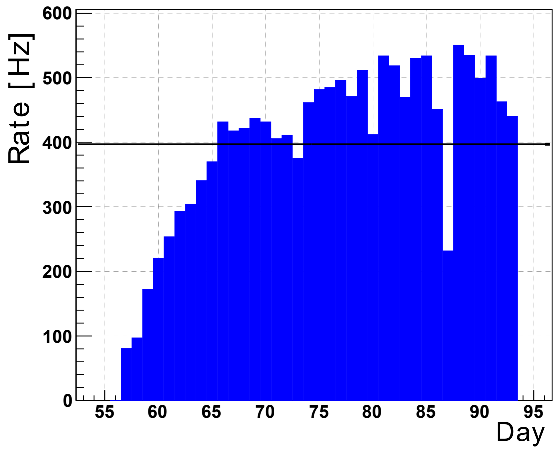

(a) Au+Au 19.6 GeV.

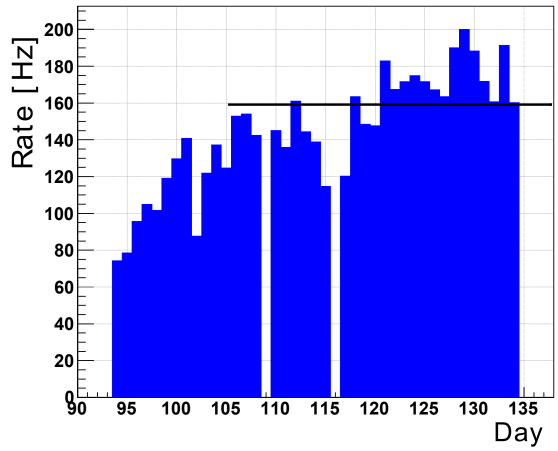

(b) Au+Au 14.6 GeV.

Figure 31: The achieved rate of good events determined with the High Level Trigger (HLT) for Run-19.

For the fixed-target runs and tests performed to date the following performances were achieved: for the $\sqrt{s_{NN}} = 3.0$ GeV (single beam energy of 3.85 GeV) run in 2018, the trigger efficiency was 93% and the good event rate was 5.1×10^6 events/hour for 60 hours and a total of 306M good events, for the 7.2 GeV (28 GeV) test in 2018, the trigger efficiency was 95% and the good event rate was 3.5×10^6 events/hour for 72 hours and a total of 252M good events, for the 3.9 GeV (7.3 GeV) test in 2019, the trigger efficiency was 90% and the good event rate was 4.1×10^6 events/hour for one hour of data taking. For all of these runs setup took on the order of one hour. The 7.2 GeV test had a lower event rate because this test was being run parasitically with the CeC development and the operators were not as focused on keeping the event rate maximized. Based on these demonstrated performances, it is safe to estimate that a rate of 4×10^6 events/hour is realistic for projections for the fixed target program for all energies across the range. This event rate is limited by the STAR DAQ rate and not by limitations of RHIC.

2.1.1 The Case for Running Au+Au Collisions at $\sqrt{s_{\mathrm{NN}}} = 16.7$ GeV

One of the main goals of the RHIC beam energy scan program is the search for the QCD critical point (CP), which is a distinct singular feature of the QCD phase diagram. The experimental confirmation of the existence of CP will become a landmark in exploring the phase structure of hot dense nuclear matter. The characteristic feature of the CP is the divergence of the correlation length and the density fluctuations. These critical phenomena are best probed by measuring event-by-event fluctuations of conserved quantities, such as baryon, electric charge and strangeness number. The effect of CP could show as a non-monotonic energy dependence of the higher moments of fluctuations in close proximity of the critical point during the beam energy scan.

In the years 2010-2014, RHIC finished the first phase of the Beam Energy Scan (BES) and

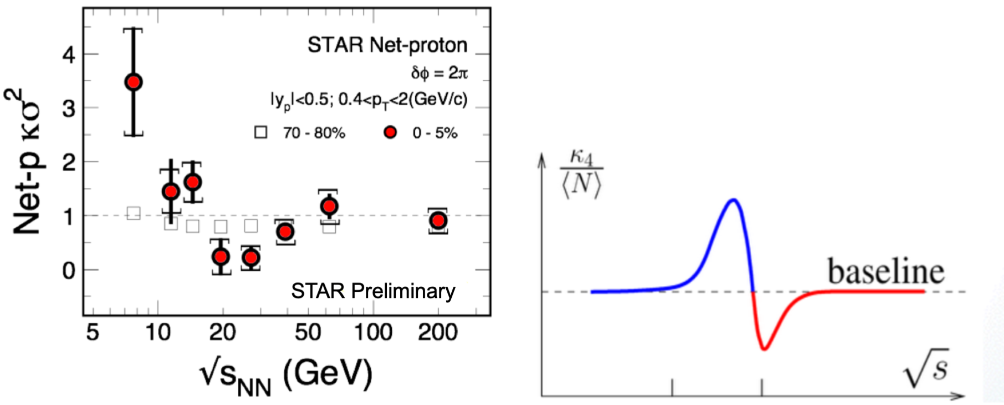

Figure 32: (Left) The fourth order net-proton fluctuations $\kappa\sigma^2$ in most central (0-5%) and peripheral (70-80%) Au+Au collisions as a function of collision energy.(Right) The characteristic signature predicted by the theoretical model for energy dependence of the fourth order fluctuations when the system passes through the critical region [104].

took the data of Au+Au collisions at $\sqrt{s_{\mathrm{NN}}} = 7.7, 11.5, 14.5, 19.6, 27, 39, 62.4$, and 200 GeV. With this experimental data, STAR measured the higher order fluctuations of net-proton, net-charge, and net-kaon multiplicity distributions [106, 107, 108, 109, 110]. One striking observation is the behavior of the fourth-order cumulants, or kurtosis, of the net-proton fluctuation $\kappa\sigma^2$ in most central (0-5%) Au+Au collisions as a function of beam energy. As shown on the left of Fig. 32, the fourth order net-proton fluctuation is close to unity above 39 GeV but deviates significantly below unity at 19.6 and 27 GeV, then becomes above unity at lower energies. This behavior may suggest that the created system skims close by the CP, and receive positive and/or negative contributions from critical fluctuations [104]. It further suggests that, if at energies below 7.7 GeV we see a peak structure for net-proton kurtosis measurement, it could be the signature of CP. However, we ignored the fact that the first order phase transition could also cause a large increase of net-proton kurtosis [111]. Due to entering into the spinodal region (mixed phase), the double peak structure of σ field will cause large values of fourth order cumulants (C_4).

In addition, STAR has measured light nuclei (deuteron and triton) production in Au+Au collisions at RHIC BES energies. The ratio of these yields is predicted to be sensitive to the neutron relative density fluctuations at kinetic freeze-out, which in turn are expected to increase near the critical point and/or a first order phase transition [105]. The neutron density fluctuation is defined as $\Delta n = \langle(\delta n)^2\rangle/\langle n\rangle^2$, which can be approximated from:

$$\Delta n = \frac{1}{g}\frac{N_t \times N_p}{N_d^2} - 1,$$

where N_p, N_d and N_t are the proton, deuteron and triton yields respectively and g is a constant factor of 0.29. In Fig. 33, we use the published feed-down corrected BES-I proton yields [112], recently submitted deuteron data [19], and preliminary triton and 14.5 GeV results to calculate Δn in central Au+Au collisions as a function of collision energy. These neutron density fluctuations exhibit a clear non-monotonic energy dependence with a peak

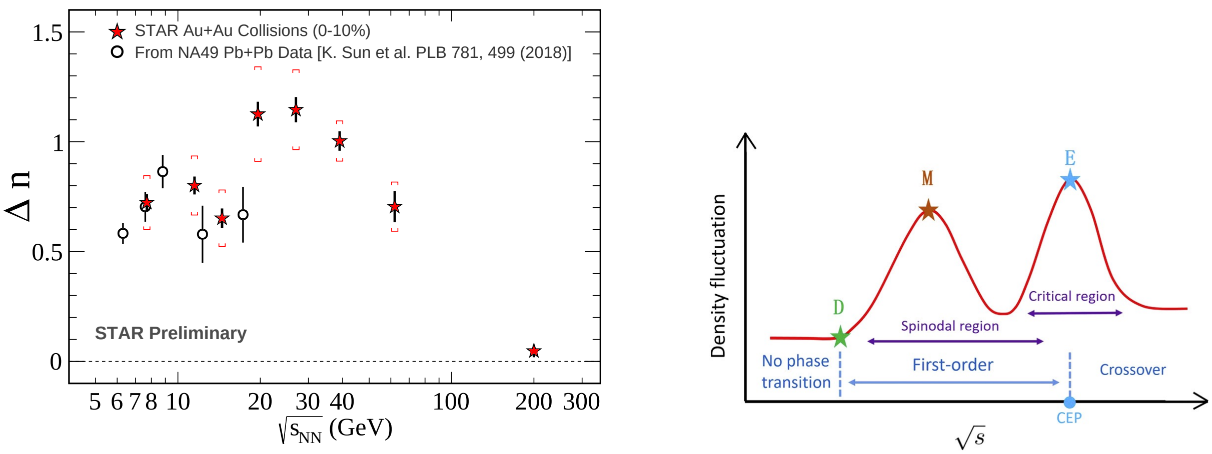

Figure 33: (Left) Collision energy dependence of the neutron density fluctuation in central Au+Au collisions. The open square data based on NA49 results in central Pb+Pb collisions at $\sqrt{s_{\rm NN}}$=6.3 (0-7%), 7.6 (0-7%), 8.8 (0-7%), 12.3 (0-7%), and 17.3 (0-12%) energies. (Right) Illustration of the density fluctuation as a function of collisions energy in the critical region and spinodal region [105].

around 19.6 GeV. Furthermore, the neutron density fluctuation show a sudden drop below 19.6 GeV, where the results are consistent with the results from NA49 experiment. The experimental observations of non-monotonic energy dependence in neutron density fluctuation can suggest the double peak structure, which assumes that the system goes through the critical region and the first order spinodal region.

Thus, in BES-II, we propose to take one more energy point in Au+Au collisions at 16.7 GeV based on the following two observations, presented in Figs. 32 and 33, aiming at QCD critical point search with net-proton kurtosis and neutron density fluctuation:

1. Net-p kurtosis and neutron density fluctuations, which are both sensitive to the critical fluctuation, show dip and peak structures around 19.6 GeV. This may suggests that the system passed through the critical region around 19.6 GeV.

2. We observe sudden changes between 19.6 and 14.5 GeV in the energy dependence of net-p kurtosis and neutron density fluctuation in the BES-I data measured by the STAR experiment. The neutron density fluctuations at low energies below 14.5 GeV are consistent with the results from NA49 experiment [105].

Table 10: Event statistics (in millions) needed in a Au+Au run at $\sqrt{s_{\rm NN}}$ = 16.7 GeV for fourth order net-proton fluctuations ($\kappa\sigma^2$) and neutron density fluctuation (Δn) measurements.

Triggers	Minimum Bias	Net-proton $\kappa\sigma^2$ (0-5% Cent.)	Δn (0-10% Cent.)
Number of events	250 M	6% error level	3.6% error level

These two observations indicate that the critical point maybe close to 19.6 GeV. Since there are sudden changes in different observables between 19.6 and 14.5 GeV, it is important to conduct a finer beam energy scan between these two energies, i.e. 19.6 GeV (μ_B =205 MeV) and 14.5 GeV (μ_B =266 MeV). Therefore, we request a run with Au+Au collisions at $\sqrt{s_{\rm NN}}$=16.7 GeV (chemical freeze-out μ_B =235 MeV), which is just between 19.6 and 14.5 GeV with equal μ_B gap, about 30 MeV, on each side.

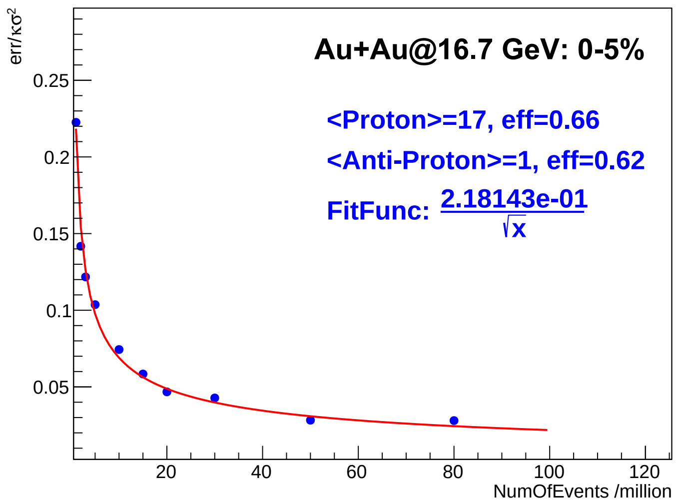

Figure 34: Monte Carlo simulation for the relative statistical errors of net-proton $\kappa\sigma^2$ in 0-5% most central Au+Au collisions at 16.7 GeV. A Skellam distribution for net-proton is assumed; the mean value for protons and anti-protons are 17 and 1, respectively. The average efficiencies for proton and anti-proton are 0.66 and 0.62, respectively.

According to the previous estimation of the required event statistics for BES-II energies presented in Table 7, we need about 250 million minimum-bias events for the net-proton kurtosis measurement at 16.7 GeV. It gives us about 12.5 million events (250/20) in 0-5% most central collisions. This will ensure that the relative statistical errors of net-proton $\kappa\sigma^2$ in 0-5% most central Au+Au collisions will reach the 6% level (shown in Fig. 34). This event statistics will also ensure that the relative statistical errors of neutron density fluctuation reach about 3.6% level in 0-10% central Au+Au collisions. On the other hand, the iTPC will help to measure the lower p_T light nuclei and thus reduce the extrapolation systematic errors of the yield.

If nature put the critical point in the QCD phase diagram between 14.5 and 19.6 GeV, RHIC has the best chance to discover it!

2.2 Spin Physics in pp at $\sqrt{s}$ = 500 GeV

The STAR collaboration is excited by the possibility of a dedicated pp run in FY22 at $\sqrt{s}$ = 500 GeV. This would be the inaugural physics run with the full suite of upgraded forward detectors installed ("fSTAR"), as well as the first *pp* run able to exploit the capabilities of the new EPD, eTOF, and (especially) the iTPC subsystems. The proposed time for this run, following the completion of BES-II, may be the last opportunity for extended 500-GeV running at RHIC. With 16 weeks of running we anticipate a total delivered luminosity of 1.2 fb^{-1}.

Physics Motivation and Goals

Over the last decade, we have made enormous strides in our understanding of the structure of the nucleon, and how the quarks and gluons of QCD give rise to its observed properties. We now have compelling evidence that *gluons contribute significantly to the proton's spin*, at a level comparable to that of the quarks. We have gained new insights into the *nature and origin of the quark-antiquark 'sea,'* through studies of $W^{\pm}$ production in *pp* collisions. Clear signatures of *transverse polarization effects*, sensitive to the relative alignment of partonic spin or intrinsic k_T with the spin of a transversely polarized proton, have been revealed via studies of di-hadron and hadron-in-jet asymmetries.

Despite these achievements, deep and critical questions remain unanswered. We have only limited understanding of how the quarks, gluons, and their spins are distributed in space and momentum inside the nucleon, or how partonic orbital motion might contribute to the proton spin. Large transverse spin asymmetries observed at forward angles for inclusive hadron production remain poorly understood. Assumptions of universality and factorization for transverse-momentum-dependent (TMD) functions probed in *pp* collisions need to be tested, and their evolution in Q^2 quantified.

When BES-II is completed in 2021, STAR will be very well positioned with an excellent suite of detectors to address many of these questions – but over a limited range in x, the fraction of the proton momentum carried by the parton of interest. To advance our understanding of how known properties of hadrons and hadronic matter emerge from QCD, it is essential that one probes both the higher-x or valence region, and low values of x, where gluons and sea quarks are abundant. These kinematic regions are accessed most directly in highly asymmetric partonic collisions, *i.e.*, when the x of one colliding quark or gluon greatly exceeds that of the other, $x_1 \gg x_2$. For such events, the outgoing particles are emitted–and thus must be detected–at far forward angles, a capability provided by the proposed STAR Forward Upgrade. A 500 GeV *pp* run in FY22 would thus allow STAR to shed insight on many of these crucial questions via several flagship measurements, exploiting the increased statistical power and kinematic reach made possible by recent and planned detector upgrades.

With transverse spin orientation, STAR would prioritize measurements of the Collins and Interference Fragmentation Function (IFF) transverse spin asymmetry A_{UT}. As outlined below, these measurements may shed light on a longstanding issue in hadronic physics: the surprisingly large transverse single-spin asymmetries (SSA) for inclusive hadron production, first seen in *pp* collisions at fixed-target energies, that remain large at the highest RHIC energies and large p_{T}. Figure 35 summarizes the world data as a function of Feynman-x. The asymmetries are seen to be nearly independent of $\sqrt{s}$ over a range of roughly 5-500 GeV.

This is particularly striking because, while the pion cross sections are consistent with NLO pQCD expectations at RHIC energies [113], they are up to an order of magnitude larger than NLO pQCD calculations at low $\sqrt{s}$ [114].

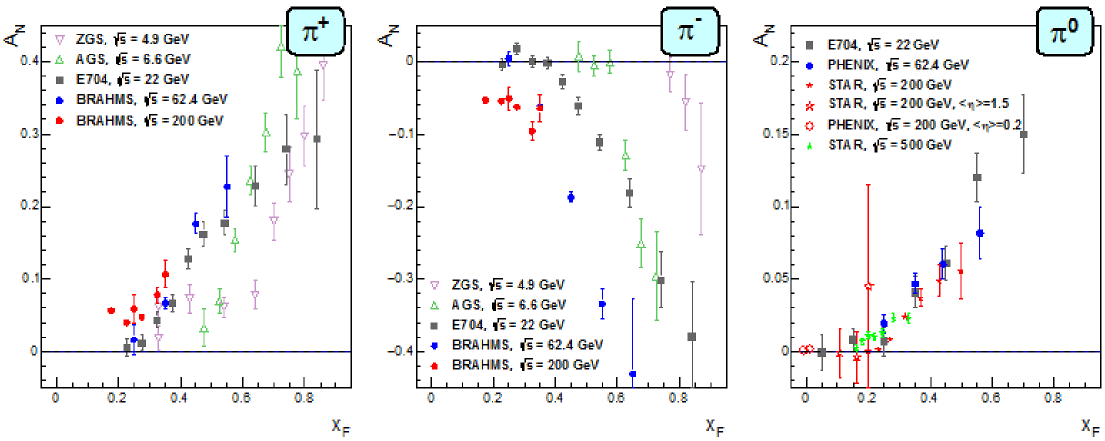

Figure 35: Transverse single-spin asymmetries for charged and neutral pions at different center-of-mass energies, shown as a function of Feynman-x.

To understand the observed SSAs one has to go beyond the conventional leading-twist collinear parton picture in the hard processes. Two theoretical formalisms have been proposed to explain the sizable SSAs in the QCD framework: Transverse momentum-dependent (TMD) parton distribution and fragmentation functions, such as Sivers and Collins functions; and transverse-momentum integrated (collinear) quark-gluon-quark correlations, which are twist-3 distributions in the initial state proton or in the fragmentation process. The Sivers function and its twist-3 analog, the Efremov-Teryaev-Qui-Sterman (ETQS) function ([115] and references therein), quantify the probability for a quark or gluon to preferentially carry transverse momentum left or right in a proton that has spin up. Such a preference can arise, for example, from spin-orbit correlations. The Collins effect involves convolution of quark transversity with the Collins fragmentation function; the former characterizes the transverse polarization of a quark in a transversely polarized proton, while the latter describes an azimuthal modulation of pions about the jet direction when a transversely polarized quark fragments.

Transversity is a leading twist distribution in the proton: together with the unpolarized and helicity distributions, it is a fundamental proton property. Both the Collins and IFF asymmetries are sensitive to the transversity distribution [116, 117, 118], $\delta q(x)$, which can be interpreted as the net transverse polarization of quarks within a transversely polarized proton. Differences between the helicity distributions and the transversity distributions for quarks and antiquarks provide a direct, x-dependent connection to non-zero orbital angular momentum components in the wave function of the proton [119]. Recently, the measurement of transversity has received renewed interest as a way to access experimentally the tensor charge of the nucleon, defined as the integral over the valence quark transversity, $\delta q^a = \int_0^1 (\delta q^a(x) - \delta \bar{q}^a(x))\, dx$ [120]. Measuring the tensor charge is important: it can be calculated on the lattice with comparatively high precision, due to the valence nature of transversity, and thus is one of the few quantities for which experimental results on nucleon spin structure can be compared to *ab initio* QCD calculations. Moreover, the tensor charge characterizes the sensitivity of observables in low energy hadronic reactions to Beyond the Standard Model (BSM) physics processes that include tensor couplings to hadrons, such as experiments with ultra-cold neutrons and nuclei.

Transversity is difficult to access due to its chiral-odd nature, requiring the coupling of this distribution to another chiral-odd distribution. Semi-inclusive deep inelastic scattering (SIDIS) experiments have successfully probed transversity through two channels: asymmetric distributions of single pions, coupling transversity to the (TMD) Collins fragmentation function [121]; and azimuthally asymmetric distributions of di-hadrons, coupling transversity to IFFs [122] in the framework of collinear factorization. Taking advantage of universality and robust proofs of TMD factorization for SIDIS, recent results (see, for example, [123, 124]) have been combined with e^+e^- measurements [125, 126], yielding the first global analyses that extract simultaneously the transversity distribution and polarized FF. Yet in spite of these large data sets, the kinematic reach of existing SIDIS experiments, for which Bjorken-x values do not exceed $x \sim 0.3$, limits the current extractions of transversity.

STAR was the first experiment to demonstrate that significant mid-rapidity Collins [101] and IFF asymmetries [99] are also observed in pp collisions. Note that the Collins measurement requires reconstruction of the angular distribution of charged pions around the axis of a jet, while the IFF requires reconstruction of di-hadron pairs. Thus, both rely on good charged-particle identification and tracking, and hence all STAR measurements to date have been restricted to the current TPC acceptance, $|\eta| < 1$. In order to further advance our understanding of transverse momentum-dependent effects, it is critical to extend our kinematical reach to lower and higher x. The iTPC and fSTAR upgrades will access jets at rapidities where more asymmetric collisions allow larger x and larger quark contributions in the hard process, or to probe lower x values and tag on gluon contributions in the hard scattering. More specifically, a run at $\sqrt{s} = 500$ GeV, with η coverage between 2.5 and 4, would allow STAR to access x above 0.3 for reasonably high scales, as well as quantitatively test universality in the range below, overlapping the range of current SIDIS experiments. On the other end of the partonic momentum spectrum, which is important for the study of linearly polarized gluons (see below), x values below 2×10^{-3} can be reached.

To estimate the physics impact of a possible run at $\sqrt{s} = 500$ GeV, we have done careful simulations of the uncertainties one might expect for some of the transverse asymmetries discussed above. A realistic momentum smearing of final state hadrons, as well as jets, in this rapidity range was assumed, and dilutions due to beam remnants (which become substantial at high rapidities) and underlying event contributions have been taken into account. As currently envisioned, no dedicated particle identification at forward rapidities is feasible for these measurements, so only charged hadrons were taken into account, reducing the expected asymmetries due to dilution by a moderate amount of protons (10-14%) and kaons (12-13%). As antiprotons are suppressed compared to protons in the beam remnants, the negative hadrons in particular can be considered a good proxy for negative pions (78%

purity according to PYTHIA-6). Given their sensitivity to the down quark transversity via favored fragmentation, they are of particular importance because SIDIS measurements are naturally dominated by up-quarks due to their electromagnetic interaction. We have estimated our statistical uncertainties based on a delivered luminosity of 385 pb^{-1}, which leaves uncertainties nearly invisible after smearing. The uncertainties were evaluated in a very fine binning in jet transverse momentum, jet rapidity and the fractional energy z of the hadrons relative to the p_{T} of the jet. These expected uncertainties are compared in Fig. 36 to the asymmetries obtained from the transversity estimates described in the caption.

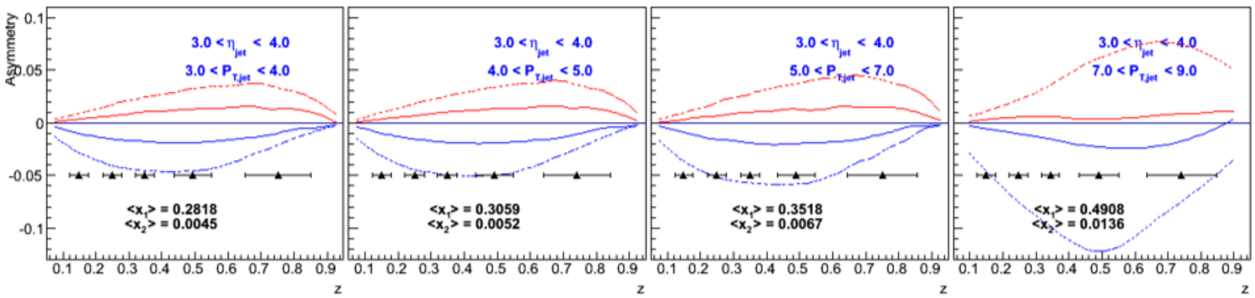

Figure 36: Expected h^- Collins asymmetry uncertainties (black points) from a delivered luminosity of 385 pb^{-1}, compared to positive (red) and negative (blue) pion asymmetries based on the Torino extraction [127] (full lines) and the Soffer bound [128] (dashed lines) as a function of fractional energy z for various bins in jet rapidity and transverse momentum.

We also note that although the studies presented here are for the Collins asymmetries, the resulting statistical uncertainties will be similar for other measurements using azimuthal correlations of hadrons in jets. One important example is the measurement of "Collins-like" asymmetries to access the distribution of linearly polarized gluons. While gluons cannot possess transverse spin, there is a strong analogy between quark transversity and the linear polarization of gluons. Similarly, there exists an equivalent of the Collins function for the fragmentation of linearly polarized gluons into unpolarized hadrons [129], first investigated by STAR at mid-rapidity in data collected in 2011 [101]. The linear polarization of gluons is a largely unexplored phenomenon, but it has been a focus of recent theoretical work, in particular due to the relevance of linearly polarized gluons in unpolarized hadrons for the p_{T} spectrum of the Higgs boson measured at the LHC. Polarized proton collisions at 500 GeV provide ideal kinematics to study the linearly polarized gluon distribution in polarized protons, especially in highly asymmetric parton scattering events in which jets are detected in the backward (relative to the polarized beam) direction.

Finally, we note that over a 16-week run we expect a delivered luminosity close to 1.2 fb^{-1}. This is roughly double that from Run-17 and also roughly double that shown in Fig. 36.

Physics Goals: Longitudinal Running

It is not necessary to describe here the fundamental importance of determining the gluon helicity distribution $\delta g(x)$ for the proton, or to point out the essential contributions made by

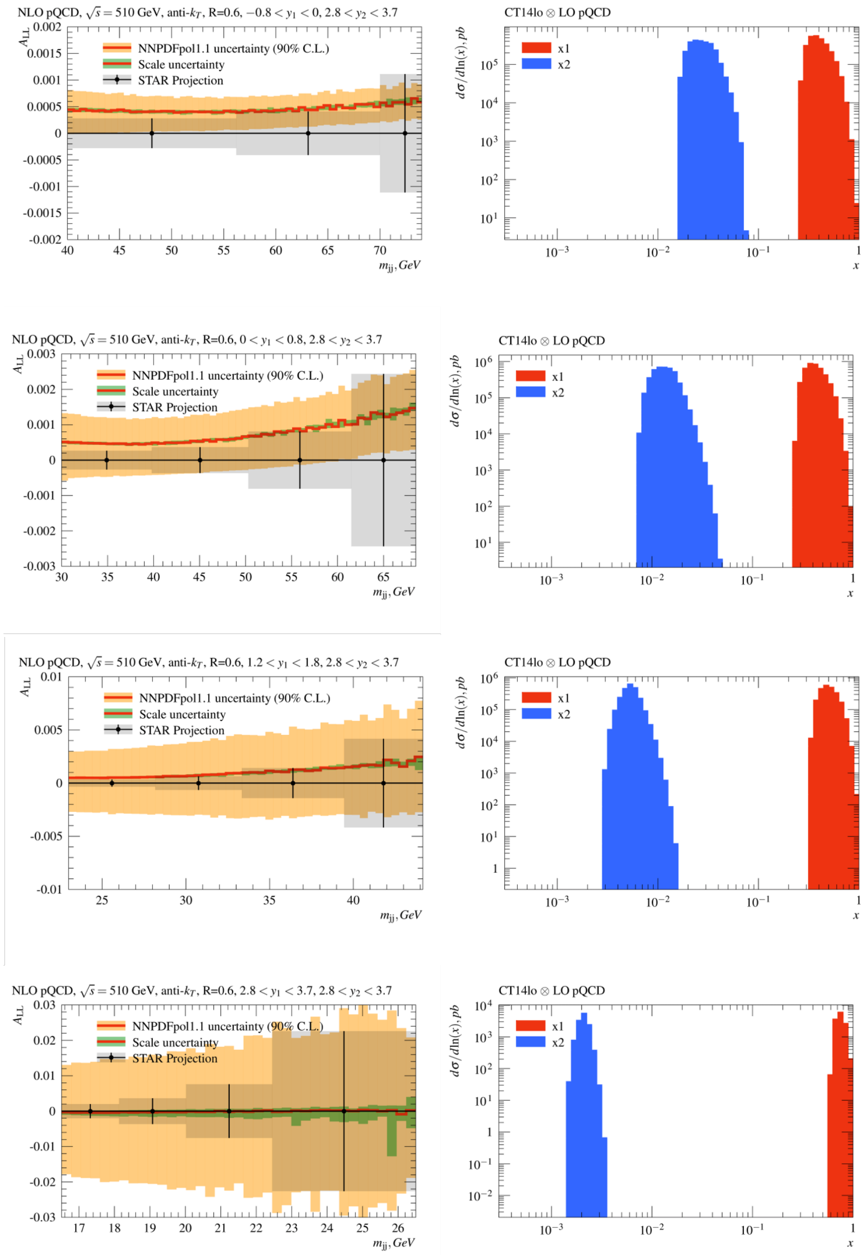

Figure 37: (Left) NLO calculations of the longitudinal double-spin asymmetry A_{LL} as a function of $M_{\text{inv}}/\sqrt{s}$ for $2.8 < \eta < 3.7$, together with projected statistical and systematic uncertainties. An uncertainty of 5×10^{-4} has been assumed for the systematic uncertainty due to relative luminosity. A beam polarization of 60% and a total delivered luminosity of 1 fb^{-1} have been assumed, with a ratio of recorded to delivered luminosity of 2/3. (Right) Ranges of momentum fraction x_1 and x_2 accessed at $\sqrt{s} = 500$ GeV for the forward acceptance region $\eta = 2.8$-3.7.

the RHIC STAR and PHENIX experiments towards this goal. The present status of STAR's efforts has been presented in the Cold QCD and Spin Highlights section of this document.

We note, though, that the study of longitudinally polarized pp collisions at the highest RHIC energies ($\sqrt{s}$ = 500 GeV), coupled with detection of outgoing high-p_T particles or jets at the most forward rapidities ($\eta \sim 4.2$) allows one to probe the lowest x regions that are accessible at RHIC. A future 500 GeV pp run, with an integrated luminosity of 1.2 fb^{-1}, would reduce the statistical uncertainty of current STAR inclusive jet results *at mid-rapidity*. These data are sensitive to gluons in the range $0.01 < x < 1$; and while they suggest a positive $\delta g(x)$ for moderate x, they do little to constrain the functional form of the distribution at low x. This translates into a large uncertainty in δG, the gluonic spin contribution to the proton spin. Dijet experiments provide a more direct measure of the x values of the colliding partons; when extended to the 'fSTAR' region, we will be able to access x down to a few times 10^{-3}, with precision far beyond current uncertainties.

The left-side plot in Fig. 37 shows the projected precision attainable for the asymmetry A_{LL} as a function of the scaled invariant dijet mass $M_{\text{inv}}/\sqrt{s}$ for four topological dijet configurations, requiring one jet detected in the proposed forward calorimeter system in combination with a second jet in the range $-0.8 < \eta < 0.0$, $0.0 < \eta < 0.8$, $1.2 < \eta < 1.8$, or also in the FCS ($2.8 < \eta < 3.7$). It is clear from the right side of the figure that the two most forward configurations would allow one to probe x values as low as a few times 10^{-3}. The systematic uncertainty, which is assumed to be driven by the relative luminosity uncertainty of $\sim 5 \times 10^{-4}$, is seen to dominate the statistical uncertainties, so any future measurements in these topological configurations would also require improved relative luminosity determinations.

2.3 The Case for a Small System Run: O+O at $\sqrt{s_{\text{NN}}}$ =200 GeV

Collective long-range azimuthal correlations in A+A collisions have been successfully described as a hydrodynamic response by a fluid-like system to geometric shape fluctuations in the initial state [43]. However, such an interpretation of similar collective phenomena observed in small-system collisions, such as pp and p+A, has been challenged. The small size and short lifetime might prevent the system from quickly thermalizing and evolving hydrodynamically. Instead, collectivity arising either from initial momentum correlations motivated by gluon saturation models [130] or via a few scatterings among partons (without hydrodynamization) [131, 132, 133] has been proposed as alternative source of collectivity that may be dominant in small systems. Lots of experimental and theoretical efforts have been devoted to the study of collectivity in small-system collisions, with the goal of understanding the time-scale for the emergence of collectivity and the mechanism for early-time hydrodynamization in large collision systems.

One key feature that distinguishes initial momentum correlation models (ISM) from final-state interaction models (FSM, including hydrodynamics or a few scatterings) is the connection to the initial-state geometry [134]. In FSM, the collectivity is a geometrical response to initial shape fluctuations, i.e., v_n is approximately proportional to the n^{th}-order initial-state eccentricity ε_n. In ISM, such a geometrical response is expected to be absent [135]. One idea to distinguish between these two scenarios is to perform a geometry scan by colliding systems with different spatial eccentricities and see if the measured v_n is correlated with the change of ε_n between different systems [136].

Such a small system scan program has been recently carried out at RHIC for a few very small systems including p+Au, d+Au and ^{3}He+Au, where studies of elliptic flow (v_2) and triangular flow (v_3) have been performed [35, 137, 138]. In high-multiplicity events, ε_2 was expected to be larger in d+Au and ^{3}He+Au than in p+Au, while ε_3 is comparable between p+Au and d+Au [136], and both are smaller than in ^{3}He+Au. Therefore, a similar hierarchy is expected for v_2 and v_3 in FSM, as observed experimentally [137]. However, ISM based on a particular implementation of gluon saturation physics could produce large momentum anisotropy in these systems [135], and may produce a hierarchy among different small systems [139]. The situation is more challenging in the understanding of collectivity involving heavy quarks in small systems, such as D meson or J/Ψ in p+Pb collisions [140, 141, 142]: FSM presently significantly underestimates the v_2 for D and J/Ψ [143], while an ISM-based approach is able to describe the data [144] The relative importance of FSM vs. ISM for the v_n data in small systems is an area of intense ongoing debate [145]. Even in FSM, there are also large uncertainties in modeling the initial-state geometry, largely due to different treatments of subnucleonic fluctuations, which are poorly known and expected to play an important role, especially in small asymmetric systems. Moreover, experimental studies from previous $p/d/^3$He+Au scans at RHIC were limited by detector capabilities: 1) most measurements were based on two-particle correlations with limited understanding of non-flow systematics, 2) the nature of longitudinal decorrelations of collectivity and its effects on the measurements were poorly understood, 3) a large class of multi-particle observables, demonstrated to be very insightful at the LHC [146], were not explored.

So far, both RHIC and the LHC carried out collisions for either relatively large (Pb+Pb, Au+Au, Xe+Xe, Cu+Cu, ...) or very small (pp, p+Pb, p+Au, d+Au, and ^{3}He+Au) systems. The large gap between pp and Cu+Cu is one of the last unexplored frontiers[2] and we propose that RHIC should play a unique role to fill-in and address a number of key open questions, largely related to collectivity in small systems, as outlined below:

- How much do initial-state correlations vs. geometry-driven final-state interactions contribute to the observed collectivity? Can we unambiguously establish experimental evidence of initial-state correlations?

- For final-state scenarios, to what extent does the collectivity arise from a hydrodynamic fluid-like QGP, as opposed to an off-equilibrium system with only a few scatterings per parton?

- What is the role of subnucleonic fluctuations in determining the initial-state geometry?

- Can we observe jet quenching in small systems?

[2]RHIC has no limitation on small A+A systems, based on private communication with Wolfram Fischer

A new comprehensive scan of colliding ion species at RHIC by systematically varying the system size and geometry, particularly for those between pp and Cu+Cu collisions, will provide a unique lever-arm to vary contributions from different mechanisms and impose strong constraints on both ISM and FSM. Since the last RHIC $p/d/$He+Au scan, the STAR experiment has completed several detector upgrades that extend p_{T} and particle identification to $|\eta| < 1.5$, and provide centrality and event plane determination in $2 < |\eta| < 5$ [147, 148, 149]. An ongoing forward upgrade to instrument the $2.5 < \eta < 4$ region with tracking detectors and calorimeters is expected to be completed in 2021 [2]. The extended detector capability should allow a full exploration of collectivity using all the observables and methods developed for large systems at RHIC/LHC. We will have much better control of the non-flow systematics, leading to a better understanding of the multi-particle nature of the collectivity and the longitudinal correlations to constrain the full 3D initial conditions.

As an example, model studies of v_2 and v_3 in various small systems including symmetric (C+C, O+O, Al+Al, Ar+Ar) and asymmetric (p+Au, d+Au, ^{4}He+Au) collisions using AMPT are shown in Fig. 38. AMPT belongs to the category of final-state interaction models, where v_n is largely driven by the geometry of initial nucleon distributions. The v_2 values from asymmetric systems follow different trends: the v_2 in $d/^4$He+Au increases with N_{ch}, while it is relatively constant in p+Au. The v_3 values show a similar N_{ch} dependence as symmetric systems, except for d+Au which deviates from the common trend at large N_{ch}. This study demonstrates that, in a scenario driven by final-state interactions, a clear difference is expected between $d/^4$He+Au and A+A for v_2, while a relatively similar behavior should be observed for v_3. Contributions from other sources, especially ISM, are expected to follow a different behavior; as the system size increases, the ISM contribution will gradually become subdominant. Also, the ISM contribution mainly depends on N_{ch}, with no sensitivity to the initial geometry.

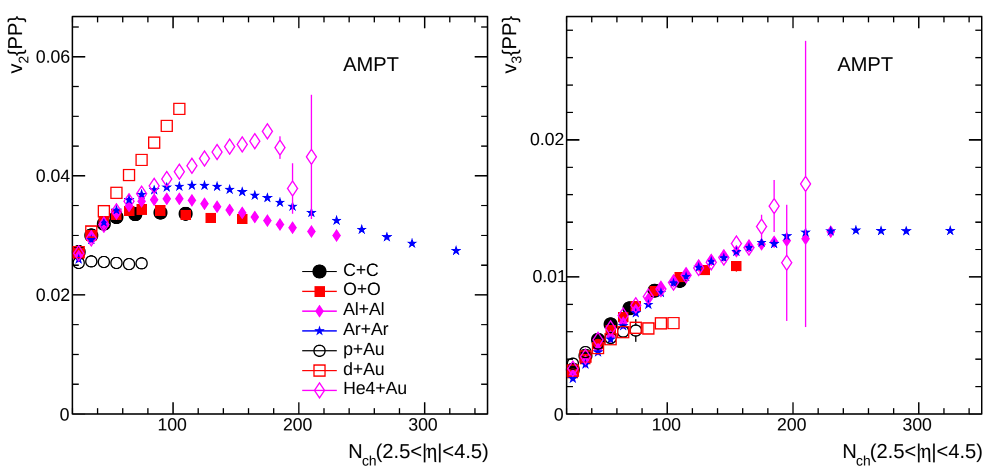

Figure 38: (Left) AMPT predictions for v_2 and (Right) v_3 as a function of N_{ch} in four symmetric and three asymmetric small collision systems.

We propose to embark on a new system-size scan, starting with an O+O run at $\sqrt{s_{\mathrm{NN}}} =$

200 GeV opportunistically in 2020 or towards the end of the BES-II in 2021, to be followed up with a comprehensive scan of symmetric and asymmetric small collision systems using the STAR forward upgrade after 2021, possibly in collaboration with sPHENIX.

In this BUR, we focus on the case for an O+O run. We argue that the O+O run should happen as soon as possible for the following reasons: 1) With the enhanced acceptance from the recently installed iTPC/eTof/EPD, we can already perform significantly more detailed measurements than were possible previously, 2) O+O is only the first part of the small system program with its own unique physics, and this dataset will allow us to motivate and strengthen the case for future small system running, and 3) a strong synergy with the higher-energy O+O run proposed at the LHC around 2021-2022, more details are discuss below.

The recent yellow report on the future LHC heavy-ion physics program discusses the possibility for smaller A+A collisions [146]. This includes a possible O+O run at $\sqrt{s_{\rm NN}}$=2.76–7 TeV in 2022[3], and other light-ion species such as Ar+Ar beyond 2028. The advantage of the O+O system is that it allows a better control of $N_{\rm part}$, ε_n and the hard-scattering rate via number of nucleon-nucleon collisions, $N_{\rm coll}$, for a smaller system, compared to peripheral Pb+Pb collisions [146]. An O+O run at RHIC right after the BES-II would provide an unprecedented and timely comparison of the same small system at very different collision energies (0.2 TeV vs. 2.76–7 TeV). This "RHIC-LHC energy scan" provides a unique opportunity to study systems with nearly identical initial nucleon geometry but very different subnucleon fluctuations and particle production mechanisms with different saturation scales, and mini-jet production in the initial state. The large lever-arm in collision energy should provide new insights on the onset behavior of collectivity, jet quenching, or any other final-state effects in small systems: any model has to describe results at both energies, which naturally leads to a better understanding of results at each energy.

To present a data-driven motivation, Fig. 39 compares the $v_n(p_{\rm T})$ data for $n=2$ and 3 at two energies in a large A+A system and in a p+A system. It is well-known that $v_n(p_{\rm T})$ for charged hadrons in large systems has very little $\sqrt{s_{\rm NN}}$ dependence from RHIC to LHC [150], as well as from 39 to 200 GeV at RHIC [151, 152]. This is confirmed by the left panel which compares Pb+Pb [153] with Au+Au data [154] at 30–40% centrality. However, a comparison of $v_n(p_{\rm T})$ between p+Pb [155] and p+Au [137] central data suggests a very different story. The $v_2(p_{\rm T})$ values are more or less in agreement, but the v_3 at RHIC is lower by more than a factor of two and the relative difference shows no apparent $p_{\rm T}$ dependence. In the FSM picture implies that the initial eccentricities, or the effect of viscosity damping, are very different between the two collision energies. In the ISM picture it may be the result of an energy dependence of initial momentum anisotropy. It would be exciting to see whether the strikingly different $\sqrt{s_{\rm NN}}$ dependence for v_2 and v_3 in p+A collisions also persists in small A+A systems such as O+O collisions between RHIC and LHC.

Figure 40 shows the AMPT model prediction of v_2 and v_3 as a function of $N_{\rm ch}$ in O+O collisions at $\sqrt{s_{\rm NN}}$=0.2 and 2.76 TeV. The results for 2.76 TeV span about a factor of 2.5 larger $N_{\rm ch}$ range than those for 0.2 TeV, due to the larger multiplicity at a higher collision

[3]The possibility of a run in Fall 2021 is also being discussed.

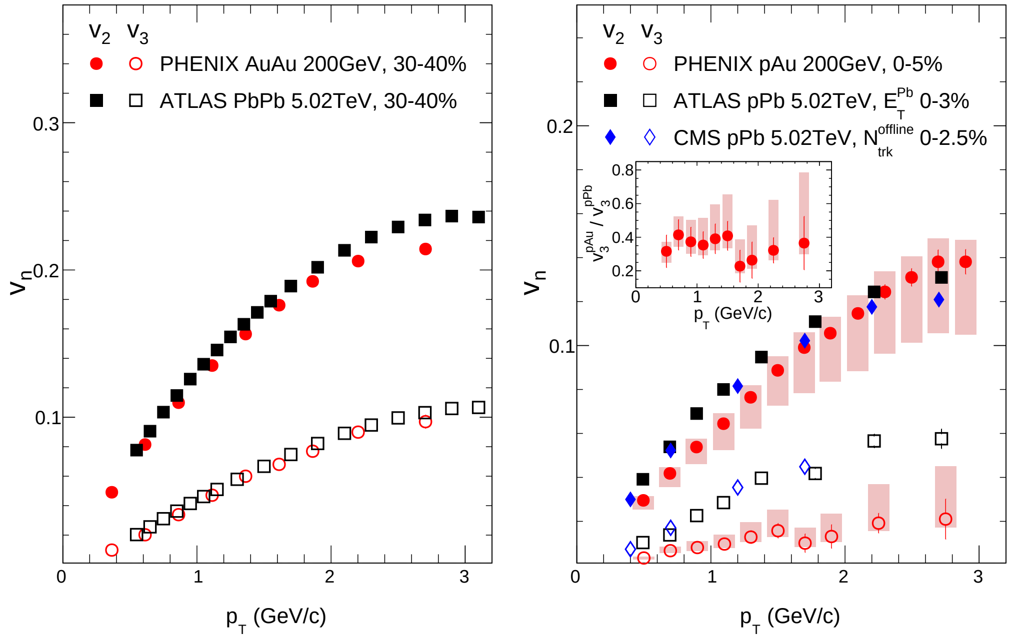

Figure 39: (Left) Comparison of measured v_2 and v_3 from Pb+Pb and Au+Au 30–40% centrality events and (Right) between high-multiplicity p+Pb and p+Au. The inset panel shows the ratio of v_3 between p+Au and p+Pb.

energy. Interestingly, the shape of the $N_{\rm ch}$ dependence of v_2 and v_3 is found to be very different between the two different energies. This may indicate a stronger energy dependence of collectivity for smaller systems.

We propose a one-week O+O program opportunistically in 2020 or right after BES-II in 2021. Assuming a total interaction rate of ∼10–15 kHz (based on recent isobar runs), the STAR DAQ rate of 2 kHz and the RHIC uptime of 50% (12 hour/day), tentative numbers of events we expect to record for different triggers are summarized in Table 11 for one week, default run plan, and two weeks as a more optimal running scenario. Note that we do not have an estimation of minimum-bias trigger efficiency at this point, and assumed it to be ∼100%.

Table 11: Event statistics (in millions) needed in an O+O run at $\sqrt{s_{\rm NN}}$ = 200 GeV for various triggers for one week (default) and two weeks (optimistic) running scenarios.

Triggers	Minimum bias	0–5% centrality
Events (1 week)	400 M	200 M
Events (2 week)	800 M	400 M

The statistics listed in Table 11 should allow precision measurements of many types of two-particle correlations, including the N_{ch} dependence of integral v_n, $p_{\rm T}$ dependence of v_n

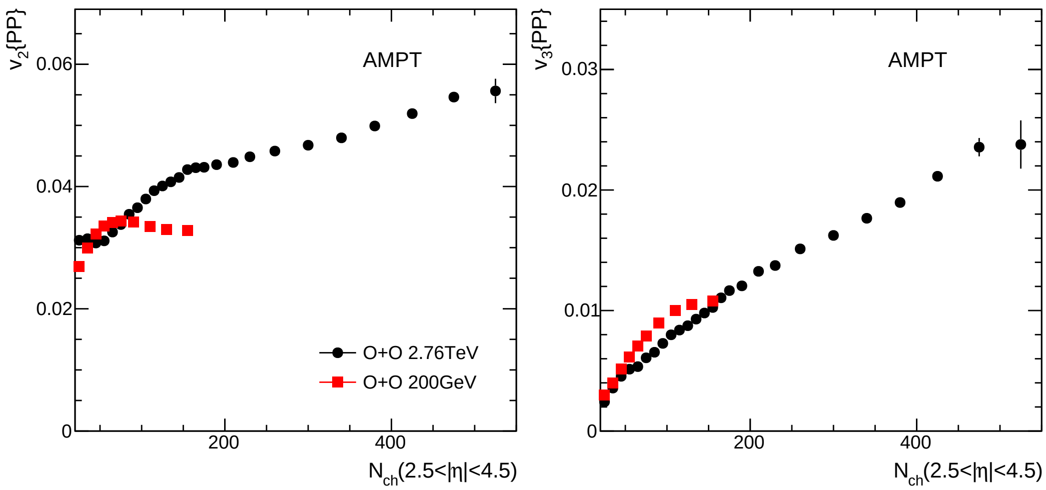

Figure 40: (Left) AMPT predictions of v_2 and (Right) v_3 (right) as a function of $N_{\rm ch}$ for O+O collisions, for $\sqrt{s_{\rm NN}} = 0.2$ TeV and 2.76 TeV.

in 0-5% for identified particles (π, K, p and ϕ) to test the NCQ-scaling. The non-flow effects for these observables can be studied in detail thanks to the large acceptance of iTPC and EPD. Based on a Glauber model estimation, the $\langle N_{\rm part}\rangle$ value is 9.5 and 26 for minimum-bias and 0-5% central O+O collisions, respectively.

Figure 41 shows the projection of the statistical precision for the ϕ meson $v_2(p_{\rm T})$ in 0–5% centrality O+O collisions. Under the assumption that its v_2 in O+O is similar to that of a charged hadron in p+Au around $p_{\rm T}$ ∼2–3 GeV/c, the estimation scales the ϕ $v_2(p_{\rm T})$ in peripheral Au+Au collisions [156] to approximately match the charged hadron v_2 in p+Au collisions in Fig. 39, accounting for differences in $\langle N_{\rm part}\rangle$, event plane resolution, and event statistics. A decent measurement of ϕ meson v_2 can be achieved with one week of running.

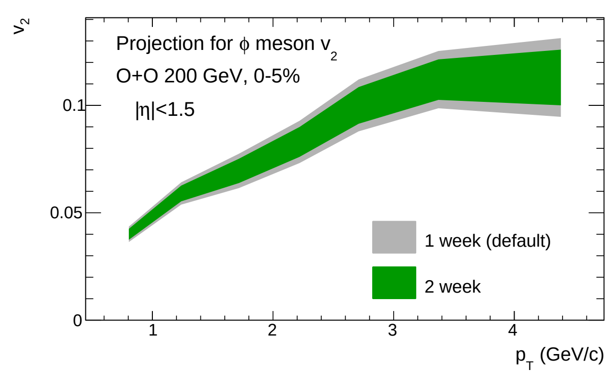

Figure 41: Projected statistical error on $v_2(p_{\rm T})$ central O+O collisions within the TPC acceptance.

In fact, the statistics requirement in Table 11 is mainly driven by multi-particle correlations, for example four-particle cumulants for single harmonics $c_2\{4\} = \langle v_n^4\rangle - 2\langle v_2^2\rangle^2$, four-particle symmetric cumulants $SC(2,3) = \langle v_2^2 v_3^2\rangle - \langle v_2^2\rangle\langle v_3^2\rangle$ and three-particle asymmetric cumulants $AC(2,4) = \langle v_2^2 v_4 \cos 4(\Phi_2 - \Phi_4)\rangle$ (Φ_n is the event plane). These observables are sensitive to event-by-event fluctuations of collectivity, and measurements of them at LHC in pp, p+Pb and Pb+Pb collisions have led to high impact results which provide evidence for geometry response in small systems [157, 158, 159, 160, 161].

Figure 42 shows the projection of the statistical precision for the $c_2\{4\}$ measurement. The projected precision should allow a measurement of $c_2\{4\}$ signal, assuming a $v_2\{4\}$ value to be between 4–6% [4].

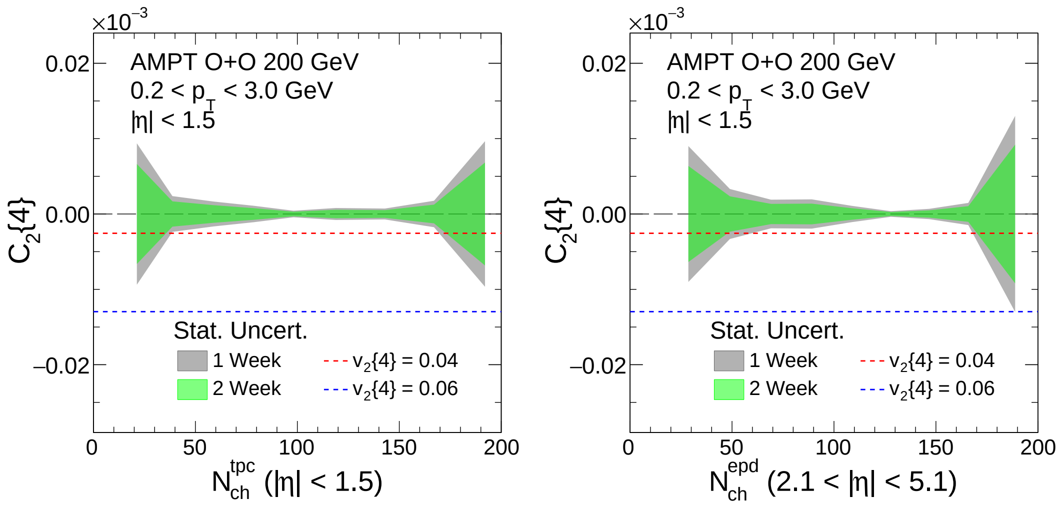

Figure 42: (Left) The projected statistical error bar on $c_2\{4\}$ in 0.2-3 GeV/c in the TPC acceptance as a function of number of charged particles in TPC acceptance and (Right) EPD acceptance.

[4]The p_{T} integrated $v_2\{4\}$ in d+Au from PHENIX [162] at forward rapidity is about 4%

3 Detector Updates and Operations

For the BES-II program STAR proposed three upgrades: the inner Time Projection Chamber (iTPC), the Event Plane Detector (EPD), and the endcap Time of Flight (eTOF). Figure 43 shows their overall location in the STAR detector. The EPD was installed and became operational for Run-18. The EPD replaces the BBC as a minimum-bias trigger detector and allows forward measurements of both centrality and event plane determination. The iTPC increases the acceptance of the TPC, it improves the dE/dx resolution, and allows tracks to be reconstructed down to p_T of $\sim$60 MeV/c. A single inner sector was installed for Run-18 and the full complement of 24 was installed for Run-19. The eTOF was installed on the east side of STAR, extending PID capabilities at forward rapidities. Three modules of eTOF were installed behind one of the TPC sectors for Run-18, with the whole detector completed for Run-19. These upgrades are described in more detail below.

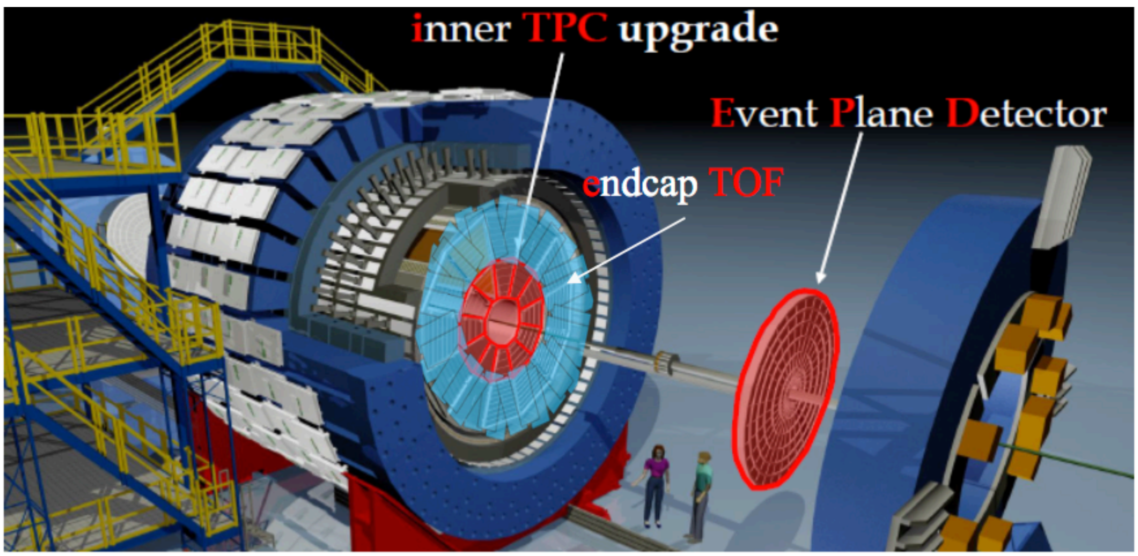

Figure 43: Rendering of the STAR detector with the BES-II upgrades highlighted in red. The EPD and iTPC are symmetric in STAR whereas the eTOF is only on the east side.

3.1 iTPC

The successful commissioning of the single iTPC sector during Run-18 was followed by the extensive installation work for the entire inner section of the upgraded detector. By the end of 2018 installation of all the elements, including the new electronics, was complete. Commissioning of the upgraded detector commenced at the beginning of January and by January 25 the entire TPC was ready for the data-taking, Figure 44 shows the completely upgraded inner sectors before (a) and after (b) the installation of the electronics. Cosmic data were collected for one month prior to the start of Run-19.

The upgrade brings more hermetic coverage to the inner part of the TPC, by having 72 padrows instead of the previously existing 45. Voltages on the inner sector anode wires were

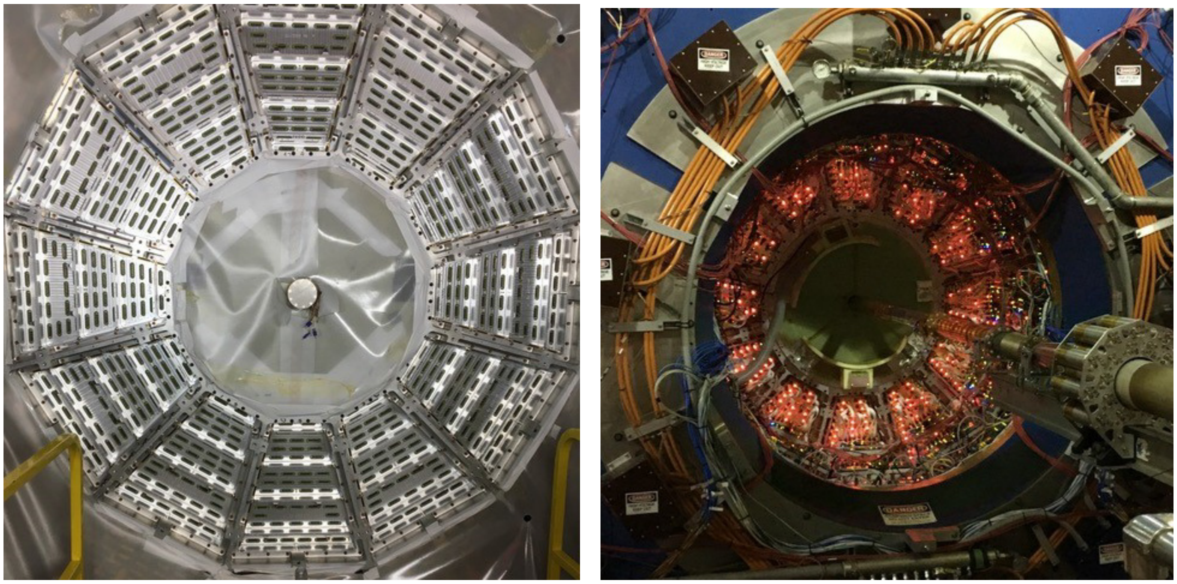

(a) All 12 new iTPC sectors on the west side.   (b) Electronics on the iTPC.

Figure 44: Images showing iTPC installation progress.

tuned to deliver gain comparable to that in outer sectors. Offline quality assurance is now done for the inner and outer sectors separately to monitor the performance of both. The integrated digital readout for a single run in each sector is shown on Fig. 45 for inner and outer sectors separately, demonstrating uniformity of the readout throughout the TPC (with the caveat that some readout electronics boards (RDO) are faulty and masked out, e.g. two of the four RDO boards in outer sector 5).

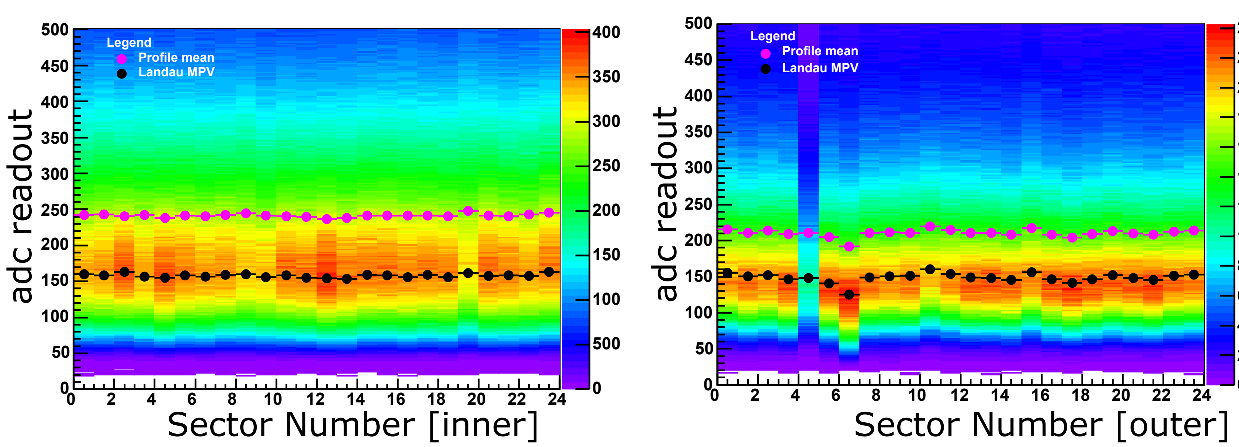

(a) Inner sectors - iTPC.   (b) Outer sectors.

Figure 45: Integrated adc readout for each sector.

Cosmic Running

Substantial amounts of cosmic data were requested prior to the start of Run-19 to have enough statistics for the alignment of the TPC; which is especially important in light of the newly installed inner sectors. A minimum of 0.5 million events in each sector was requested at both full-field and reverse full-field polarities of the magnetic field. Figure 46 shows the amount of cosmic tracks collected in each sector separately for each magnetic field polarity.

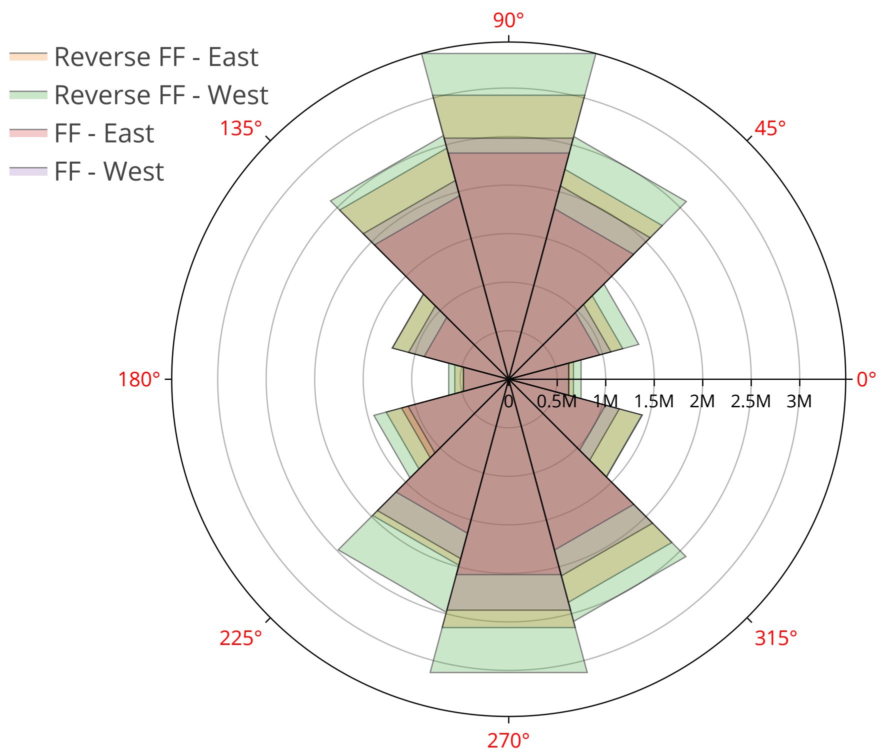

Figure 46: Distribution of cosmic tracks in TPC sectors.

Improvements Due to the iTPC

One of the main deliverables of the upgraded TPC is the extended pseudorapidity reach from $|\eta| < 1$ to $|\eta| < 1.5$. Figure 47(a) shows the distribution of the primary tracks' pseudorapidity for the current Run-19 and previous Run-18 (where only sector 20 was upgraded to iTPC).

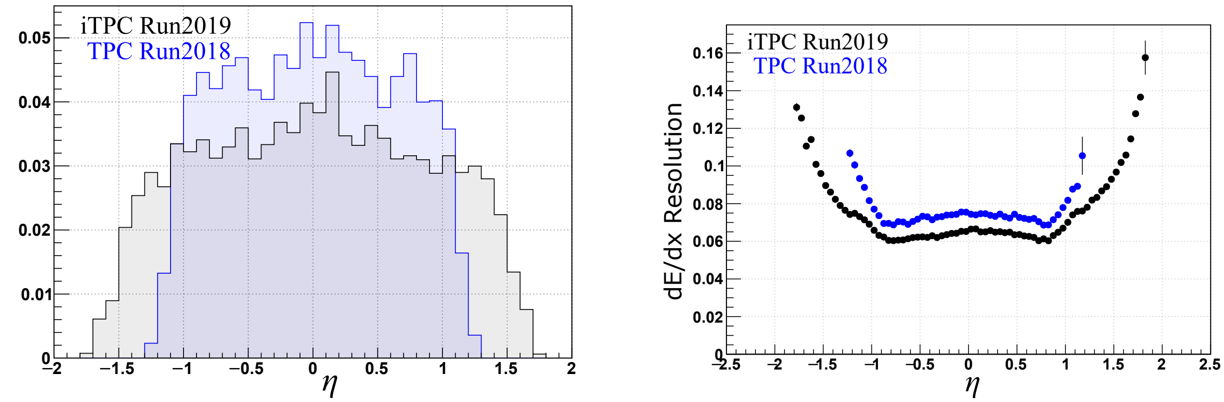

(a) Normalized distribution of pseudorapidity for Run-18 and Run-19. All tracks have at least 16 measured hits.

(b) dE/dx resolution as a function of pseudorapidity before and after the iTPC upgrade.

Figure 47: Improvements due to the iTPC upgrade.

In addition, the iTPC upgrade essentially adds more measured dx into the total sampled length of the track. This has direct impact on the resolution of the dE/dx measurement:

$$\sigma_{dE/dx} = 0.47N^{-0.46}(P \times h)^{-0.32}(dE/dx)_{trunc} \tag{1}$$

where h is the total sampled length of the track in the TPC [163]. This results in the dE/dx resolution improvement shown in Fig. 47(b) compared to that of the TPC before the upgrade.

3.2 Event Plane Detector

The Event Plane Detector (EPD), which operates as an event plane, centrality, and trigger detector was installed in the forward direction of STAR for Run-18. The detector has a pseudorapidity acceptance of $2.1 < |\eta| < 5.1$, with 16 radial segments and 24 azimuthal segments. The EPD allows both centrality and the event plane to be measured in the forward region, reducing the systematics due to autocorrelations for mid-rapidity analyses.

The EPD consists of two disks that are placed on either side of the STAR interaction region, in the former location of the Beam-Beam Counter (BBC) at $z = \pm$ 375 cm. The BBC small tiles were installed behind the EPD in order to calibrate the performance of the detector, and to have a redundancy in the trigger capabilities. The EPD scintillator is 1.2 cm thick and has 12 azimuthal segments, which span an angle of 30°, and have the label "super-sector". The EPD has a total of 744 channels, with each super-sector containing 31 tiles (the innermost tile spans the entire super-sector. The tile size was designed such that the probability of multiple particle hits in the same tile would be less than 10% at $\sqrt{s_{\mathrm{NN}}}$ = 19.6 GeV, based on $dN/d\eta$ measurements from PHOBOS [164]. This increases to 65% for Au+Au collisions at 200 GeV. More details on the EPD design can be found here [148]. Saturation of the signal can occur if the input to the 12-bit ADC is larger than the maximum value of 4096, or more than one photon is incident on a SiPM pixel. In both 2017 and 2018 data, there is no evidence of saturation due to either effect for up to 4-MIP events.

In both Run-18 and Run-19, the EPD had signals in all 744 of its tiles. The detector was timed in and the bias voltages were set within the first day of operations for both years. In Run-19, the EPD has been used as the main trigger detector as it has a greater acceptance than either the VPD or ZDC, and has better timing resolution than the BBC. Only the inner 216 tiles, with an acceptance of $3.28 < |\eta| < 5.1$, were used in the trigger logic. The EPD timing resolution in Run-19 for the $\sqrt{s_{\mathrm{NN}}} = 19.6$ GeV data taking period was 0.75 ns, which is shown in Fig. 48. Due to the multiplicity of heavy-ion collisions a fastest TAC algorithm was utilized.

The EPD triggering algorithm was designed so that it could be used to select against background events, which come from the beam interacting with the beam pipe or other material within the accelerator. In BES-I this was a significant problem at the lowest energies where the transverse size of the beam was large. The EPD can require that collisions have a symmetry in the number of hits in East compared to West. This optimization was not needed in Run-19, where we found that simply requiring 3 hits in East and 3 hits in West was sufficient to remove enough background in the 19.6 GeV collisions and that a single hit in East and West were sufficient at 14.5 GeV. This functionality may be important for Run-20 depending on the relative rates of beam-beam to beam-pipe interactions.

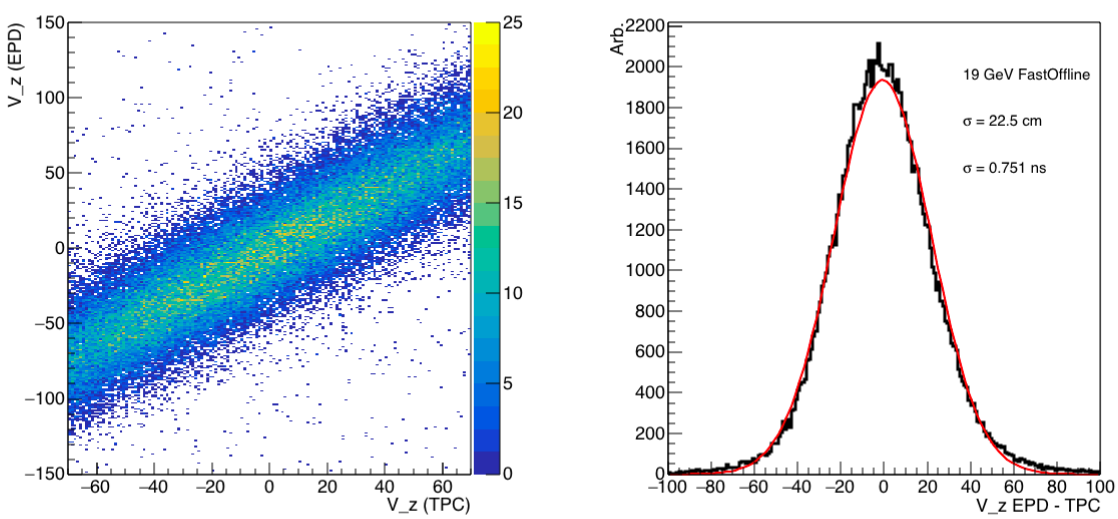

Figure 48: (Left) Correlation between the offline vertex found by the TPC and the vertex found by the EPD for events with ten or more reconstructed tracks at mid-rapidity. (Right) The difference between the EPD and TPC vertices for the same events, fitted with a Gaussian in red.

The entire EPD has been used to measure four different systems with a very uniform response, as illustrated in Fig. 49. The peak of the first MIP peak for all systems is in nearly the same place, though subtle differences will be corrected for in the calibrations database.

For the innermost tiles, the greater contribution of the second and beyond MIP peaks for the higher energy can be seen. For the outermost tiles, which have the least multiplicity, the difference between the systems is minimal.

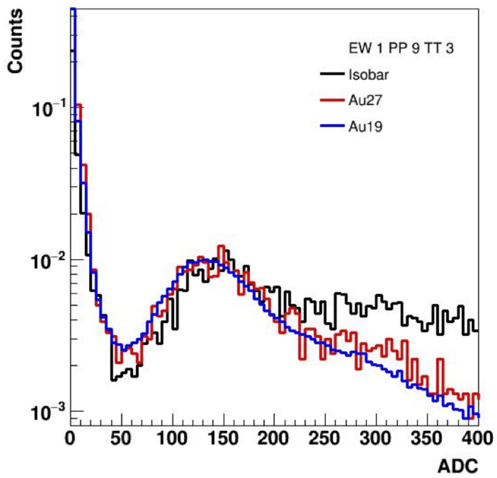

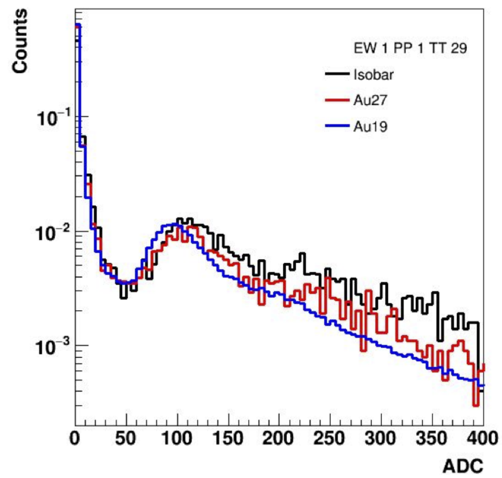

Figure 49: (Left) MIP peaks in three of the four systems recorded with the full EPD for an inner tile. The Isobar data at 200 GeV are in black, the Au+Au at 27 GeV are in red and the Au+Au at 19.6 GeV are in blue. (Right) MIP peaks for three of the four systems for an outermost tile.

The EPD will be used to measure both the event plane and centrality at forward rapidities. Studies are underway to maximize the performance versus collision system, however preliminary results from Run-18 are promising. In Fig. 50 the distribution of the first order event plane as measured by the EPD in $\sqrt{s_{NN}}$=27 GeV is shown. Additionally, the event plane resolution from the EPD is compared to the event plane resolution as measured by the BBC, and is nearly twice as good for the first order event plane. The precise resolution of the event plane depends on the collision system and the event plane order. The EPD will allow us to measure the event plane outside of the iTPC acceptance, which removes the effects of auto-correlations in flow analyses.

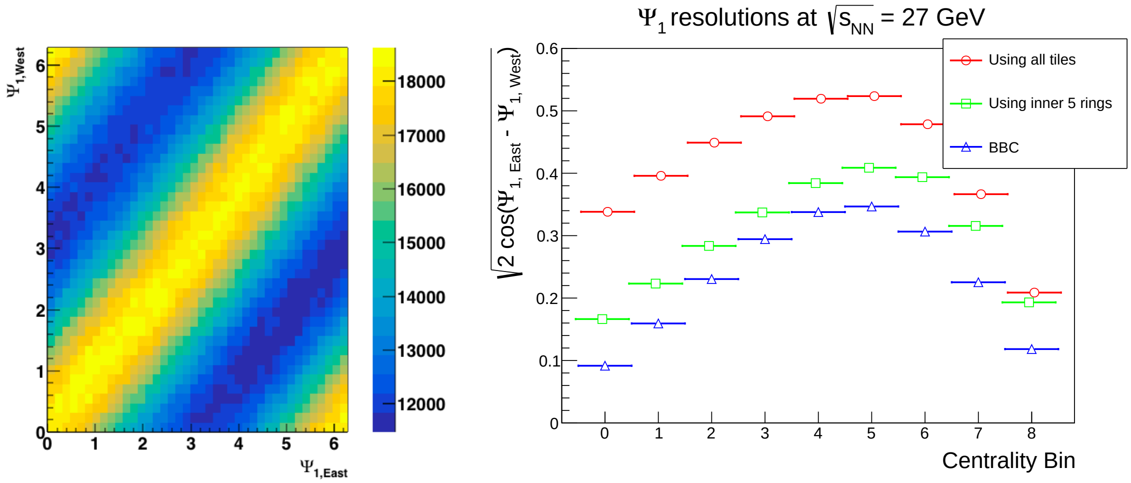

Figure 50: (Left) Correlation between $\Psi_{1,\mathrm{East}}$ vs. $\Psi_{1,\mathrm{West}}$ as measured by the EPD in semi-central Au+Au collisions at $\sqrt{s_{NN}} = 27$ GeV. (Right) The event plane resolution in the same data for the BBC inner tiles in blue, the EPD inner tiles in green and the entire EPD in red. The first two centrality bins are roughly 0-5% and 5-10%, the other bins have a width of 10% in centrality.

3.3 Endcap Time-of-Flight Detector

The addition of an endcap Time-of-Flight (eTOF) detector to STAR strengthens the physics potential of the experiment during the BES-II experimental campaign [149]. The eTOF detector crucially complements the particle identification capabilities at forward-to-mid rapidities for the collider and fixed target programs. eTOF is a joint project between the STAR collaboration and institutions from the CBM collaboration: University of Heidelberg, Technical University of Darmstadt, GSI-Helmholtz Center for Heavy-Ion Research, Tsinghua, Central China Normal University, and University of Science and Technology of China. This synergy project is a part of the so-called FAIR Phase-0 program and provides CBM with important operational experience via a large-scale integration test of the future CBM TOF.

The eTOF wall contains two types of Multi-gap Resistive Plate Chambers (MRPCs) [165]: (i) 36 high rate capability counters (MRPC3a) with 0.7 mm thick low resistive glass as electrode material were produced at Nuctech in Beijing; (ii) 72 counters (MRPC3b) with normal float glass at a thickness of 0.28 mm as electrode material were produced at USTC/Hefei [166]. Both counter types are full size prototypes for the CBM TOF. Most of them were tested and delivered to Heidelberg University where integration into modules took place. Each module consists of 3 MRPCs with a 32 strip segmented readout electrode. Each strip is read out from both sides (to achieve a position resolution below 5 mm along the strip), thus a total of 6912 readout channels build up the eTOF wheel. The module production was finished in August 2018, all modules were extensively tested using a cosmic setup (installed at Heidelberg University) prior to shipping to BNL. The eTOF was installed at the East end of STAR in the small gap between the poletip and the TPC; behind its readout electronics. The modules are arranged in 12 sectors matching those of the TPC. The installation of the eTOF was completed in November 2018.

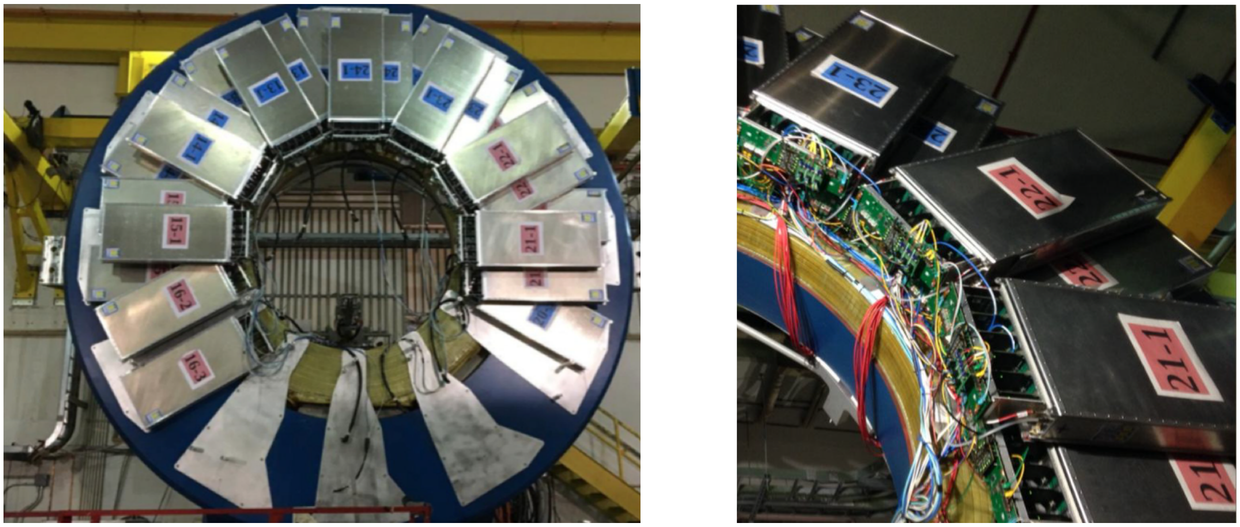

Figure 51: (Left) Photograph of eTOF in the service position. (Right) Photograph of eTOF zoomed in on the region of the readout electronics.

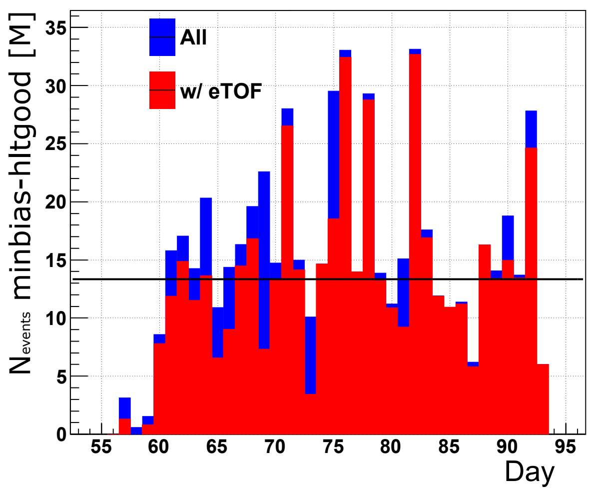

Figure 52: Day-by-day statistics accumulated during Au+Au 19.6 GeV run. Blue bars: Good HLT minimum bias events, red bars: Good HLT minimum bias event with eTOF.

The detector modules are equipped with readout cards containing ultrafast and radiation-tolerant ASICs for pre-amplification followed by CERN GBTx-based radiation-tolerant data transmission units. The signals delivered by the eTOF are processed by PADIX (a preamplifier 32 channel board inside the module box) as front-end electronics, a feed-through PCB. The further processing and readout of the signals are performed by a free-streaming DAQ system equipped with the TDC 32 channel board with GET4 V2.0 chip, a back-plane board with GBTx chip distributing the power and the clock to the FEE cards, AFCK boards placed in a μTCA crate at 8 m distance from the modules. Further downstream, the data streams are forwarded via FLES Input Boards (FLIB) placed in a rack mount PC located in the DAQ room about 100 m from the setup. The connection between the module backplane to the AFCK (via GBT link) and from the AFCK to the FLIB (via FLIM link) is an optical fiber. Thus, the CBM free streaming readout system was successfully integrated to the trigger

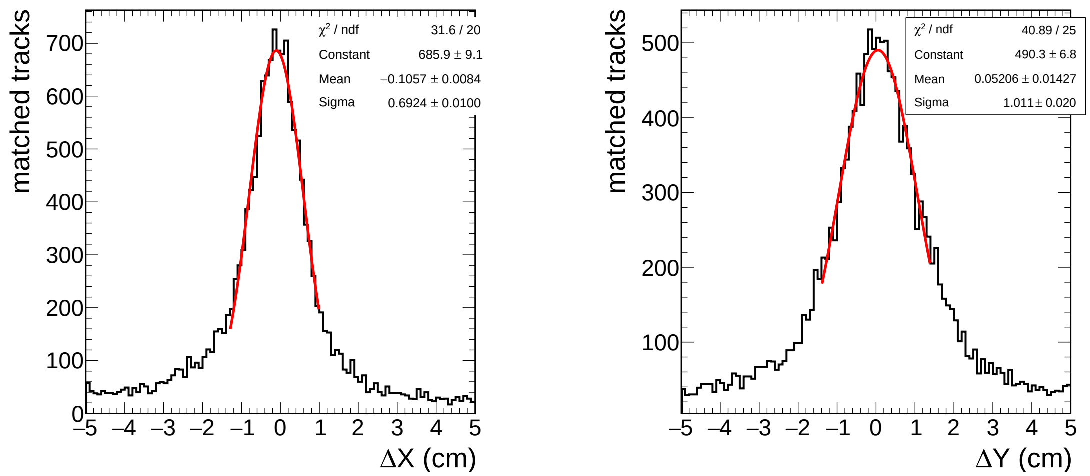

Figure 53: (Left) Matching quality between TPC/iTPC track candidate and eTOF hit across strips (local X coordinate). (Right) Matching quality along the strips (local Y coordinate).

based readout system of STAR.

The Au+Au 19.6 GeV BES-II production run started on February 25, 2019. Figure 52 shows the day-by-day accumulated statistics of the minimum bias events. The red curve shows that the eTOF was included in about 85% of collected events. By the end of the 19.6 GeV run the eTOF was present in nearly 100% of the data collected.

The main goal of the eTOF detector is to provide excellent time resolution of the order of < 100 ps, and a position resolution along the strip of < 5 mm. The software for the eTOF data unpacking, calibration, building of hits, track matching and particle identification was developed. It is accessible in the STAR analysis framework and allows for an online and fast offline analysis of the collected data. As discussed above, the counters inside the module have an overlap of two strips, thus a signal is generated on both MRPCs. From the hits in the overlapping region a system time resolution can be estimated and was found to be $\tau_{system} = 85$ ps. To recall, the intrinsic detector time resolution is $\tau_{RPC} = 65$ ps. The accuracy of the position determination of a hit, directly impacts the matching quality between the eTOF and the TPC systems. The longitudinal coordinate along the MRPC is calculated by the time difference between measured times at both ends (Y hit). The local transverse coordinate (X hit) is the center of the cell or a weighted average in case of clustered hits. In order to estimate the matching quality, the TPC tracks are extrapolated to the eTOF plane using an ideal helix as a track model. The difference between the TPC track intersection and reconstructed eTOF hit position is shown in Fig. 53 (left/right panel) across/along the strips. The Gaussian width of these distributions is < 10 mm in both cases, accurate enough to prevent fake matches.

The left panel of Fig. 54 shows the ratio of the number of reconstructed TPC tracks matched to an eTOF hit to the number of tracks intersecting the eTOF. The ratio varies between 0.3 and 0.5 and includes track candidate losses due to intrinsic detector inefficiencies, and the hit finder and track matching quality. The matching efficiency as a function of

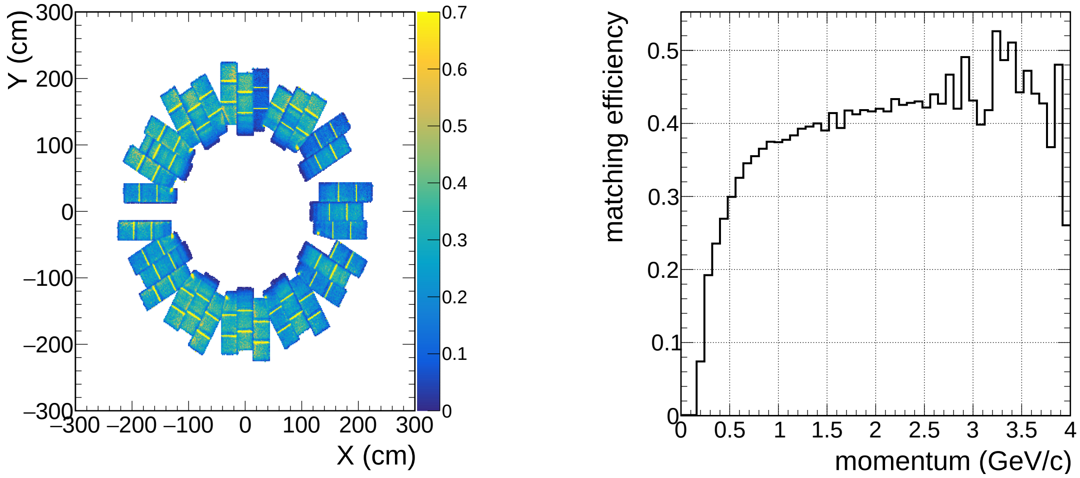

Figure 54: (Left) Ratio between the number of tracks matched to reconstructed eTOF hits and the number of potential track intersections with the eTOF using an ideal helix track model. (Right) Matching efficiency as a function of momentum in one of the eTOF sectors.

momentum for one sector is shown in the right panel of Fig. 54 and reaches 0.45 for tracks with momentum $p > 1$ GeV$/c$.

Thanks to the excellent time resolution of eTOF, the different particle species are clearly visible over a wide momentum range in the velocity versus momentum distribution for the TPC/iTPC track candidates matched to eTOF hit, as shown in Fig. 55 (left panel). Figure 55 (right panel) shows the raw phase-space ($p_{\mathrm{T}} - y$) distribution of identified protons in Au+Au collisions at $\sqrt{s_{NN}} = 14.6$ GeV. Protons are identified by applying a cut on the squared mass obtained from the time-of-flight measurement in the barrel-TOF or eTOF. The red curves indicate the extended phase-space ($-1.0 < \eta < -1.7$) covered by the eTOF acceptance.

Though the detector alignment and calibration need to be carefully done, this online performance of the detector demonstrates its readiness for precision physics.

During Run-19 operation of the eTOF the slow control and monitor software available to the shift crew was developed and continuously improved, allowing for the efficient inclusion of the eTOF system into the STAR data taking. The system has been kept in a running state throughout the run so far although some beam induced damage occurred to parts of the front-end electronics.

In a major event on April 30th, 2019 that caused a HV trip of the full system about 20% of the front-end channels were destroyed, followed by other events that reduced the number of working channels to about 40% in May 2019. The reason for these massive damages is currently not understood. As a counter measure the front-end boards of the eTOF MRPCs have been redesigned to include more electro-static-discharge protection for each data input line of the preamplifier chip PADI. Major repair work will be executed in the second half of 2019 with the goal of restoring the full eTOF performance by the end of 2019, prior to Run-20.

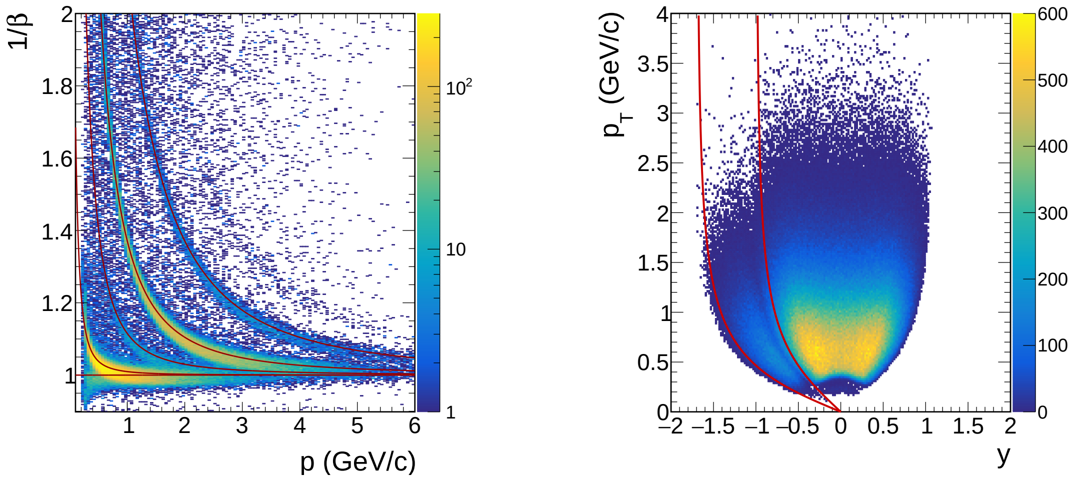

Figure 55: (Left) The inverse velocity vs momentum of matched TPC tracks to eTOF hits from a fixed target test run. (Right) Transverse momentum versus rapidity distribution of identified protons in the Au+Au 14.6 GeV run. The red curves indicate the extension of coverage enabled by the eTOF upgrade.

3.4 Forward Detector Upgrades

As described in Sect. 1.2 and 2.2 recent STAR efforts using the FMS and a pre- and post-shower detector upgrade from data taken during 2015-2017 have demonstrated the existence of outstanding QCD physics opportunities in the forward region. However, superior detection capability for neutral pions, photons, electrons, jets and leading hadrons covering a region of $2.5 < \eta < 4.5$ are required. Therefore we have proposed a forward detector system, realized by combining tracking with electromagnetic and hadronic calorimeters for the years beyond 2020. The design of the Forward Calorimeter System (FCS) is driven by consideration of detector performance, integration into STAR and cost optimization. The refurbished PHENIX sampling ECal is used and the hadronic calorimeter will be a sandwich iron scintillator plate sampling type, based on the extensive STAR Forward Upgrade and EIC Calorimeter Consortium R&D and will utilize STAR's existing Forward Preshower Detector. Both calorimeters share the same cost-effective readout electronics, with SiPMs as photo-sensors. This FCS system will have very good ($\sim 10\%/\sqrt{E}$) electromagnetic and ($\sim 50\%/\sqrt{E} + 10\%$) hadronic energy resolutions. Integration into STAR requires minimal modification of existing infrastructure. In addition, a Forward Tracking System (FTS) is proposed. The FTS must be capable of discriminating hadron charge sign for transverse asymmetry and Drell-Yan measurements in p+A. In heavy ion collisions, measurements of charged particle transverse momenta of $0.2 < p_{\mathrm{T}} < 2$ GeV/c with 20-30% momentum resolution are required. To keep multiple scattering and photon conversion background under control, the material budget of the FTS must be small. Hence, the FTS design is based on three Silicon mini-strip detectors that consists of disks with a wedge-shaped design to cover the full azimuth and $2.5 < \eta < 4.0$; they are read out radially from the outside to minimize the material. The Si-disks are combined with four small-strip Thin Gap Chamber (sTGC) wheels following the ATLAS design [167, 168]. These extremely cost effective sTGCs can also be seen as an alternative tracking detector technology to the planned GEM-trackers in the forward arms of current EIC detector designs. The Si mini-strip disks will be placed in the region $z = 140 - 187$ cm. The 4 sTGC wheels would be placed 30 cm apart starting from $z = 273$ cm. The Si-Disks readout is based on APV chips, which allows us to reuse the readout chain of the IST, which was part of the STAR HFT. For the sTGC the plan is to read it with the TPC electronics just unmounted TPX electronics.

3.4.1 Status

The June 2018 PAC recommended the FCS and all other STAR forward upgrade components be ensured to have a sound technical basis, hold to the estimated cost, and be ready to be installed and commissioned without beam for a 500 GeV RHIC polarized *pp* run to begin mid-August 2021. To this end the BNL ALD for NPP convened a cost and schedule review in November 2018 [169]. The outcome of the review can be summarized as: "A five-member review panel (S. Boose, C. Miraval, G. van Nieuwenhuizen, A. Tricoli, and chaired by G. Young) conducted a review of the resource requirements for the proposed forward upgrades to the STAR detector on November 19, 2018. The panel noted good progress on the proposed concept for a cold-QCD experiment to run in late FY2021 at RHIC, with plausible plans for funding and conservative designs for all detector components, electronics, and support infrastructure. The panel opined that the major project risks are identified and that the experiment appears positioned to be ready for first operation in 2021."

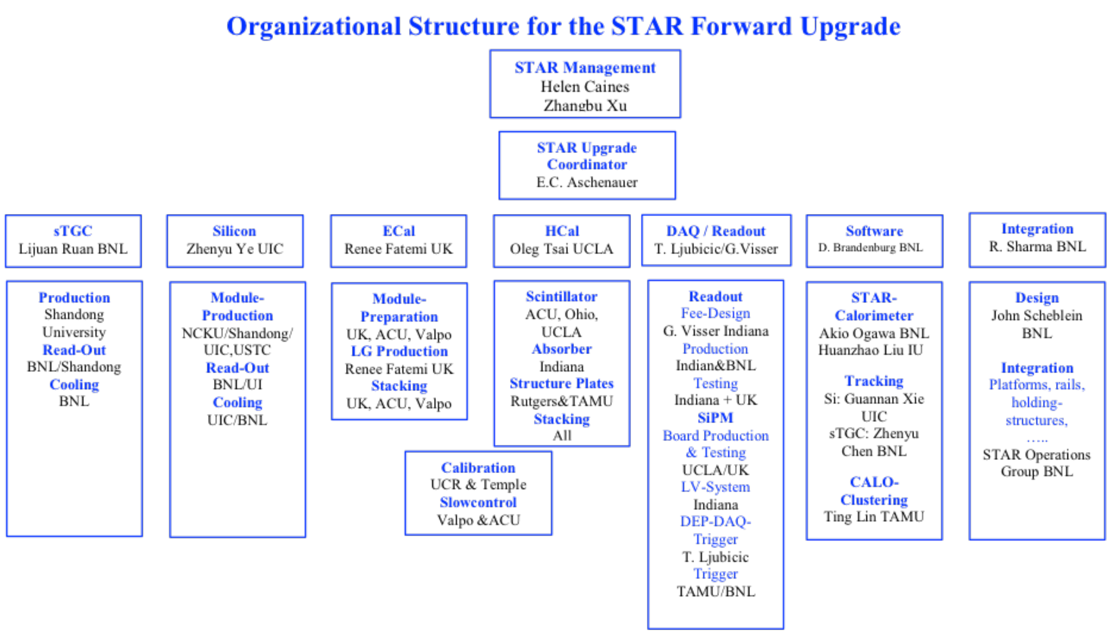

Figure 56: The organizational structure for the STAR forward upgrade.

Since the review the project team (see Fig. 56) has concentrated on the following topics.

- Submission of a NSF MRI proposal for the ECAL and HCAL, including its read-out electronics under the leadership of Prof. S. Wissink from Indiana University.
- Securing funding for the sTGCs and the Silicon subdetectors in China through proposals to MOST, NSFC and start-up funds at Shandong University, and funding from NCKU in Taiwan.
- Securing one of the PHENIX ECAL super sectors and preparing its towers to be restacked as the forward ECal during the summer 2019 RHIC shutdown.
- Finalizing the design of the ECAL and HCAL readout electronics, i.e. SiPM boards, FEEs and the digitizer and trigger processor boards
- Finalizing the design of the "FMS platform" modifications required to install the calorimeters (see Fig. 57). The safety reviews with CAD have been finalized and the final design drawings are ready and fabrication of the parts will start soon, to allow the modifications to be done during the summer 2019 RHIC shutdown, before the ECAL gets installed.
- Production of a full scale prototype of a quadrant of a sTGC – plane (see Fig. 58).
- Production of a full scale prototype Si-detector wedge.
- Operation of final prototypes of the preshower, ECAL, HCAL, their readout electronics, and an sTGC quadrant during the current STAR data taking.
- Finalizing all the integration of the 4 subdetectors into STAR, see for example Fig. 58 for the Silicon detector.
- Developing tracking and clustering software algorithms.

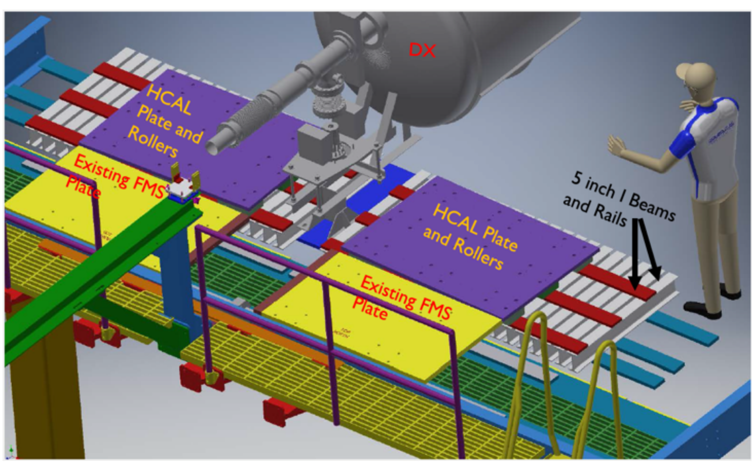

Figure 57: Design of the ECAL and HCAL platform.

The STAR forward upgrade design and existing detailed schedule obeys several overall requirements:

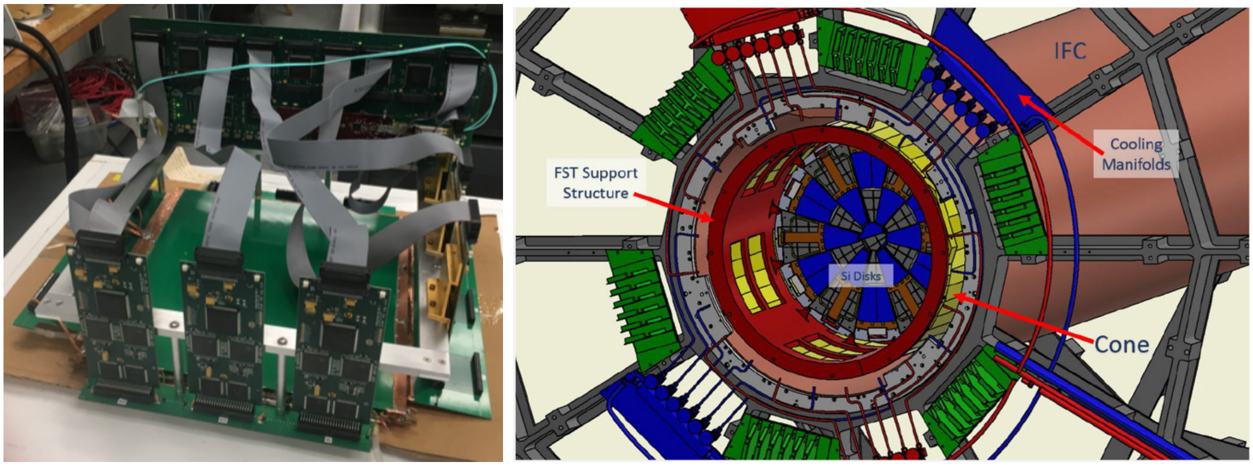

Figure 58: (Left) sTGC quadrant full scale prototype including its mounting structure with FEE's and RDO's installed. (Right) 3-D view of the Silicon detector integrated into STAR.

- The RHIC operations schedule requires that the installation of the forward upgrade needs to be done without rolling STAR into the assembly hall.
- HCAL and ECAL need to be movable transverse to the RHIC beam pipe to allow access to RHIC accelerator components.
- Calorimeter platform modifications and ECAL stacking needs to be done during the RHIC shutdown August 2019 to January 2020
- HCAL, SiPMs and all readout electronics (FEE, DEP and Trigger) installation needs to be completed during the RHIC shutdown August 2020 to January 2021
- The sTGC-subdetector needs to be installed without breaking the beam vacuum and needs to be ready for installation during the RHIC shutdown August 2020 to January 2021.
- The Silicon-subdetector needs to be installed without breaking the vacuum. It will be installed in Summer 2021 before the planned 500 GeV *pp* run earliest at the end of FY21.
- The STAR forward upgrade needs to be ready for physics data taking starting earliest mid-August 2021

A Charge to the STAR Collaboration

Dear Helen & Zhangbu:

I am writing to solicit the STAR beam use request for RHIC Run-20 and to request presentations at this year's PAC meeting, which is scheduled to be held on June 10-11, 2019.

The 2020 RHIC run will be the second year of the planned three-year high statistics beam energy scan. The 2018 PAC tentatively assigned first priority for Runs 20-21 to data taking in the collider mode at 7.7, 9.1, and 11.5 GeV CM energy, accumulating at least 100M, 160M, and 230M min bias events, respectively. Second priority was assigned to fixed target runs at 3.0, 3.2, 3.5, 5.2, and 6.2 GeV CM energy, acquiring at least 100M events at each energy, but did not specify exactly in which order these data should be taken, except that optimal use should be made of the availability of electron cooling to enhance the luminosity.

The STAR collaboration should not simply take these tentative recommendations as a given, but reconsider and justify the prioritized set of beam energies and the requested accumulated statistics at each energy, assuming either a 24 or a 28 cryo-week run in FY2020, followed by a 20 cryo-week run in FY2021. STAR should also consult with C-AD about the number of dedicated LEReC commissioning weeks that are expected to be required during Run-20.

In addition, I request presentations on (i) the status of data analysis from previous RHIC runs and (ii) an update of the physics goals for a short (16 cryo-weeks) forward Spin physics run in FY22 with 500 GeV p+p collisions.

The beam use request should be submitted no later than May 15 in order to allow the PAC members to study it in detail before the meeting.

Best regards
Berndt

References

[1] STAR. STAR Public Note SN0669 - The STAR midrapidity pp, pA, AA physics program beyond BES-II. https://drupal.star.bnl.gov/STAR/starnotes/public/sn0669.

[2] STAR. STAR Public Note SN0648 - The STAR Forward Calorimeter System and Forward Tracking System beyond BES-II. https://drupal.star.bnl.gov/STAR/starnotes/public/sn0648.

[3] P. Wang. Γ measurements in Au+Au collisions at $\sqrt{s_{NN}} = 200$GeV with the STAR experiment. *Nucl. Phys.*, A982:723–726, 2019.

[4] Yan-Qing Ma and Raju Venugopalan. Comprehensive Description of J/ψ Production in Proton-Proton Collisions at Collider Energies. *Phys. Rev. Lett.*, 113(19):192301, 2014.

[5] Yan-Qing Ma, Kai Wang, and Kuang-Ta Chao. $J/\psi(\psi')$ production at the Tevatron and LHC at $\mathcal{O}(\alpha_s^4 v^4)$ in nonrelativistic QCD. *Phys. Rev. Lett.*, 106:042002, 2011.

[6] Yan-Qing Ma and Ramona Vogt. Quarkonium Production in an Improved Color Evaporation Model. *Phys. Rev.*, D94(11):114029, 2016.

[7] Jaroslav Adam et al. First observation of the directed flow of D^0 and $\overline{D^0}$ in Au+Au collisions at $\sqrt{s_{\rm NN}} = 200$ GeV. *subm. to Phys. Rev. Lett.*, arXiv:1905.02052, 2019.

[8] Sandeep Chatterjee and Piotr Bożek. Large directed flow of open charm mesons probes the three dimensional distribution of matter in heavy ion collisions. *Phys. Rev. Lett.*, 120(19):192301, 2018.

[9] Santosh K. Das, Salvatore Plumari, Sandeep Chatterjee, Jane Alam, Francesco Scardina, and Vincenzo Greco. Directed Flow of Charm Quarks as a Witness of the Initial Strong Magnetic Field in Ultra-Relativistic Heavy Ion Collisions. *Phys. Lett.*, B768:260–264, 2017.

[10] L. Adamczyk et al. Observation of D^0 Meson Nuclear Modifications in Au+Au Collisions at $\sqrt{s_{NN}} = 200$ GeV. *Phys. Rev. Lett.*, 113(14):142301, 2014. [Erratum: Phys. Rev. Lett.121,no.22,229901(2018)].

[11] J. Adam et al. Centrality and transverse momentum dependence of D^0-meson production at mid-rapidity in Au+Au collisions at $\sqrt{s_{\rm NN}} = 200\,$GeV. *Phys. Rev.*, C99(3):034908, 2019.

[12] L. Zhou. Measurements of Λ_c^+ and D_s^+ productions in Au+Au collisions at $\sqrt{s_{NN}} = 200$ GeV from STAR. *Nucl. Phys.*, A967:620–623, 2017.

[13] S. Radhakrishnan. Measurements of open charm production in Au+Au collisions at $\sqrt{s}_{NN} = 200$GeV with the STAR experiment at RHIC. *Nucl. Phys.*, A982:659–662, 2019.

[14] J. Adam et al. Precise measurement of the mass difference and the binding energy of hypertriton and antihypertriton. *subm. to Nature Physics*, arXiv:1904.10520, 2019.

[15] W. Gajewski et al. A compilation of binding energy values of light hypernuclei. *Nucl. Phys.*, B1:105–113, 1967.

[16] G. Bohm et al. A determination of the binding-energy values of light hypernuclei. *Nucl. Phys.*, B4:511–526, 1968.

[17] G. Keyes, M. Derrick, T. Fields, L. G. Hyman, J. G. Fetkovich, J. Mckenzie, B. Riley, and I. T. Wang. Properties of (lambda)he-3. *Phys. Rev.*, D1:66–77, 1970.

[18] Peter J. Mohr, David B. Newell, and Barry N. Taylor. CODATA Recommended Values of the Fundamental Physical Constants: 2014. *Rev. Mod. Phys.*, 88(3):035009, 2016.

[19] J. Adam et al. Beam energy dependence of (anti-)deuteron production in Au+Au collisions at RHIC. *accepted by PRC*, arXiv:1903.11778, 2019.

[20] W. Busza and A. S. Goldhaber. Nuclear Stopping Power. *Phys. Lett.*, B139:235, 1984.

[21] T. Abbott et al. Measurement of particle production in proton induced reactions at 14.6-GeV/c. *Phys. Rev.*, D45:3906–3920, 1992.

[22] T. Abbott et al. Charged hadron distributions in central and peripheral Si + A collisions at 14.6-A/GeV/c. *Phys. Rev.*, C50:1024–1047, 1994.

[23] L. Ahle et al. Particle production at high baryon density in central Au + Au reactions at 11.6-A-GeV/c. *Phys. Rev.*, C57:466–470, 1998.

[24] J. Barrette et al. Forward baryons in relativistic nucleus-nucleus collisions. *Phys. Rev.*, C45:819–832, 1992.

[25] J. Barrette et al. Centrality dependence of longitudinal and transverse baryon distributions in ultrarelativistic nuclear collisions. *Phys. Rev.*, C50:3047–3059, 1994.

[26] S. E. Eiseman et al. Rapidity distributions and nuclear transparency in heavy ion collisions. *Phys. Lett.*, B292:10–12, 1992.

[27] S. E. Eiseman et al. Rapidity distributions of K_s^0s and Lambdas produced by 14.6-A/GeV/c Si beams on Si and Pb targets. *Phys. Lett.*, B297:44–48, 1992.

[28] J. Adam et al. Measurements of Dielectron Production in Au+Au Collisions at $\sqrt{s_{NN}}=$ 27, 39, and 62.4 GeV from the STAR Experiment. *subm. to PRL*, arXiv:1810.10159, 2018.

[29] J. Adam et al. Low-p_T e^+e^- pair production in Au+Au collisions at $\sqrt{s_{NN}} = 200$ GeV and U+U collisions at $\sqrt{s_{NN}} = 193$ GeV at STAR. *Phys. Rev. Lett.*, 121(13):132301, 2018.

[30] G. Antchev et al. Evidence for non-exponential elastic proton–proton differential cross-section at low |t| and $\sqrt{s}$=8 TeV by TOTEM. *Nucl. Phys.*, B899:527–546, 2015.

[31] G. Antchev et al. First measurement of elastic, inelastic and total cross-section at $\sqrt{s} = 13$ TeV by TOTEM and overview of cross-section data at LHC energies. *Eur. Phys. J.*, C79(2):103, 2019.

[32] Betty Abelev et al. Long-range angular correlations on the near and away side in p-Pb collisions at $\sqrt{s_{NN}} = 5.02$ TeV. *Phys. Lett.*, B719:29–41, 2013.

[33] Georges Aad et al. Observation of Associated Near-Side and Away-Side Long-Range Correlations in $\sqrt{s_{NN}}$=5.02 TeV Proton-Lead Collisions with the ATLAS Detector. *Phys. Rev. Lett.*, 110(18):182302, 2013.

[34] L. Adamczyk et al. Long-range pseudorapidity dihadron correlations in d+Au collisions at $\sqrt{s_{\rm NN}} = 200$ GeV. *Phys. Lett.*, B747:265–271, 2015.

[35] A. Adare et al. Quadrupole Anisotropy in Dihadron Azimuthal Correlations in Central d+Au Collisions at $\sqrt{s_{_{NN}}}$=200 GeV. *Phys. Rev. Lett.*, 111(21):212301, 2013.

[36] Georges Aad et al. Observation of Long-Range Elliptic Azimuthal Anisotropies in $\sqrt{s}$ =13 and 2.76 TeV pp Collisions with the ATLAS Detector. *Phys. Rev. Lett.*, 116(17):172301, 2016.

[37] Peifeng Liu and Roy A. Lacey. System-size dependence of the viscous attenuation of anisotropic flow in p + Pb and Pb + Pb collisions at energies available at the CERN Large Hadron Collider. *Phys. Rev.*, C98(3):031901, 2018.

[38] Zuo-Tang Liang and Xin-Nian Wang. Globally polarized quark-gluon plasma in non-central A+A collisions. *Phys. Rev. Lett.*, 94:102301, 2005. [Erratum: Phys. Rev. Lett.96,039901(2006)].

[39] Sergei A. Voloshin. Polarized secondary particles in unpolarized high energy hadron-hadron collisions? *arXiv*, nucl-th/0410089, 2004.

[40] L. Adamczyk et al. Global Λ hyperon polarization in nuclear collisions: evidence for the most vortical fluid. *Nature*, 548:62–65, 2017.

[41] Jaroslav Adam et al. Global polarization of Λ hyperons in Au+Au collisions at $\sqrt{s_{_{NN}}}$ = 200 GeV. *Phys. Rev.*, C98:014910, 2018.

[42] Sergei A. Voloshin, Arthur M. Poskanzer, and Raimond Snellings. Collective phenomena in non-central nuclear collisions. *Landolt-Bornstein*, 23:293–333, 2010.

[43] Ulrich Heinz and Raimond Snellings. Collective flow and viscosity in relativistic heavy-ion collisions. *Ann. Rev. Nucl. Part. Sci.*, 63:123–151, 2013.

[44] Sergei A. Voloshin. Vorticity and particle polarization in heavy ion collisions (experimental perspective). In *Proceedings, 17th International Conference on Strangeness in Quark Matter (SQM 2017): Utrecht, The Netherlands, July 10-15, 2017*, 2017. [EPJ Web Conf.17,10700(2018)].

[45] F. Becattini and Iu. Karpenko. Collective Longitudinal Polarization in Relativistic Heavy-Ion Collisions at Very High Energy. *Phys. Rev. Lett.*, 120(1):012302, 2018.

[46] Xiao-Liang Xia, Hui Li, Ze-Bo Tang, and Qun Wang. Probing vorticity structure in heavy-ion collisions by local Λ polarization. *Phys. Rev.*, C98:024905, 2018.

[47] F. Becattini and Iu. Karpenko. Collective Longitudinal Polarization in Relativistic Heavy-Ion Collisions at Very High Energy. *Phys. Rev. Lett.*, 120(1):012302, 2018.

[48] Masayuki Asakawa and Masakiyo Kitazawa. Fluctuations of conserved charges in relativistic heavy ion collisions: An introduction. *Prog. Part. Nucl. Phys.*, 90:299–342, 2016.

[49] Xiaofeng Luo and Nu Xu. Search for the QCD Critical Point with Fluctuations of Conserved Quantities in Relativistic Heavy-Ion Collisions at RHIC : An Overview. *Nucl. Sci. Tech.*, 28(8):112, 2017.

[50] B. Friman, F. Karsch, K. Redlich, and V. Skokov. Fluctuations as probe of the QCD phase transition and freeze-out in heavy ion collisions at LHC and RHIC. *Eur. Phys. J.*, C71:1694, 2011.

[51] J. Engels, L. Fromme, and M. Seniuch. Correlation lengths and scaling functions in the three-dimensional O(4) model. *Nucl. Phys.*, B675:533–554, 2003.

[52] M. Cheng et al. Baryon Number, Strangeness and Electric Charge Fluctuations in QCD at High Temperature. *Phys. Rev.*, D79:074505, 2009.

[53] Adam Bzdak and Volker Koch. Acceptance corrections to net baryon and net charge cumulants. *Phys. Rev.*, C86:044904, 2012.

[54] A. Bazavov et al. The QCD Equation of State to $\mathcal{O}(\mu_B^6)$ from Lattice QCD. *Phys. Rev.*, D95(5):054504, 2017.

[55] Jaroslav Adam et al. Collision energy dependence of second-order off-diagonal and diagonal cumulants of net-charge, net-proton and net-kaon multiplicity distributions in Au+Au collisions. *arXiv*, 1903.05370, 2019.

[56] Arghya Chatterjee, Sandeep Chatterjee, Tapan K. Nayak, and Nihar Ranjan Sahoo. Diagonal and off-diagonal susceptibilities of conserved quantities in relativistic heavy-ion collisions. *J. Phys.*, G43(12):125103, 2016.

[57] L. Foa. Inclusive Study of High-Energy Multiparticle Production and Two-Body Correlations. *Phys. Rept.*, 22:1–56, 1975.

[58] Sedigheh Jowzaee. Rapidity correlations in the RHIC Beam Energy Scan Data. *Nucl. Phys.*, A967:792–795, 2017.

[59] Dmitri Kharzeev, R. D. Pisarski, and Michel H. G. Tytgat. Possibility of spontaneous parity violation in hot QCD. *Phys. Rev. Lett.*, 81:512–515, 1998.

[60] Sergei A. Voloshin. Parity violation in hot QCD: How to detect it. *Phys. Rev.*, C70:057901, 2004.

[61] D. E. Kharzeev, J. Liao, S. A. Voloshin, and G. Wang. Chiral magnetic and vortical effects in high-energy nuclear collisions—A status report. *Prog. Part. Nucl. Phys.*, 88:1–28, 2016.

[62] Jie Zhao. Search for the Chiral Magnetic Effect in Relativistic Heavy-Ion Collisions. *Int. J. Mod. Phys.*, A33(13):1830010, 2018.

[63] Jie Zhao. Measurements of the chiral magnetic effect with background isolation in 200 GeV Au+Au collisions at STAR. *Nucl. Phys.*, A982:535–538, 2019.

[64] Prithwish Tribedy. Disentangling flow and signals of Chiral Magnetic Effect in U+U, Au+Au and p+Au collisions. *Nucl. Phys.*, A967:740–743, 2017.

[65] Gang Wang. STAR measurements in search of the CME and the CMW, 2018.

[66] Niseem Magdy. Collision-system Dependence of the Charge Separation Relative to the Event Plane: Implications for Chiral Magnetic Effect Search in STAR, 2019.

[67] Jaroslav Adam et al. Collision Energy Dependence of p_{t} Correlations in Au+Au Collisions at RHIC. *Phys. Rev.*, C99(4):044918, 2019.

[68] Jaroslav Adam et al. The Proton-Ω correlation function in Au+Au collisions at $\sqrt{s_{NN}}$=200 GeV. *Phys. Lett.*, B790:490–497, 2019.

[69] L. Adamczyk et al. Constraining the initial conditions and temperature dependent viscosity with three-particle correlations in Au+Au collisions. *Phys. Lett.*, B790:81–88, 2019.

[70] L. Adamczyk et al. Measurements of jet quenching with semi-inclusive hadron+jet distributions in Au+Au collisions at $\sqrt{s_{NN}} = 200$ GeV. *Phys. Rev.*, C96(2):024905, 2017.

[71] L. Adamczyk et al. Dijet imbalance measurements in $Au + Au$ and pp collisions at $\sqrt{s_{NN}} = 200$ GeV at STAR. *Phys. Rev. Lett.*, 119(6):062301, 2017.

[72] L. Adamczyk et al. Measurement of D^0 Azimuthal Anisotropy at Midrapidity in Au+Au Collisions at $\sqrt{s_{NN}}$=200 GeV. *Phys. Rev. Lett.*, 118(21):212301, 2017.

[73] T. Sjostrand and M. van Zijl. A Multiple Interaction Model for the Event Structure in Hadron Collisions. *Phys. Rev.*, D36:2019, 1987.

[74] D. T. Kettler, D. J. Prindle, and T. A. Trainor. Transverse-rapidity $\mathbf{y_t}$ dependence of the nonjet azimuth quadrupole from 62 and 200 GeV Au-Au collisions. *Phys. Rev.*, C91(6):064910, 2015.

[75] G. Agakishiev et al. Anomalous centrality evolution of two-particle angular correlations from Au-Au collisions at $\sqrt{s_{\mathrm{NN}}} = 62$ and 200 GeV. *Phys. Rev.*, C86:064902, 2012.

[76] H. Agakishiev et al. Measurements of Dihadron Correlations Relative to the Event Plane in Au+Au Collisions at $\sqrt{s_{NN}} = 200$ GeV. *arXiv*, 1010.0690, 2010.

[77] J. Schukraft, A. Timmins, and S. A. Voloshin. Ultra-relativistic nuclear collisions: event shape engineering. *Phys. Lett.*, B719:394–398, 2013.

[78] A. J. Larkoski, S. Marzani, G. Soyez, and J. Thaler. Soft Drop. *JHEP*, 05:146, 2014.

[79] G. D'Agostini. Improved iterative Bayesian unfolding. In *Alliance Workshop on Unfolding and Data Correction Hamburg, Germany, May 27-28, 2010*, 2010.

[80] T. Sjostrand, S. Mrenna, and P. Z. Skands. PYTHIA 6.4 Physics and Manual. *JHEP*, 05:026, 2006.

[81] T. Sjöstrand, S. Ask, J. R. Christiansen, R. Corke, N. Desai, P. Ilten, S. Mrenna, S. Prestel, C. O. Rasmussen, and P. Z. Skands. An Introduction to PYTHIA 8.2. *Comput. Phys. Commun.*, 191:159–177, 2015.

[82] M. Bahr et al. Herwig++ Physics and Manual. *Eur. Phys. J.*, C58:639–707, 2008.

[83] L. Apolinário, J. G. Milhano, M. Ploskon, and X. Zhang. Novel subjet observables for jet quenching in heavy-ion collisions. *Eur. Phys. J.*, C78(6):529, 2018.

[84] S. Chatrchyan et al. Modification of jet shapes in PbPb collisions at $\sqrt{s_{NN}} = 2.76$ TeV. *Phys. Lett.*, B730:243–263, 2014.

[85] J. Adam et al. Longitudinal double-spin asymmetries for dijet production at intermediate pseudorapidity in polarized pp collisions at $\sqrt{s} = 200$ gev. *Phys. Rev. D*, 98:032011, Aug 2018.

[86] J. Adam et al. Longitudinal double-spin asymmetries for π^0s in the forward direction for 510 gev polarized pp collisions. *Phys. Rev. D*, 98:032013, Aug 2018.

[87] J. Adam et al. Measurement of the longitudinal spin asymmetries for weak boson production in proton-proton collisions at $\sqrt{s} = 510$ gev. *Phys. Rev. D*, 99:051102, Mar 2019.

[88] J. Adam et al. Transverse spin transfer to Λ and $\overline{\Lambda}$ hyperons in polarized proton-proton collisions at $\sqrt{s} = 200$ gev. *Phys. Rev. D*, 98:091103, Nov 2018.

[89] J. Adam et al. Improved measurement of the longitudinal spin transfer to Λ and $\overline{\Lambda}$ hyperons in polarized proton-proton collisions at $\sqrt{s} = 200$ gev. *Phys. Rev. D*, 98:112009, Dec 2018.

[90] Chris Dilks. Transverse spin asymmetries in the $p^{\uparrow}p \longrightarrow p\pi^0 x$ process at STAR. In *DIS2019*, 2019. https://indico.cern.ch/event/749003/contributions/3339088/.

[91] Matt Posik. Constraining the sea quark distributions through $W^{\pm}$ cross section ratio measurements at STAR. In *DIS2019*, 2019. https://indico.cern.ch/event/749003/contributions/3344617/.

[92] Zilong Chang. *Inclusive Jet Longitudinal Double-Spin Asymmetry A_{LL} Measurements in 510 GeV Polarized pp Collisions at STAR*. PhD thesis, Texas A&M University, 2016.

[93] Suvarna Ramachandran. *Probing the low-x gluon helicity Distribution with Dijet Double Spin Asymmetries in Polarized Proton Collisions at $\sqrt{s} = 510$ GeV*. PhD thesis, University of Kentucky, 2018.

[94] D. De Florian, G. A. Lucero, R. Sassot, M. Stratmann, and W. Vogelsang. Monte Carlo sampling variant of the DSSV14 set of helicity parton densities. 1902.10548, 2019.

[95] L. Adamczyk et al. Measurement of the cross section and longitudinal double-spin asymmetry for dijet production in polarized *pp* collisions at $\sqrt{s} = 200$ GeV. *Phys. Rev. D*, 95:071103, Apr 2017.

[96] D. de Florian, M. Stratmann, and W. Vogelsang. Polarized Λ-baryon production in *pp* collisions. *Phys. Rev. Lett.*, 81:530–533, Jul 1998.

[97] M. Radici and A. Bacchetta. First extraction of transversity from a global analysis of electron-proton and proton-proton data. *Phys. Rev. Lett.*, 120:192001, May 2018.

[98] L. Adamczyk et al. Observation of Transverse Spin-Dependent Azimuthal Correlations of Charged Pion Pairs in $p^{\uparrow} + p$ at $\sqrt{s} = 200$ GeV. *Phys. Rev. Lett.*, 115:242501, 2015.

[99] L. Adamczyk et al. Transverse spin-dependent azimuthal correlations of charged pion pairs measured in p$^{\uparrow}$+p collisions at $\sqrt{s} = 500$ GeV. *Phys. Lett.*, B780:332–339, 2018.

[100] J. K. Adkins and J. L. Drachenberg. Azimuthal single-spin asymmetries of charged pions in jets in $\sqrt{s} = 200$ gev $p^{\uparrow}p$ collisions at star. *Int. J. Mod. Phys. Conf. Ser.*, 40:166040, 2016.

[101] Leszek Adamczyk et al. Azimuthal transverse single-spin asymmetries of inclusive jets and charged pions within jets from polarized-proton collisions at $\sqrt{s} = 500$ GeV. *Phys. Rev. D*, 97(3):032004, 2018.

[102] Zhong-Bo Kang, Alexei Prokudin, Felix Ringer, and Feng Yuan. Collins azimuthal asymmetries of hadron production inside jets. *Phys. Lett.*, B774:635–642, 2017.

[103] Umberto D'Alesio, Francesco Murgia, and Cristian Pisano. Testing the universality of the Collins function in pion-jet production at RHIC. *Phys. Lett.*, B773:300–306, 2017.

[104] M. A. Stephanov. On the sign of kurtosis near the QCD critical point. *Phys. Rev. Lett.*, 107:052301, 2011.

[105] K. J. Sun, L.-W. Chen, C. M. Ko, J. Pu, and Z. Xu. Light nuclei production as a probe of the QCD phase diagram. *Phys. Lett.*, B781:499–504, 2018.

[106] L. Adamczyk et al. Energy Dependence of Moments of Net-proton Multiplicity Distributions at RHIC. *Phys. Rev. Lett.*, 112:032302, 2014.

[107] L. Adamczyk et al. Beam energy dependence of moments of the net-charge multiplicity distributions in Au+Au collisions at RHIC. *Phys. Rev. Lett.*, 113:092301, 2014.

[108] L. Adamczyk et al. Collision Energy Dependence of Moments of Net-Kaon Multiplicity Distributions at RHIC. *Phys. Lett.*, B785:551–560, 2018.

[109] Xiaofeng Luo. Energy Dependence of Moments of Net-Proton and Net-Charge Multiplicity Distributions at STAR. *PoS*, CPOD2014:019, 2015.

[110] Xiaofeng Luo. Exploring the QCD Phase Structure with Beam Energy Scan in Heavy-ion Collisions. *Nucl. Phys.*, A956:75–82, 2016.

[111] A. Bzdak, V. Koch, D. Oliinychenko, and J. Steinheimer. Large proton cumulants from the superposition of ordinary multiplicity distributions. *Phys. Rev.*, C98(5):054901, 2018.

[112] L. Adamczyk et al. Beam Energy Dependence of Jet-Quenching Effects in Au+Au Collisions at $\sqrt{s_{\rm NN}}$ = 7.7, 11.5, 14.5, 19.6, 27, 39, and 62.4 GeV. *Phys. Rev. Lett.*, 121(3):032301, 2018.

[113] J. Adams et al. Cross-sections and transverse single spin asymmetries in forward neutral pion production from proton collisions at s**(1/2) = 200- GeV. *Phys. Rev. Lett.*, 92:171801, 2004.

[114] C. Bourrely and J. Soffer. Do we understand the single spin asymmetry for pi0 inclusive production in pp collisions? *Eur. Phys. J.*, C36:371–374, 2004.

[115] J.-W. Qiu and G. F. Sterman. Single transverse spin asymmetries in hadronic pion production. *Phys. Rev.*, D59:014004, 1999.

[116] F. Yuan. Azimuthal asymmetric distribution of hadrons inside a jet at hadron collider. *Phys. Rev. Lett.*, 100:032003, 2008.

[117] U. D'Alesio, F. Murgia, and C. Pisano. Azimuthal asymmetries for hadron distributions inside a jet in hadronic collisions. *Phys. Rev.*, D83:034021, 2011.

[118] A. Bacchetta and M. Radici. Dihadron interference fragmentation functions in proton-proton collisions. *Phys. Rev.*, D70:094032, 2004.

[119] D. Sivers. The Adventure and the Prize. *Nuovo Cim.*, C035N2:171–186, 2012.

[120] R. L. Jaffe and X.-D. Ji. Chiral odd parton distributions and polarized Drell-Yan. *Phys. Rev. Lett.*, 67:552–555, 1991.

[121] J. C. Collins. Fragmentation of transversely polarized quarks probed in transverse momentum distributions. *Nucl. Phys.*, B396:161–182, 1993.

[122] J. C. Collins, S. F. Heppelmann, and G. A. Ladinsky. Measuring transversity densities in singly polarized hadron hadron and lepton - hadron collisions. *Nucl. Phys.*, B420:565–582, 1994.

[123] A. Airapetian et al. Observation of the Naive-T-odd Sivers Effect in Deep-Inelastic Scattering. *Phys. Rev. Lett.*, 103:152002, 2009.

[124] C. Adolph et al. Transverse spin effects in hadron-pair production from semi-inclusive deep inelastic scattering. *Phys. Lett.*, B713:10–16, 2012.

[125] R. Seidl et al. Measurement of Azimuthal Asymmetries in Inclusive Production of Hadron Pairs in e+e- Annihilation at s**(1/2) = 10.58-GeV. *Phys. Rev.*, D78:032011, 2008. [Erratum: Phys. Rev.D86,039905(2012)].

[126] A. Vossen et al. Observation of transverse polarization asymmetries of charged pion pairs in e^+e^- annihilation near $\sqrt{s} = 10.58$ GeV. *Phys. Rev. Lett.*, 107:072004, 2011.

[127] M. Anselmino, M. Boglione, U. D'Alesio, S. Melis, F. Murgia, and A. Prokudin. Simultaneous extraction of transversity and Collins functions from new SIDIS and e+e- data. *Phys. Rev.*, D87:094019, 2013.

[128] J. Soffer. Positivity constraints for spin dependent parton distributions. *Phys. Rev. Lett.*, 74:1292–1294, 1995.

[129] M. Anselmino, M. Boglione, U. D'Alesio, E. Leader, S. Melis, and F. Murgia. The general partonic structure for hadronic spin asymmetries. *Phys. Rev.*, D73:014020, 2006.

[130] K. Dusling, W. Li, and B. Schenke. Novel collective phenomena in high-energy proton–proton and proton–nucleus collisions. *Int. J. Mod. Phys.*, E25(01):1630002, 2016.

[131] L. He, T. Edmonds, Z.-W. Lin, F. Liu, D. Molnar, and F. Wang. Anisotropic parton escape is the dominant source of azimuthal anisotropy in transport models. *Phys. Lett.*, B753:506–510, 2016.

[132] A. Kurkela, U. A. Wiedemann, and B. Wu. Kinetic transport is needed to reliably extract shear viscosity from pA and AA data. In , volume arXiv:1805.04081, 2018.

[133] P. Romatschke. Azimuthal Anisotropies at High Momentum from Purely Non-Hydrodynamic Transport. *Eur. Phys. J.*, C78(8):636, 2018.

[134] J. L. Nagle and W. A. Zajc. Small System Collectivity in Relativistic Hadronic and Nuclear Collisions. *Ann. Rev. Nucl. Part. Sci.*, 68:211–235, 2018.

[135] B. Schenke, S. Schlichting, and R. Venugopalan. Azimuthal anisotropies in p+Pb collisions from classical Yang–Mills dynamics. *Phys. Lett.*, B747:76–82, 2015.

[136] J. L. Nagle et al. Exploiting Intrinsic Triangular Geometry in Relativistic He3+Au Collisions to Disentangle Medium Properties. *Phys. Rev. Lett.*, 113(11):112301, 2014.

[137] C. Aidala et al. Creation of quark–gluon plasma droplets with three distinct geometries. *Nature Phys.*, 15(3):214–220, 2019.

[138] Shengli Huang. Long-range collectivity in small collision systems with two- and four-particle correlations at STAR. *Nucl. Phys. A*, 982:475–478, 2019.

[139] M. Mace, V. V. Skokov, P. Tribedy, and R. Venugopalan. Initial state description of azimuthally collimated long range correlations in ultrarelativistic light-heavy ion collisions. arXiv:1901.10506, 2019.

[140] Albert M Sirunyan et al. Observation of prompt J/ψ meson elliptic flow in high-multiplicity pPb collisions at $\sqrt{s_{\mathrm{NN}}} = 8.16$ TeV. *Phys. Lett.*, B791:172–194, 2019.

[141] S. Acharya et al. Search for collectivity with azimuthal J/ψ-hadron correlations in high multiplicity p-Pb collisions at $\sqrt{s_{\mathrm{NN}}} = 5.02$ and 8.16 TeV. *Phys. Lett.*, B780:7–20, 2018.

[142] A. M. Sirunyan et al. Elliptic flow of charm and strange hadrons in high-multiplicity pPb collisions at $\sqrt{s_{\mathrm{NN}}} = 8.16$ TeV. *Phys. Rev. Lett.*, 121(8):082301, 2018.

[143] Xiaojian Du and Ralf Rapp. In-Medium Charmonium Production in Proton-Nucleus Collisions. *JHEP*, 03:015, 2019.

[144] Cheng Zhang, Cyrille Marquet, Guang-You Qin, Shu-Yi Wei, and Bo-Wen Xiao. On the elliptic flow of heavy quarkonia in pA collisions. *Phys. Rev. Lett.*, 122(17):172302, 2019.

[145] Workshop on collectivity of small systems in high-energy collisions, 14-16 march 2019. https://indico.cern.ch/event/771998/, Accessed May 2019.

[146] Z. Citron et al. Future physics opportunities for high-density QCD at the LHC with heavy-ion and proton beams. arXiv:1812.06772, 2018.

[147] STAR. STAR Public Note SN0644 - Technical Design Report for the iTPC Upgrade. https://drupal.star.bnl.gov/STAR/starnotes/public/sn0644.

[148] STAR. STAR Public Note SN0666 - An Event Plane Detector for STAR. https://drupal.star.bnl.gov/STAR/starnotes/public/sn0666.

[149] STAR Collaboration and CBM eTOF Group. Physics Program for the STAR/CBM eTOF Upgrade. arXiv:1609.05102, 2016.

[150] K Aamodt et al. Elliptic flow of charged particles in Pb-Pb collisions at 2.76 TeV. *Phys. Rev. Lett.*, 105:252302, 2010.

[151] S. S. Adler et al. Saturation of azimuthal anisotropy in Au + Au collisions at s(NN)**(1/2) 62-GeV to 200-GeV. *Phys. Rev. Lett.*, 94:232302, 2005.

[152] J. Adam et al. Beam energy dependence of rapidity-even dipolar flow in Au+Au collisions. *Phys. Lett.*, B784:26–32, 2018.

[153] M. Aaboud et al. Measurement of the azimuthal anisotropy of charged particles produced in $\sqrt{s_{\mathrm{NN}}} = 5.02$ TeV Pb+Pb collisions with the ATLAS detector. *Eur. Phys. J.*, C78(12):997, 2018.

[154] A. Adare et al. Measurements of Higher-Order Flow Harmonics in Au+Au Collisions at $\sqrt{s_{NN}} = 200$ GeV. *Phys. Rev. Lett.*, 107:252301, 2011.

[155] G. Aad et al. Measurement of long-range pseudorapidity correlations and azimuthal harmonics in $\sqrt{s_{NN}} = 5.02$ TeV proton-lead collisions with the ATLAS detector. *Phys. Rev. C*, 90(4):044906, 2014.

[156] B. I. Abelev et al. Partonic flow and phi-meson production in Au + Au collisions at s(NN)**(1/2) = 200-GeV. *Phys. Rev. Lett.*, 99:112301, 2007.

[157] CMS Collaboration. Evidence for collectivity in pp collisions at the LHC. *Phys. Lett. B*, 765:193–220, 2017.

[158] CMS Collaboration. Evidence for Collective Multiparticle Correlations in p-Pb Collisions. *Phys. Rev. Lett.*, 115:012301, 2015.

[159] Morad Aaboud et al. Measurement of long-range multiparticle azimuthal correlations with the subevent cumulant method in pp and $p + Pb$ collisions with the ATLAS detector at the CERN Large Hadron Collider. *Phys. Rev.*, C97(2):024904, 2018.

[160] M. Aaboud et al. Correlated long-range mixed-harmonic fluctuations measured in pp, p+Pb and low-multiplicity Pb+Pb collisions with the ATLAS detector. *Phys. Lett.*, B789:444–471, 2019.

[161] S. Acharya et al. Investigations of anisotropic flow using multi-particle azimuthal correlations in pp, p-Pb, Xe-Xe, and Pb-Pb collisions at the LHC. arXiv:1903.01790, 2019.

[162] C. Aidala et al. Measurements of Multiparticle Correlations in d + Au Collisions at 200, 62.4, 39, and 19.6 GeV and p + Au Collisions at 200 GeV and Implications for Collective Behavior. *Phys. Rev. Lett.*, 120(6):062302, 2018.

[163] STAR. PUB-5347 - STAR Conceptual Design Report.

[164] B. et al Alver. Charged-particle multiplicity and pseudorapidity distributions measured with the phobos detector in au+au, cu+cu, d+au and pp collisions at ultrarelativistic energies. *Phys. Rev. C*, 83:024913, Feb 2011.

[165] I. Deppner and N. Herrmann. The CBM Time-of-Flight system. In *14th Workshop on Resistive Plate Chambers and Related Detectors (RCP2018) Puerto Vallarta, Jalisco State, Mexico, February 19-23, 2018*, 2018.

[166] D. Hu et al. MRPC3b mass production for CBM-TOF and eTOF at STAR. In *14th Workshop on Resistive Plate Chambers and Related Detectors (RCP2018) Puerto Vallarta, Jalisco State, Mexico, February 19-23, 2018*, 2018.

[167] V. Smakhtin, G. Mikenberg, A. Klier, Y. Rozen, E. Duchovni, E. Kajamovitz, and A. Hershenhorn. Thin Gap Chamber upgrade for SLHC: Position resolution in a test beam. *Nucl. Instrum. Meth.*, A598:196–200, 2009.

[168] A. Abusleme et al. Performance of a Full-Size Small-Strip Thin Gap Chamber Prototype for the ATLAS New Small Wheel Muon Upgrade. *Nucl. Instrum. Meth.*, A817:85–92, 2016.

[169] 2018 review indico page. https://indico.bnl.gov/event/5269/, Accessed May 2019.